# Durham E-Theses

## Large-scale Structure and Galaxy Formation in non-standard Cosmologies

SHI, DIFU

**How to cite:**

SHI, DIFU (2017) *Large-scale Structure and Galaxy Formation in non-standard Cosmologies*, Durham theses, Durham University. Available at Durham E-Theses Online: http://etheses.dur.ac.uk/12217/

**Use policy**

# Large-scale Structure and Galaxy Formation in non-standard Cosmologies

by Difu Shi

A Thesis presented for the degree of
Doctor of Philosophy

Institute for Computational Cosmology
Department of Physics

Durham
University

March 2017

# Large-scale Structure and Galaxy Formation in non-standard Cosmologies

## Difu Shi

## Abstract

We study the large-scale structure of alternative cosmologies, which intrinsically avoid the theoretical problems of the cosmological constant in the standard $\Lambda$ cold dark matter ($\Lambda$CDM) cosmology. We focus on early dark energy (EDE) models and $f(R)$ gravity, which are the typical examples of dark energy and modified gravity models respectively. We constrain the EDE model using measurements of cosmic microwave background and baryon acoustic oscillations, then use large-volume N-body simulations to study the structure formation and growth. EDE and $\Lambda$CDM can be distinguished through the shape of matter power spectrum on large scales, as well as the halo mass function at high redshift. We run high-resolution N-body simulations of $f(R)$ gravity in order to study in detail the properties of haloes and their environment. We find that halos less massive than $10^{13} M_\odot/h$ have a more compact inner structure in $f(R)$ gravity than in $\Lambda$CDM. These low-mass haloes grow faster and contain substantially more subhaloes in $f(R)$ gravity. We also measure the correlation between different halo environment definitions used in observations and the fifth force potential in $f(R)$ gravity. Although the different ways to define environment do not agree with one another perfectly, they can provide useful guidance about how well a dark matter halo is screened. We also find that the screening of subhaloes in dark matter haloes is primarily determined by the environment, with the subhalo mass playing a minor role. Finally, we investigate and improve the H$\alpha$ luminosity function predicted by semi-analytical galaxy formation model, GALFORM. The result is important for accessing the performance of Euclid redshift survey, which is one of the missions cosmological probe of accelerating cosmic expansion.

# Declaration

The work in this thesis is based on research carried out between October 2012 and March 2017. The author is was a postgraduate research student under the supervision of Prof. Carlton Baugh and Dr. Baojiu Li at the Institute for Computational Cosmology in the Department of Physics at Durham University.

This work has not been submitted for any other degree at the University of Durham or any other University.

Chapter 2, 3 & 4 have been published in the form of refereed papers,

- Shi, Difu; Li, Baojiu; Han, Jiaxin; Gao, Liang; Hellwing, Wojciech A. **Exploring the liminality: properties of haloes and subhaloes in borderline $f(R)$ gravity**, *Monthly Notices of the Royal Astronomical Society* (2015) **452**: 3179-3191.

- Shi, Difu; Baugh, Carlton M. **Can we distinguish early dark energy from a cosmological constant?** *Monthly Notices of the Royal Astronomical Society* (2016) **459**: 3540-3550.

- Shi Difu, Li Baojiu, Han Jiaxin, **Environmental screening of dark matter haloes in $f(R)$ gravity**, *Monthly Notices of the Royal Astronomical Society* (2017) **469**: 705-715.

Parts of Chapter 5 were published as part of the following paper:

- Pozzetti, L.; Hirata, C.M.; Geach, J.E.; Cimatti, A.; Baugh, C.; Cucciati, O.; Merson A.; Norberg P.; Shi D. **Modelling the number density of H$\alpha$ emitters for future spectroscopic near-IR space missions**, *Astronomy & Astrophysics* (2016) **590**: A3.

All figures shown in this thesis were made by the author, with the exception of Fig. 5.1. These were taken from Pozzetti et al. (2016), on which the author has also collaborated.

# Acknowledgements

I would first like to thank my two supervisors, Carlton Baugh and Baojiu Li, for the excellent guidance they provided over the past four and a half years. Their endless patience and enthusiasm keep me always stay positive during the whole of my PhD time. I have learned a great deal from the enjoyable discussions and interacting with you. You are my teachers as well as my friends.

Thanks to all my collaborators: Jiaxin Han, Elise Jennings, Wojciech Hellwing, Liang Gao, and colleagues: Jun Hou, Celine Boehm, Peder Norberg, Silvia Pascoli, for their assistance and contribution to the work in this thesis. It has been a pleasure working with you all. I should offer my great appreciation to the wonderful ICC IT team, Lydia Heck and Alan Lotts particularly. Without your day and night hard working and patience to solve the computational issues, I would never run my simulations on COSMA. It is a privilege to be part of the astronomy department at Durham.

My very special thanks to all of my friends in Durham, especially to Dan Li, Lei Fan, Xiaolin Mou, Yuexian Hong, Mengwei Sun, Yi Gu, Xuan Chen, Jing Zhang, Ang Li and Manjun Liu. You make the on-earth part of my PhD life so colourful. I will never forget the laughter and tears, the weekend nights and the drunks, with all of you. Wish our friendships built in this cold rainy country would keep on fire forever.

Finally, I am deeply thankful to my dearest Mum and Dad for the support not only during the PhD, but during all my life. Whenever I have been depressed, your gentle concerns can always encourage me to carry on.

# Contents

# List of Figures

# List of Tables

# Chapter 1

# Introduction

In 1929, Edwin Hubble discovered the expansion of the Universe by measuring the relation between the distances to galaxies and their redshifts (Hubble, 1929). Galaxies are actually flying away from one another rather than fixed in a static Universe. This surprising discovery marks the birth of modern cosmology. Since then, the 'hot big bang' gradually became the most popular hypothesis of cosmology. At the end of twentieth century, observations of distant supernovae type Ia (SNIa) revealed a even more unexpected phenomenon that the expansion of the Universe is accelerating (Riess et al., 1998; Perlmutter et al., 1999). This is not just the first suggestion of the mysterious energy source which competes against standard gravity which is called "dark energy", but also the beginning of a new era in cosmology. The $\Lambda$ cold dark matter ($\Lambda$CDM) model is the standard theoretical paradigm, and treats dark energy as a cosmological constant, $\Lambda$, which is assumed to be the vacuum energy. The Universe is thought to have evolved from a compact and dense early state after the big bang to a vast and sparse current state with galaxies. Dark energy dominates the energy budget of the Universe and drives the accelerating expansion in recent cosmological history. Despite the great success of the $\Lambda$CDM model, the fine tuning problem and cosmic coincidence problem still leave big question marks over the cosmological constant. Understanding the nature of dark energy is one of the biggest challenges in modern cosmology. Cosmic structure formation is driven by a competition between gravitational attraction and the expansion of the Universe. Hence, the large scale structure of the Universe can be useful tool to probe funda-

mental physics including the nature of dark energy and the theory of gravity. By measuring the growth rate of overdensities and the clustering statistics of galaxies, we can distinguish between different cosmological models. Precision modelling of the evolution of cosmic structure and galaxy formation in both standard and non-standard cosmologies provides accurate theoretical predictions for the interpretation of future galaxy surveys and other cosmological observations.

This chapter reviews the standard cosmological model and discusses viable ways to improve it. We also give a brief introduction about modelling and simulating the cosmic structure growth and galaxy formation.

## 1.1   The standard ΛCDM model of cosmology

The Λ cold dark matter (ΛCDM) model assumes the cosmological principle, which is the notion that the Universe is statistically homogeneous and isotropic on large scales. The model can be divided into four main ingredients: (i) the standard model of particle physics; (ii) cold dark matter (CDM); (iii) dark energy, Λ; and (iv) general relativity (GR) as the theory of gravity. There are plenty of cosmological observations that support the ΛCDM model. These include temperature anisotropies in the cosmic microwave background (CMB) (Hinshaw et al., 2013; Planck Collaboration et al., 2016a), baryonic acoustic oscillations (BAO) (Cole et al., 2005; Eisenstein et al., 2005), galaxy cluster abundances (Allen et al., 2011; Planck Collaboration et al., 2016b) etc. The energy density of the Universe today is composed of approximately 4% baryons, 26% dark matter and 70% dark energy. In this model, dark energy is assumed to be a negative pressure component in the Universe which acts against the gravitational attraction and drives the accelerated expansion, behaving as a fluid with a constant equation of state, $w = P/\rho = -1$. It is the most familiar and the simplest candidate for dark energy (see the review, e.g. Carroll 2001), and simply requires adding a cosmological constant, Λ, into general relativity.

The Einstein-Hilbert action with a cosmological constant is given by

$$S[g] = \int \left[ \frac{1}{16\pi G}(R - 2\Lambda) + \mathcal{L}_m \right] \sqrt{-g}\, \mathrm{d}^4 x, \qquad (1.1.1)$$

where $R$ is the Ricci tensor, $g$ is the space-time metric, $G$ is Newton's constant and $\mathcal{L}_m$ is the matter field. The stationary point of the variation of $S[g]$ with respect to the metric then yields the Einstein equation,

$$R_{\mu\nu} - \frac{1}{2}g_{\mu\nu}R = \frac{8\pi}{c^4}GT_{\mu\nu} - \Lambda g_{\mu\nu}, \tag{1.1.2}$$

where $T_{\mu\nu}$ is the energy-momentum tensor and $c$ is speed of light. On assuming the cosmological principle and a perfect fluid, the Einstein equation has an exact solution for the Friedmann-Lematre-Robertson-Walker (usually FRW in short) metric, which is

$$\mathrm{d}s^2 = \mathrm{d}t^2 + a^2(t)[(1 - kr^2)^{-1}\mathrm{d}r^2 + r^2\mathrm{d}\theta^2 + \sin^2\theta\ \mathrm{d}\phi^2], \tag{1.1.3}$$

where $r$, $\theta$ and $\phi$ are spherical polar coordinates and $k$ describes the spatial curvature and usually takes on the values 0, 1, -1 to represent a flat, closed or open universe respectively. The $a(t)$ is the comic scale factor which is normalized such that at the present time, $a = 1$.

On inserting the FRW metric into the Einstein equations, after some tedious algebra, we obtain the Friedmann equations:

$$\left(\frac{\dot{a}}{a}\right)^2 = \frac{8\pi G}{3}\rho - \frac{kc^2}{a^2} + \frac{\Lambda}{3}, \tag{1.1.4}$$

$$\frac{\ddot{a}}{a} = -\frac{4\pi G}{3}\left(\rho + \frac{3p}{c^2}\right) + \frac{\Lambda}{3}, \tag{1.1.5}$$

where the dot denotes the time derivative. The first equation is from the 00 component of the Einstein equation and the second is from the ii component. The Hubble parameter is defined as $H = \dot{a}/a$. For a given value of $H$, a special value of the density would be required to make a flat universe, $k = 0$. This is known as the critical density,

$$\rho_c = \frac{3H^2}{8\pi G}. \tag{1.1.6}$$

It is conventional to express density in units of the critical density. If we define $H_0$ as the Hubble "constant" at the present time and $\rho_{c,0}$ as the critical density at the

present time, then Eq. 1.1.4 becomes:

$$H^2 = H_0^2 \left( \frac{\rho_m}{\rho_{c,0}} + \frac{\rho_r}{\rho_{c,0}} + \frac{\rho_\Lambda}{\rho_{c,0}} + \frac{\rho_k/a^2}{\rho_{c,0}} \right), \qquad (1.1.7)$$

where $\rho_m$ and $\rho_r$ are the matter density and radiation density respectively, $\rho_\Lambda = \Lambda/8\pi G$ is the dark energy density and $\rho_k = 3kc^2/8\pi G$ is the "curvature density". It is convenient to introduce the dimensionless density parameter,

$$\Omega_i = \rho_i/\rho_c. \qquad (1.1.8)$$

$\Omega$ can be used to rewrite the Friedmann equation. As we also know that the matter density evolves as $1/a^3$, radiation as $1/a^4$ and $\Lambda$ retains a constant density, we can write

$$H^2 = H_0^2 \left( \frac{\Omega_{m,0}}{a^3} + \frac{\Omega_{r,0}}{a^4} + \Omega_{\Lambda,0} + \frac{\Omega_{k,0}}{a^2} \right). \qquad (1.1.9)$$

The additional cosmological constant term is interpreted as a new fluid component to the Universe which is referred to as dark energy. This negative pressure component is generally assumed to be the vacuum energy arising from the zero point fluctuations of quantum fields.

## 1.2 Beyond ΛCDM

In ΛCDM, the negative pressure component is generally assumed to be the vacuum energy arising from the zero point fluctuations of quantum fields. Despite the success of ΛCDM at fitting much of the available observational data, this model fails to address two important issues: the fine-tuning problem and the cosmic coincidence problem. The fine-tuning problem arises from the huge discrepancy between the vacuum energy level predicted by particle physics, and the value measured from cosmological observations, $\rho \sim 10^{-47}\text{GeV}^4$. However, in the standard model of particle physics, a plausible value for the vacuum energy level is approximately 120 orders of magnitude higher than the measured energy density. The coincidence problem refers to the fact that the dark energy density has a comparable energy

density to matter, $\rho_{de} \sim \rho_m$, and has just emerged as the dominant component of the Universe. It implies that we live in a intermediate phase when the gravity and anti-gravity effects are of comparable size, i.e. the expansion of the Universe has 'just' begun to accelerate. Given the enormous age of the universe, this is a relatively short and special period of time. If the acceleration began earlier in the universe, structures such as galaxies would never have had time to form. To solve the fine-tuning and cosmic coincidence problems, many alternative models have been introduced. These models can be generally divided into two categories: (alternative) dark energy and modified gravity.

### 1.2.1   Dark energy

To find an alternative explanation of the accelerating expansion, perhaps the most straight forward option is to assume that dark energy is a dynamical field rather than a constant. An abundance of models has been proposed in the literature (e.g. the review by Copeland et al., 2006). Although these models can have very different potentials, what they share is the presence of a degree of freedom which in result drives the background cosmological evolution and late-time accelerating expansion. This kind of model, which introduces a fifth contribution to the cosmic energy density, is defined as "quintessence". For example, the simplest option is to replace the $\Lambda$ in Eq. 1.1.1 by a canonical scalar field with a potential,

$$S[g] = \int \left[ \frac{1}{16\pi G} R - \frac{1}{2} (\partial \phi)^2 - V(\phi) + \mathcal{L}_m \right] \sqrt{-g} \, \mathrm{d}^4 x. \qquad (1.2.10)$$

The scalar field behaves as a perfect fluid with an equation of state,

$$w = \frac{\frac{1}{2} \dot{\phi}^2 - V(\phi)}{\frac{1}{2} \dot{\phi}^2 + V(\phi)}, \qquad (1.2.11)$$

where dots denote derivatives with respect to time. The quintessence equation of state is generally time-dependent as the scalar field evolves with time. If the field is potential-dominated at the present time, the quintessence model will agree with the observational constraint that $w$ is very close to $-1$ in the present universe.

There is an interesting property that a wide class of quintessence models show, the so-called "tracking" behavior, where the energy density in the field traces the matter energy density until recent times. This behavior provides a possible explanation of the cosmic coincidence problem. The Ratra-Peebles potential, $V(\phi) = M^{4+n}/\phi^n$ with $n > 0$, is one typical example (Ratra & Peebles, 1988).

## 1.2.2 Modified gravity

General relativity has passed all the precision tests performed in the Solar system (Will, 2014), including the famous observation that the Sun bends the light from background stars and the anomalous perihelion of Mercury, as well as the Shapiro time-delay effect measured by the Cassini spacecraft and Lunar laser ranging experiments which measure the rate of change of the strength of gravitation. Recently, the LIGO consortium has also confirmed the existence of gravitational waves, a GR predicted phenomena, by measuring a merger event of two black holes (Abbott et al., 2016a). However, the length scales probed by all these measurements are much smaller than cosmological scales. Whether GR still works on large scales is unclear. Weaker gravity on large scales may explain the accelerating expansion of the Universe. This idea is the starting point of modifying gravity.

General relativity describes gravity as the relationship between matter and curvature in the Universe. Unlike the dark energy model which adds a new matter-like component to the Einstein equation, an alternative way to explain the accelerating expansion is to change the matter and curvature relation, or in other words, to modify general relativity itself. There are lots of modified gravity models on the market. These models generally introduce new degrees of freedom in the gravitational sector, which can be motivated by low energy limits of string theory, or by higher dimensional gravity theories, etc. (Koyama, 2016).

The simplest and probably best-studied modifications to Einstein's gravity are scalar-tensor theories (Boisseau et al., 2000). For a canonical scalar field, $\phi$, the general form of these theories can be derived by minimising the action:

$$S = \int \left[ \frac{1}{16\pi G} R - \frac{1}{2}(\partial\phi)^2 - V(\phi) + \mathcal{L}_m(A^2(\phi)g_{\mu\nu}, \psi) \right] \sqrt{-g} \; \mathrm{d}^4 x. \qquad (1.2.12)$$

Here, the arbitrary function $A^2(\phi)$ can be absorbed into the metric by a conformal transformation of the form, $A^2(\phi)g_{\mu\nu} \to \tilde{g}_{\mu\nu}$, which is usually referred to as the Jordan frame (Dicke, 1962). $\psi$ represents the matter fields which couple to the Jordan-frame metric $\tilde{g}_{\mu\nu}$. Thus, test particles in the Newtonian regime would feel a force,

$$-\vec{\nabla}(\Phi + \ln A(\phi)), \tag{1.2.13}$$

which is sourced by both the Einstein-frame potential, $\Phi$, and the scalar field, $\phi$. In principle, it is possible to pass Solar System tests of gravity, while still having interesting phenomenology for the scalar field by carefully designing suitable forms of $V(\phi)$ and $A(\phi)$. For example, the Brans-Dicke theory defines $V(\phi) = 0$ and $A^2(\phi) = \exp[\phi/\sqrt{(2/3 + \omega)/8\pi G}]$, where $\omega$ is a constant (Brans & Dicke, 1961). Interestingly, under the Solar System constraints, this scalar field couples very weakly to matter, which makes Brans-Dicke theory practically equivalent to a dark energy model.

We will focus on the so-called $f(R)$ gravity in this thesis (Carroll et al., 2004). The Einstein-Hilbert action of $f(R)$ gravity is modified as

$$S[g] = \int \left[ \frac{1}{16\pi G}(R - f(R)) + \mathcal{L}_m \right] \sqrt{-g} \, \mathrm{d}^4 x, \tag{1.2.14}$$

where $f(R)$ is a general function only of the Ricci scalar. Although Eq. 1.2.14 does not look like a scalar-tensor theory at all, in fact, $f(R)$ gravity is classically equivalent to a scalar-tensor theory on performing a field redefinition and conformal transformation (see e.g. Joyce et al. 2015 for details). Again, mathematically, $f(R)$ can be any arbitrary function. But, in order to drive the accelerating expansion, $f(R)$ is required to become significant in the low-curvature regime. A simple example of these theories is $f(R) \propto 1/R$ (Carroll et al., 2004). Besides this, there are some other limits on the form of $f(R)$, for instance, the effective gravitational constant, $G_{\mathrm{eff}} = G/(1 + f(R))$, should remain positive for all $R$ to avoid the graviton becoming a ghost (Amendola et al., 2007).

No matter what particular form of modified gravity model is adopted, the extra amount of force in addition to Newtonian gravity force is introduced because of the new degrees of freedom in the gravitational sector (as shown in Eq. 1.2.13).

In order to evade the tight Solar System constraints on gravity, which are in the high-curvature regime and on small scales, the theory must employ some 'screening mechanism'. This dynamically suppresses the additional degrees of freedom in regions like the Solar System. There are plenty of screening mechanisms in the literature. Based on the nature of the screening criterion, we can classify them into three cases: i) screening based on the local field value $\phi$, like the chameleon (Khoury & Weltman, 2004), symmetron (Hinterbichler & Khoury, 2010; Pietroni, 2005; Olive & Pospelov, 2008) and dilaton (Damour & Polyakov, 1994; Brax et al., 2010); ii) screening based on the first derivative $\partial\phi$, like K-mouflage (Babichev et al., 2009); and iii) screening based second derivative $\partial^2\phi$, like Vainshtein mechanism (Vainshtein, 1972). We note that there is another way to build the screen mechanism, by confining the extra interaction to act only on dark energy and dark matter. This is a valid way to reconcile the Solar System tests. More details of this type of screening mechanism can be found in Amendola (2000).

It is only a rough classification to divide non-standard cosmological models into dark energy and modified gravity. There is no strict boundary between them. If the "quintessence" in a dark energy model can couple to matter, the gravity is phenomenological being modified. On the other hand, if the extra amount of force in a modified gravity model is highly screened or couples very weakly to matter, this model is more likely to be a dark energy model. Actually, dark energy is formally equivalent to modified gravity, because modifying or adding a term on either left-hand side or right-hand side of Einstein equation (Eq. 1.1.2) is mathematically equivalent. In this thesis, we study two typical examples of dark energy and modified gravity models: 1) the early dark energy model, in which dark matter and baryon obey the same gravity law as GR, but the cosmic background evolution is modified; 2) the $f(R)$ gravity, in which gravity at low density region is enhanced, but the background evolution is almost the same as ΛCDM. We will have detailed introduction of these models in subsequent chapters.

## 1.3    The linear growth of density fluctuations

The formation of inhomogeneous structure in the Universe is thought to be seeded by tiny quantum fluctuations in the early Universe that ultimately appear as anisotropies in the CMB. The overdensity of matter can be defined as

$$\delta(\mathbf{x}) = \frac{\rho(\mathbf{x})}{\bar{\rho}} - 1, \tag{1.3.15}$$

where the bar denotes the mean density of the Universe, i.e. the unperturbed (homogeneous) matter density. Assuming an ideal fluid, in the Newtonian limit, the linear approximation of cosmological perturbation growth is described by

$$\text{Euler:} \quad \frac{\partial \mathbf{v}}{\partial t} + \mathbf{v} \cdot \vec{\nabla} \mathbf{v} + 2\frac{\dot{a}}{a}\mathbf{v} = -\frac{\vec{\nabla}P}{\rho} - \frac{\vec{\nabla}\Phi}{a^2}, \tag{1.3.16}$$

$$\text{Continuity:} \quad \frac{\partial \delta}{\partial t} + \vec{\nabla} \cdot [(1+\delta)\mathbf{v}] = 0, \tag{1.3.17}$$

$$\text{Poisson:} \quad \vec{\nabla}^2\Phi = 4\pi G\bar{\rho}a^2\delta, \tag{1.3.18}$$

where $\Phi$ is the gravitational potential and differentiation with respect to $\mathbf{x}$ is denoted by $\vec{\nabla}$ (see the derivation of these equations in e.g. Dodelson & Efstathiou 2004). We can combine the three equations above to describe the growth of matter perturbations in an expanding universe. For example, if we assume that the pressure gradients are negligible, $\vec{\nabla}P/\rho \ll \vec{\nabla}\Phi$, then taking the divergence of the Euler equation, and eliminating $\mathbf{v}$ by taking the time derivative of the continuity equation and substituting $\vec{\nabla}^2\Phi$ using Poisson's equation, gives the growth equation for density perturbations,

$$\frac{\partial^2\delta}{\partial t^2} + 2H\frac{\partial \delta}{\partial t} = 4\pi G\bar{\rho}\delta. \tag{1.3.19}$$

Here, the expansion rate introduces an effective friction term into Eq. 1.9 corresponding to the Hubble drag term,

This second-order differential equation (Eq. 1.3.19) has the general solution:

$$\delta(\mathbf{x}, t) = A(\mathbf{x})D_+(t) + B(\mathbf{x})D_-(t), \tag{1.3.20}$$

where $D_+$ and $D_-$ are the growing and decaying modes respectively. In a flat, matter-dominated universe, $\Omega_m = 1$, $D_+(t) \propto t^{2/3}$ and $D_2(t) \propto t^{-1}$. After some time, the decaying mode vanishes and the perturbation grows as

$$\delta \propto D(t) \propto a(t). \tag{1.3.21}$$

We ignore the subscript $+$ for $D_+$ hereafter. Because the matter density perturbations are small (i.e. the density contrast $\delta(\mathbf{x}, t) \ll 1$) at early times, the structure growth can be written as

$$\delta(\mathbf{x}, t) = \frac{D(t)}{D(t_i)} \delta(\mathbf{x}, t_i), \tag{1.3.22}$$

where $D$ is defined as linear growth factor.

In observations and simulations, it is convenient to use the matter power spectrum to describe the density fluctuation in the Universe. The power spectrum is the Fourier transform of the correlation function. The matter overdensity in Fourier space is given as,

$$\delta(\mathbf{k}) = (2\pi)^{-2/3} \int \mathrm{d}^3 x \delta(\mathbf{x}) e^{i\mathbf{k}\cdot\mathbf{x}}. \tag{1.3.23}$$

Assuming that the overdensities are isotropic, the two-point statistic can be written as

$$\langle \delta(\mathbf{k})\delta(\mathbf{k}') \rangle = \langle |\delta(k)|^2 \rangle \delta^3(\mathbf{k} - \mathbf{k}') \equiv P(k)\delta^3(\mathbf{k} - \mathbf{k}'). \tag{1.3.24}$$

Here, $P(k)$ is the power spectrum. As Eq. 1.3.22, in linear regime, the power spectrum is a function only of time,

$$P(k, t) = \frac{D(t)^2}{D(t_0)^2} P(k, t_0), \tag{1.3.25}$$

where $D(t_0)$ is the present-day linear growth factor, which is usually normalised to unity.

## 1.4 Simulations of the formation of cosmic structures

The linear growth of overdensities is theoretically well understood. However, once the evolution of fluctuations becomes non-linear (where $\delta \not\ll 1$) it becomes significantly more complicated and difficult to describe by analytical equations. The non-linear behaviour of structure formation appears in high density regions where galaxies form. So precise and accurate modelling of the non-linear growth is crucial to study the predictions of particular models, and can only be done by numerical simulation.

The basic procedure to simulate the formation of cosmic structures is as follows: i) divide a representative portion of the Universe into "particles"; ii) compute the gravitational forces on these particles from all the other particles; iii) evolve the system forward in discrete time steps and then go back to procedure ii and repeat. This portion of the Universe is usually a cube with periodic boundary conditions. The "particles" are not physical particles, but actually represent some large quantity of physical particles. The chosen of particle mass is a compromise between numerical accuracy and computational cost. The simulation is set up by applying a perturbation to an initially uniform distribution of particles, so that the resulting density distribution has the appropriate power spectrum at the starting redshift.

The N-body code is essentially a gravity solver. The gravitational potential is given by the Poisson equation (Eq. 1.3.18). The equations are usually solved in a comoving frame. The expansion rate of the Universe is calculated using the Friedmann equation (Eq. 1.1.4). For cosmological simulations, because the General Relativity corrections are generally negligible, the Newtonian equations are actually solved. The naïve way to construct the gravitational potential for each particle is by directly summing up the contributions made by each of the remaining particles. This method is called the Particle-Particle (PP) method, and obviously not appropriate, as $\mathcal{O}((\mathcal{N}-1)!)$ operations are required to compute all forces on $N$ particles. A more efficient algorithm needs to be applied.

One way to simplify the calculation is to approximate the gravitational force of

a distant group of particles by the force due to a single pseudo particle located at the centre of mass of the group, with mass equal to the total mass of the group of particles. In particular, the particles are organised into a hierarchical tree structure (Barnes & Hut, 1986). The process starts with a cubical cell containing the entire simulation box. Then this cell is divided into eight equal-sized sub-cells. The process is executed recursively in each sub-cell at every stage until the smallest cells only have one particle in them. The resulting tree structure is then used to calculate an approximation to the gravitational force felt by each particle. For a single particle, if a cell satisfies the criterion, $r > l/\theta$, the cell is regarded as a pseudo particle to calculate the gravitational force. Otherwise, the criterion is tested for each sub-cell. Here, $r$ is the distance between the particle and the cell, $l$ is the size of the cell, and $\theta$ is the tree opening angle. Again, this process starts with the largest cell and continues recursively until all the particles have contributed. This criterion means that long-range forces are approximated by grouping particles into larger-scale cells. The short-range force is more accurately computed, because, for the nearby particles, the tree is walked to greater depth and the cell contains fewer particles. Actually, if a cell only has one particle, the calculation is back to the PP method. $\mathcal{O}(\mathcal{N} \log \mathcal{N})$ operations are required to compute the forces on $N$ particles.

Another method is the particle-mesh (PM) technique (e.g. Hockney & Eastwood, 1988), which works by assigning particle mass to Cartesian grids. The PM algorithm has three steps. Firstly, the mass density field is computed on each grid cell. Then, the Poisson equation is solved on the grid for the gravity field. Finally, the gravity field on the grid is interpolated back to the particles. In the first step, the mass density of the grid is computed from discrete particle positions and masses. The simplest mass assignment method is the nearest grid point (NGP), where the mass is allocated to the grid cell in which the particle resides. Obviously, this method loses the small-scale information and could produce large truncation errors. These can be reduced by using a higher order interpolation scheme such as the cloud-in-cell (CIC) or triangular-shaped-cloud (TSC). In the CIC scheme, the particle is treated as a uniform-density cubical cloud and assigned to the 8 nearest grid cells depending on the overlap, while the TSC scheme uses the nearest 27 grid cells.

The gravitational potential on a grid is obtained by solving the Poisson equation in $\mathbf{k}$ space, as follows: i) Fourier transform the density field on the grid; ii) apply Green's function to convolve the density field; iii) solve the gravitational potential; and iv) transform it back to real space. Using the Fast Fourier Transform (FFT) algorithm (Cooley & Tukey, 1965), this requires $\mathcal{O}(\mathcal{N}_g \log \mathcal{N}_g)$ operations to solve Poisson equation in $N_g$ grid cells.

Tree codes can resolve the force on particles accurately down to the softening length, while PM codes are limited in resolution to the grid cell size. However, the PM code is faster per time step and requires less memory than the tree algorithm. The GADGET-2 (Springel, 2005) code uses a TreePM algorithm, which is a hybrid of the tree and PM methods. The potential at large-scales is evaluated using the PM method, whereas the potential on smaller-scales is calculated from the hierarchical tree. GADGET-2 exploits the advantages of the two methods. The simulations in Chapter 2 use variants of the GADGET-2 code. Instead of using a tree algorithm to improve the small-scale resolution in PM method, RAMSES code (Teyssier, 2002) makes use of the adaptive mesh refinement (AMR) method. This adaptively refines the grid in regions requiring higher resolution. For example, in a high density region, the grid is divided into sub-grids and then Poisson equation is sloved locally. The more deeply the grid is spilt into sub-grids, the higher force resolution is obtained. The simulations in Chapter 3 & 4 use a modified gravity version of RAMSES code (Li et al., 2012).

## 1.5 Galaxy formation modelling

The N-body codes introduced in the previous section model the growth of structure in collisionless matter. Baryons behave quite differently compared to the dark matter. In order to model galaxy formation and evolution, theorists have developed a wide range of different tools (Somerville & Davé, 2015). We now briefly introduce the most commonly used tools.

One class of galaxy model is to assign galaxies to dark matter halos according to some rules based on a mapping between the properties of the dark matter halos

and the observable properties of galaxies. Halo occupation distribution models (e.g. Berlind & Weinberg, 2002) and subhalo abundance matching (SHAM) models (e.g. Tasitsiomi et al., 2004) are two widely used empirical techniques. These models do not actually model any physical processes. Because no heavy computation is required, they are extremely useful to gain insight into the connection between simulated dark matter halos and observed galaxies.

Numerical hydrodynamic simulation is the most explicit way to model galaxy formation (Schaye et al., 2015; Vogelsberger et al., 2014). It requires solving the equations of hydrodynamics and thermodynamics in addition to Poisson equation, because baryonic gas particles carry more information like an intrinsic internal energy besides their position, velocity and mass. Similarly, as with a dark-matter-only simulation, these equations are concurrently solved for particles and/or grid cells which represent dark matter, gas, and stars. Obviously, hydrodynamic simulations can provide more physical and accurate predictions within the limitations of numerical resolution. However, the extremely heavy computational exigencies seriously restrict the resolution of simulations. Furthermore, the small-scales physics, like star formation, black hole growth and feedback, is not fully understood. We have to apply uncertain and even arbitrary subgrid recipes for these important processes of galaxy formation (Schaye et al., 2015). Worse still, due to the computational limitations, it is nearly impossible to extensively test different subgrid recipes or widely explore the multidimensional parameter space of the these recipes. Both the GADGET-2 and RAMSES codes have hydrodynamical solver. But we do not use the hydrodynamical part of these two codes in the simulations of this thesis.

Another technique that is widely used for modeling galaxy formation is semi-analytic modelling (SAMs) which treats the various physical processes associated with galaxy formation using approximate, and analytic techniques (see e.g. Baugh, 2006; Benson, 2010, for reviews). These models work on the halo merger trees obtained from N-body simulations or generated by a Monte-Carlo method. Gas is assumed to be initially spatially distributed in the same way as the dark matter. A typical SAM tracks how much gas accretes into halos, how much hot gas cools down and turns into stars, how feedback processes remove cold gas from the galaxy or

heat the halo gas, and how mergers transform disk galaxies into spheroidal galaxies, etc. Because SAMs do not explicitly solve the hydrodynamical equations, the computational cost of SAMs is much smaller than that of hydrodynamic simulations. This make it possible to apply SAMs to very large-volume simulations. Although the numerical resolution is a disadvantage, the modeling of small-scales physics is somewhat more reliable than subgrid recipes in hydrodynamical simulations, because the rapid exploration of parameter space and model space is practicable in SAMs. We use the Durham semi-analytical galaxy formation model, GALFORM, in the simulations of chapter 5. A more detailed description of GALFORM is provided in that chapter.

## 1.6  Outline of thesis

In this thesis, we study the structure growth in the alternative cosmologies using N-body simulations. We also explore how many galaxies the Euclid redshift survey will detect using semi-analytical galaxy formation model. The rest of this thesis is organized as follows.

In Chapter 2, we investigate the power spectrum, halo mass function and redshift distortion effects in early dark energy cosmologies using a set of large-volume N-body simulations. Chapters 3 and 4 are devoted to the predictions in a 'borderline' $f(R)$ gravity model using high-resolution N-body simulations. In Chapter 3, we study the properties of halo and subhalo in $f(R)$ gravity. Then, in Chapter 4, we measure the correlation between different halo environment definitions used by observers and the fifth force potential in $f(R)$ gravity. In Chapter 5, we use Durham semi-analytical galaxy formation model, GALFORM, to estimate the number of galaxies the Euclid survey will see. Particularly, we test and improve the prediction of H$\alpha$ luminosity functions in GALFORM. Finally, we summarize our results and outline future research directions in Chapter 6.

# Chapter 2

# Can we distinguish early dark energy from a cosmological constant?

## 2.1 Introduction

One of the key objectives of future galaxy surveys is to determine the nature of the dark energy behind the accelerating cosmic expansion. In particular, does the dark energy take the form of a cosmological constant, which is hard to explain from a theoretical perspective, or is it a dynamical field, with a time dependent equation of state? What is the best way to distinguish between these scenarios for the dark energy? Here we demonstrate that this is a remarkably challenging problem, once the competing models have been set up to reproduce what we already know about the Universe.

The standard $\Lambda$ Cold Dark Matter ($\Lambda$CDM) cosmological model, in which dark energy is time independent, provides a good description of current data (e.g. Efstathiou et al., 2002; Sánchez et al., 2009, 2012; Planck Collaboration et al., 2014, 2016a). However, the cosmological constant lacks theoretical motivation and throws up issues such as the fine-tuning and the coincidence problems. Many alternatives have been proposed to alleviate these problems (e.g. the review by Copeland, Sami, & Tsujikawa, 2006). A number of these are based on time-evolving scalar

fields, which are usually referred to as quintessence models (Ratra & Peebles, 1988; Wetterich, 1988; Caldwell, Dave, & Steinhardt, 1998; Ferreira & Joyce, 1998).

In $\Lambda$CDM, the impact of the cosmological constant on the cosmic expansion can be ignored once the energy density of the dark energy falls below $\sim 1\%$ of the critical density, which occurs above $z \sim 5$. In contrast, a class of quintessence models called early dark energy (EDE) display a small but non-negligible amount of dark energy at early times which can change the expansion rate appreciably, even as early as the epoch of matter-radiation equality. These models can be divided into two classes: the so called "tracker fields" (Steinhardt, Wang, & Zlatev, 1999) and "scaling solutions" (Halliwell, 1987; Wetterich, 1995).

Previous simulations of EDE cosmologies, such as those by Grossi & Springel (2009), Francis, Lewis, & Linder (2009) and Fontanot et al. (2012), focused on the impact on structure formation of the different expansion history with EDE compared with $\Lambda$CDM, whilst keeping the same linear theory power spectrum and background cosmological parameters as used in $\Lambda$CDM. However, to produce a fully self-consistent model two further steps are necessary in addition to changing the expansion history (Jennings et al., 2010). First, the best fitting cosmological parameters will be different in EDE cosmologies than they are in $\Lambda$CDM. Second, the input power spectrum used to set up the initial conditions for the N-body simulation should be different in EDE from that used in $\Lambda$CDM. The change in the expansion history alters the width of the break in the power spectrum around the scale of the horizon at matter - radiation equality (Jennings et al., 2010). This change in the power spectrum is compounded by the changes in the cosmological parameters between the best fitting EDE and $\Lambda$CDM models. If we are to compare models that satisfy the current observational constraints to look for measurable differences which can be probed by new observations, we need to take all three of these effects into account.

EDE models can be described in terms of a scalar field potential, with the dynamical properties obtained by minimizing the action that includes the scalar field potential. We take a more practical view and consider parametrizations of EDE models which allow us to explore the parameter space more efficiently. Corasaniti &

Copeland (2003) presented four and six parameter models for the time dependence of the equation of state parameter of the dark energy, $w$, which give very accurate reproductions of the results of the full Lagrangian minimisation. However, with current data it is not feasible to constrain such a large number of additional parameters in addition to the standard cosmological parameters. Instead we investigate two parameter formulations of the dark energy.

We demonstrate that current observations of temperature fluctuations and the polarization of the cosmic microwave background (CMB) radiation and the apparent size of baryon acoustic oscillations (BAO) in the galaxy distribution already put tight constraints on EDE models. In fact, the best fitting models are consistent with *no* early dark energy, a conclusion that has been reached by other studies (Planck Collaboration et al., 2014, 2016c). Nevertheless, models with appreciable amounts of dark energy remain formally consistent with the current data. We consider two cases which have one and two percent of the critical density in dark energy back to the epoch of matter radiation equality.

In the standard lore, EDE models display a more rapid expansion at high redshift than ΛCDM and so, if they are normalised to have the same fluctuations on $8h^{-1}\mathrm{Mpc}$ today (ie the same value of $\sigma_8$), structures form earlier in these models. We find that this is not a generic feature of EDE. The EDE models we consider have growth rates that are very similar to that in ΛCDM, even lagging behind ΛCDM at intermediate redshifts. This results in these cosmologies actually displaying *fewer* massive haloes than ΛCDM at high redshifts.

This chapter is organized as follows. In Section 2.2 we discuss the parametrization of EDE models (§ 2.1), the constraints derived on cosmological parameters using CMB and BAO data (§ 2.2), compare the rate at which fluctuations grow in EDE and ΛCDM (§ 2.3) and describe the N-body simulations carried out (§ 2.4). The simulation results, namely the matter power spectrum, distribution function of counts-in-cells and halo mass function are presented in Section 2.3. Finally, in Section 2.4, we give a summary of our results.

## 2.2 Theoretical background

In this section we explain the behaviour of EDE cosmologies and how this is parametrized (§ 2.2.1), and then present constraints on the cosmological parameters in EDE and ΛCDM (§ 2.2.2). The rate at which fluctuations grow in the different cosmologies is calculated in § 2.2.3. The numerical simulations used are described in § 2.2.4.

### 2.2.1 Early Dark Energy cosmologies

The dark energy equation of state, $w(z) = P/\rho$, where $P$ is pressure and $\rho$ is density, determines how dark energy influences the expansion of the universe. In the standard ΛCDM model, the equation of state of the dark energy is a constant, $w_\Lambda = -1$, and the dark energy density parameter $\Omega_{\text{de}}(z)$ falls rapidly to zero with increasing redshift (see Fig. 2.1). The cosmological constant can be completely ignored beyond $z \sim 5$, once it accounts for less than 1% of the critical density. However, if the dark energy equation of state is such that $w > -1$, $\Omega_{\text{de}}$ will decrease more slowly and the consequences of dark energy will be felt earlier.

Quintessence originates from theoretical models which treat the dark energy as a slowly evolving scalar field. The scalar field can be described by potentials with different properties. Viable models share common features such as reproducing the observed magnitude of the present-day energy density and producing an accelerating expansion at late times. Due to the time-dependent scalar field, the dark energy equation of state evolves. The ratio of the energy density of dark energy to the critical density in quintessence models, $\Omega_{\text{de}}$, will be different from that in the ΛCDM model. This affects the growth of structure (see Fig. 2.1 for a comparison between $\Omega_{\text{de}}$ in ΛCDM and in the EDE models simulated here; the choice of EDE model is discussed later in § 2.2.2). Observations constrain the present-day dark energy equation of state to be $w_0 < -0.8$ (Sánchez et al., 2012). So, EDE models which agree with this constraint should display a transition in $w$ from the present day value ($w \approx -1$) to the early-time value (usually close to zero). How and when this transition happens is the main difference between the various EDE models.

Ideally, the dark energy equation of state should be derived from the potential
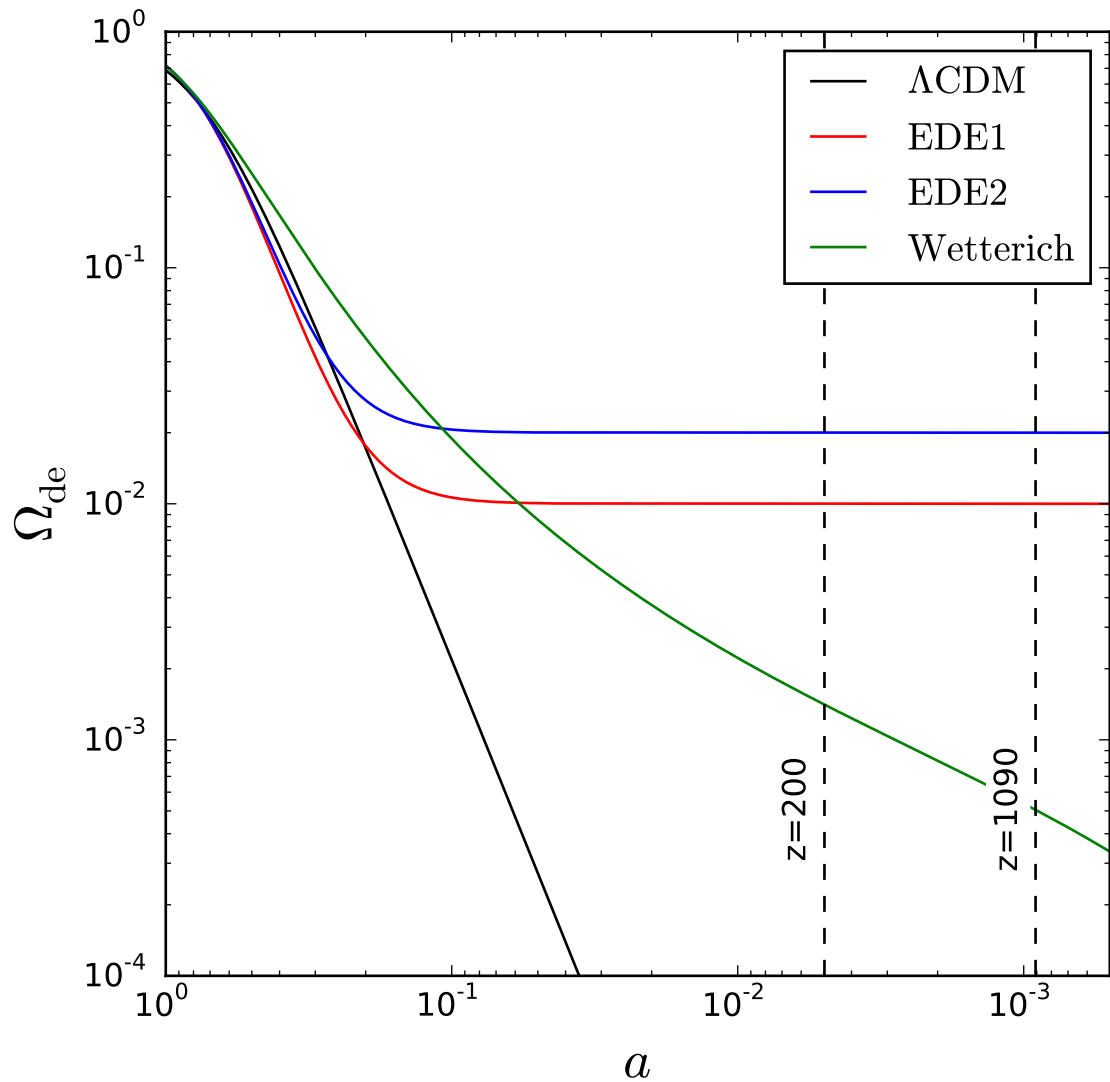
Figure 2.1: The dark energy density parameter, $\Omega_{\mathrm{de}}$, as a function of scale factor, $a$, for the two EDE models studied here, the EDE1 model (red line), EDE2 model (blue line), the Wetterich model (green line) and $\Lambda$CDM (black line). (See Table 2.1 for the model parameters.) The two black dashed lines indicate, as labelled, redshift 200 when our simulations are started and the CMB redshift, $z \sim 1090$.

energy associated with a time dependent scalar field. However, the motivation behind the form of the potential is weak which means that a wide variety of cases have been considered (Corasaniti & Copeland, 2003). One way to carry out a systematic study of the EDE parameter space is to use a parametrization for the dark energy equation of state, $w$, or the dark energy density parameter, $\Omega_{\mathrm{de}}$. This approach offers a model-independent and efficient way to investigate the properties of EDE models which display similar behaviour for $w$.

The most commonly used and simplest parametrization to describe the evolution of the equation of state is the two-parameter equation, $w = w_0 + (1 - a)w_a$, where $a$ is the expansion parameter (Chevallier & Polarski, 2001; Linder, 2003). However, Bassett, Corasaniti, & Kunz (2004) have shown that a two-parameter equation is not sufficiently accurate to describe the equation of state of the scalar field to better than 5 per cent beyond $z \sim 1$. This problem is even worse when if a two-parameter model is to be used in an N-body simulation which might start at a very high redshift (e.g. $z \approx 100$). More complex parametrizations with more parameters have been proposed which can capture the behaviour seen in a wide range of quintessence models (Corasaniti & Copeland, 2003). However, the additional parameters are hard to constrain in practice given current observations.

Instead we investigate empirical parametrizations of EDE which have three parameters. One was introduced by Wetterich (2004) and is given in terms of the equation of state parameter,

$$w(a) = -\frac{w_0}{(1 - b\ln(a))^2},$$
(2.2.1)

where

$$b = -\frac{3w_0}{\ln\left(\frac{1-\Omega_{\mathrm{de,e}}}{\Omega_{\mathrm{de,e}}}\right) + \ln\left(\frac{1-\Omega_{\mathrm{m,0}}}{\Omega_{\mathrm{m,0}}}\right)}.$$
(2.2.2)

Here $w_0$ is the dark energy equation of state today, $\Omega_{m,0}$ is the matter (i.e. baryons and cold dark matter) density parameter at $z = 0$. $\Omega_{\mathrm{de,0}}$ and $\Omega_{\mathrm{de,e}}$ are, respectively, the dark energy density parameters today and as $z \to \infty$.

The other empirical parametrization we consider was proposed by Doran & Robbers (2006) and is written in terms of the time evolution of the dark energy density

parameter

$$\Omega_{\mathrm{de}}(a) = \frac{\Omega_{\mathrm{de},0} - \Omega_{\mathrm{de,e}}(1 - a^{-3w_0})}{\Omega_{\mathrm{de},0} + \Omega_{\mathrm{m},0}a^{3w_0}} + \Omega_{\mathrm{de,e}}(1 - a^{-3w_0}). \qquad (2.2.3)$$

Both parametrizations mimic $\Lambda$CDM at low redshift and can provide non-negligible amounts of EDE at early times, depending upon the parameter values adopted. The Doran & Robbers parametrization allows rapid transitions in the dark energy equation of state. The variation of $w(a)$ in the Wetterich parametrization is more gradual as shown in Fig. 2.2. If we assume $\Omega_{\mathrm{m}} + \Omega_{\mathrm{de}} = 1$ at $z = 0$, the two parametrizations yield $\Lambda$CDM, $w(a) = w_0 = -1$, in the limit when $\Omega_{\mathrm{de,e}} = 0$.

### 2.2.2 Parameter fitting

Changing the equation of state, $w$, from a constant to being time-dependent will affect the evolution of the Universe. The cosmological distance-redshift relation also changes. Cosmological constraints derived for $\Lambda$CDM will not necessarily apply in an EDE universe. We need to re-fit the cosmological parameters for an EDE cosmology and use the best-fitting values in a simulation of such a model rather those derived for $\Lambda$CDM. Here we use observations of the CMB and BAO to find the best-fitting cosmological parameters for EDE models. Using the CMB and BAO data in this way not only allows us to determine the cosmological parameters we should use in simulations, but is also a preliminary test of the viability of EDE parametrization.

To derive the constraints on EDE parameters, we use the CMB measurement from the Planck 2013 data release (Planck Collaboration et al., 2014), which contains the Planck temperature angular power spectrum (TT) and WMAP9 polarization data (WP), in the form of likelihood software[1]. We adapted the Markov Chain Monte-Carlo code, CosmoMC, to work for EDE cosmologies (Lewis & Bridle, 2002). Some studies, such as Wang & Mukherjee (2006), use CMB distance priors which condense the full temperature fluctuation power spectrum into three quantities which depend on an assumed cosmological model to describe the peak positions and peak height ratios (Komatsu et al., 2009; Wang & Wang, 2013). Al-

---

[1]We note that the Planck 2015 results show a somewhat tighter constraint on $\Omega_{\mathrm{de,e}}$ for the Doran & Robbers (2006) model than we find using the 2013 data release (Planck Collaboration et al., 2016c).
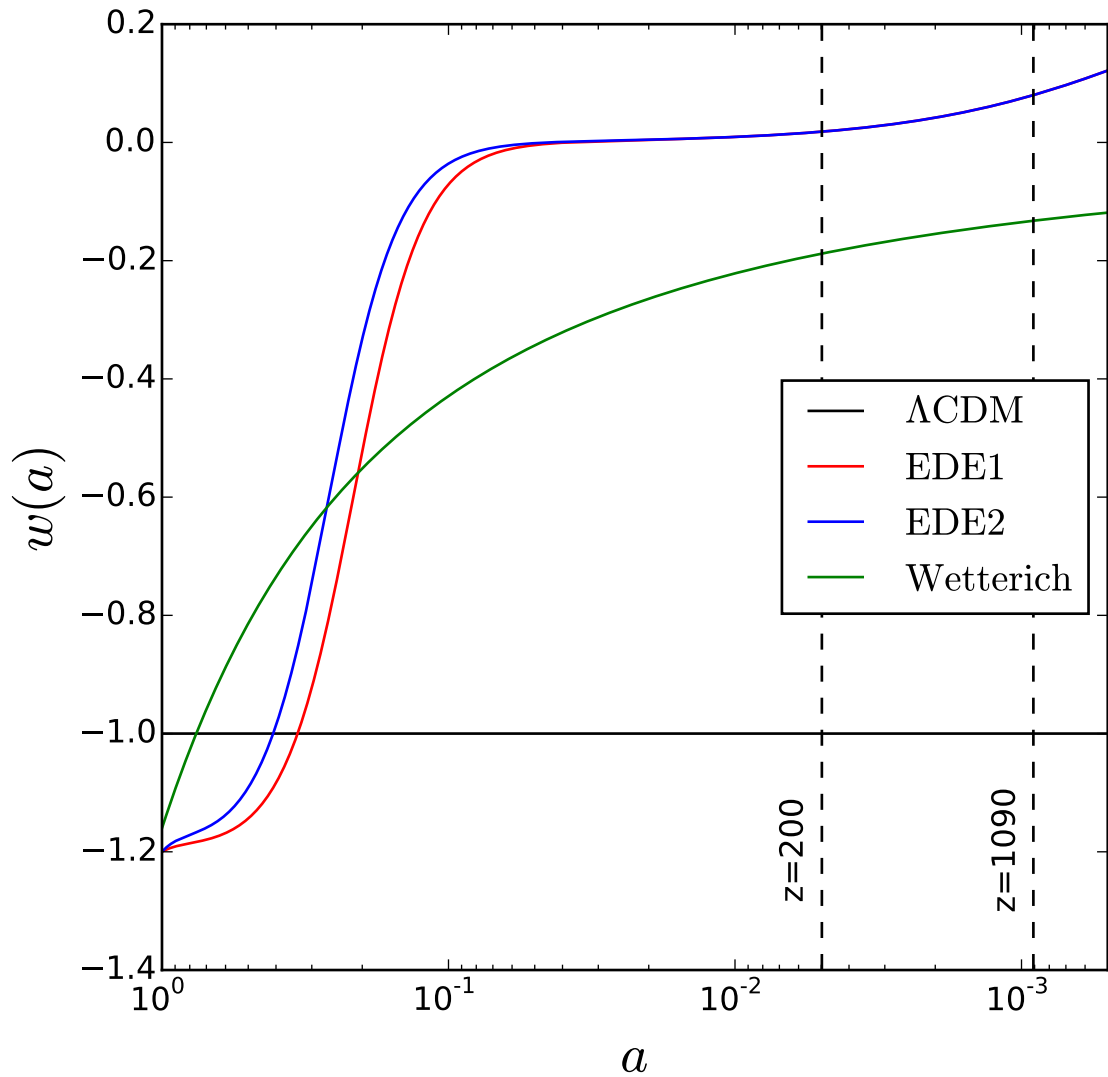
Figure 2.2: The dark energy equation of state, $w$, as a function of the scale factor, $a$, for the EDE1 model (red line), EDE2 model (blue line), a Wetterich model (green line) and $\Lambda$CDM (black line). (See Table 2.1.) The two black dashed lines indicate the redshift when the simulations are started ($z = 200$) and the CMB redshift ($z \sim 1090$).
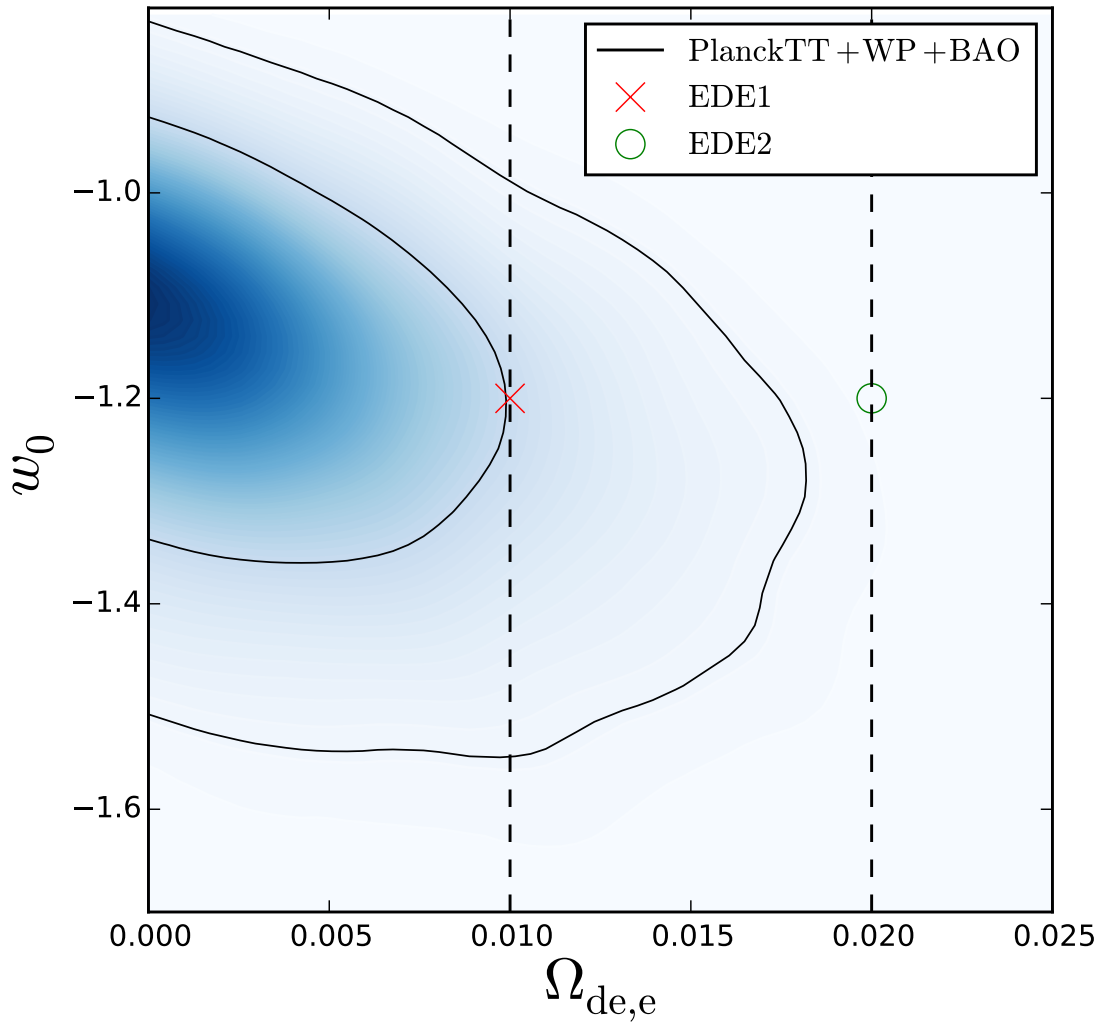
Figure 2.3: The 2D marginalized distribution in the present day equation of state parameter, $w_0$, and the critical density in dark energy at early times, $\Omega_{de}$, using the Doran & Robbers EDE parametrization for the Planck TT, WMAP polarization and BAO data combination. The constraint is compatible with $\Lambda$CDM. The solid black lines show the 68% and 95% confidence intervals. The red cross and green circle indicate, respectively, the EDE1 and EDE2 models which are used in our simulations. The black dashed lines indicate the values of $\Omega_{de}$ in these models.

though this method is faster, we do not use it here because it results in weaker constraints than using the full data set.

We also use the BAO feature in the galaxy distribution which depends on the horizon scale at matter-radiation decoupling and angular diameter distance to a given redshift. The BAO measurements used are the $z = 0.106$ result from the 6dF Galaxy Survey (6dFGS, Beutler et al., 2011), the $z = 0.35$ measurement from Sloan Digital Sky Survey Data Release 7 (SDSS DR7, Percival et al., 2010) and the $z = 0.57$ measurement from the Baryon Oscillation Spectroscopic Survey (BOSS, Sánchez et al., 2012).

Fig. 2.3 shows the 2D marginalized distribution for $w_0$ and $\Omega_{\mathrm{de,e}}$ using the Doran & Robbers parametrization of EDE. $\Lambda$CDM ($w_0 = -1$, $\Omega_{\mathrm{de,e}} = 0$) is within the 68% confidence level. The Doran & Robbers cosmologies with 1 and 2 percent EDE are respectively roughly 1 and 2 $\sigma$ away from the best-fitting value. In order to maximize the effects of EDE, here, we choose $w_0 = -1.2$ and $\Omega_{\mathrm{de,e}} = 0.01$ as the "EDE1" model, $\Omega_{\mathrm{de,e}} = 0.02$ as the "EDE2" model rather than using the best fitting values and keep the other cosmological parameters the same between the two models. The EDE1 and EDE2 models are therefore somewhat in tension with the current observational constraints but are formally consistent with the data.

Table 2.1 summarizes the constraints for the $\Lambda$CDM and EDE cosmologies, assuming a flat universe. In the EDE models, the cosmological parameters show small departures from the best fitting $\Lambda$CDM values. The best fitting result obtained using the Wetterich parametrization gives a negligible amount of EDE, $\Omega_{\mathrm{de,e}} \sim 0$, corresponding to $\Lambda$CDM if we fix $w_0 = -1$. The Wetterich parametrization does not yield any EDE when constrained using current observations. The Doran & Robbers parametrization can reproduce the step-like transition in the dark energy equation of state that results from solving the equations of motion for an EDE potential, so we focus on this parametrization from hereon.

Fig. 2.2 shows the dark energy equation of state as a function of scale factor for the EDE1 and EDE2 models, along with the $\Lambda$CDM model. The corresponding dark energy density parameter as a function of scale factor is shown in Fig. 2.1. Here, we plot the Wetterich model with $\Omega_{\mathrm{de,e}} = 10^{-5}$, which is much larger than
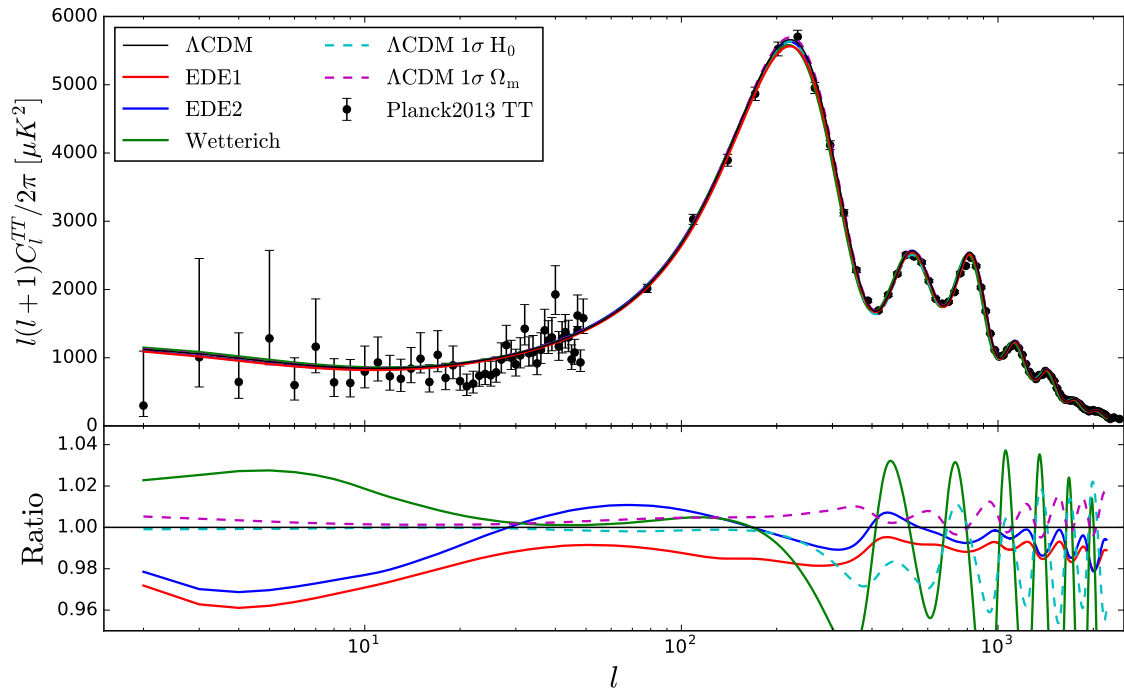
Figure 2.4: The upper panel shows the cosmic microwave background temperature fluctuation spectra of the EDE1, EDE2, ΛCDM and Wetterich models from Table 2.1 compared with the Planck 2013 data (Planck Collaboration et al., 2014) (see legend). Two variants of the ΛCDM model are also shown, which depart from the best fitting model by similar amounts to the EDE models. The lower panel shows the ratio of these models to ΛCDM.

Table 2.1: Summary of the best fitting values using CMB and BAO data for the dark energy parametrizations of Doran & Robbers (labelled EDE1 and EDE2) and Wetterich, along with ΛCDM. All models have $\sigma_8 = 0.8$.

| Parameter | ΛCDM | EDE1 | EDE2 | Wetterich |
|---|---|---|---|---|
| $H_0$ | 67.7 | 71.9 | 71.9 | 70.7 |
| $\Omega_{de}$ | 0.687 | 0.719 | 0.719 | 0.716 |
| $\Omega_b$ | 0.0488 | 0.0424 | 0.0424 | 0.044 |
| $w_0$ | -1 | -1.2 | -1.2 | -1.16 |
| $\Omega_{de,e}$ | - | 0.01 | 0.02 | $< 10^{-7}$ |

the value listed in Table 2.1, but retain the other best-fitting cosmological parameters for comparison. At late times the EDE1 and EDE2 models show very similar behaviour to ΛCDM, with a rapid transition to $w \approx 0$ at early times. The dark energy parameter remains nearly constant at early times ($z \gtrsim 9$). Even for the tiny amount of EDE considered, the Wetterich model deviates from ΛCDM from very low redshift. The BAO data probe low redshifts which is why the observational constraints do not allow Wetterich model to have non-negligible EDE.

Since the EDE1 and EDE2 models are not best-fitting models, in order evaluate the effect of the deviations before running simulations, we look at two variant ΛCDM models for comparison. One is a ΛCDM model with a value of $\Omega_{\mathrm{m}}$ which deviates by $1\sigma$ from the best-fitting value, labelled "ΛCDM $1\sigma$ $\Omega_{\mathrm{m}}$". The other one is a ΛCDM model with $H_0$ deviating by $1\sigma$ from the best-fitting value, named "ΛCDM $1\sigma$ $H_0$". We use the CAMB code (Lewis & Bridle, 2002) to generate the CMB temperature spectra for those models. Fig. 2.4 shows the comparison between all the models and the Planck CMB data. It is clear that the CMB peaks of the Wetterich model are shifted to lower multipoles compared to ΛCDM. All the other models have similar CMB spectra and fit the Planck data reasonably well. At very low multipoles, $l < 50$, the "ΛCDM $1\sigma$ $\Omega_{\mathrm{m}}$" and "ΛCDM $1\sigma$ $H_0$" models are almost the same as ΛCDM. However, the two Doran & Robbers models deviate from ΛCDM by up to 4 percent at these multipoles. Hence the differences between the EDE1 and EDE2 models and ΛCDM are not due to the fact that the EDE models are not formally the best fitting models but rather arise because of the different expansion histories. Fig. 2.4 also shows that the acoustic oscillations appear at slightly different $l$ in EDE1 and EDE2 than in ΛCDM, as shown by the oscillations in the ratio of power spectra shown in the lower panel.

### 2.2.3 Linear growth rate

The evolution of linear growth rate reflects the different growth histories of structure between the EDE and ΛCDM cosmologies. If we assume the dark matter perturbations are small, i.e., the density contrast $\ll 1$, the power spectrum, $P(k,t)$ can be
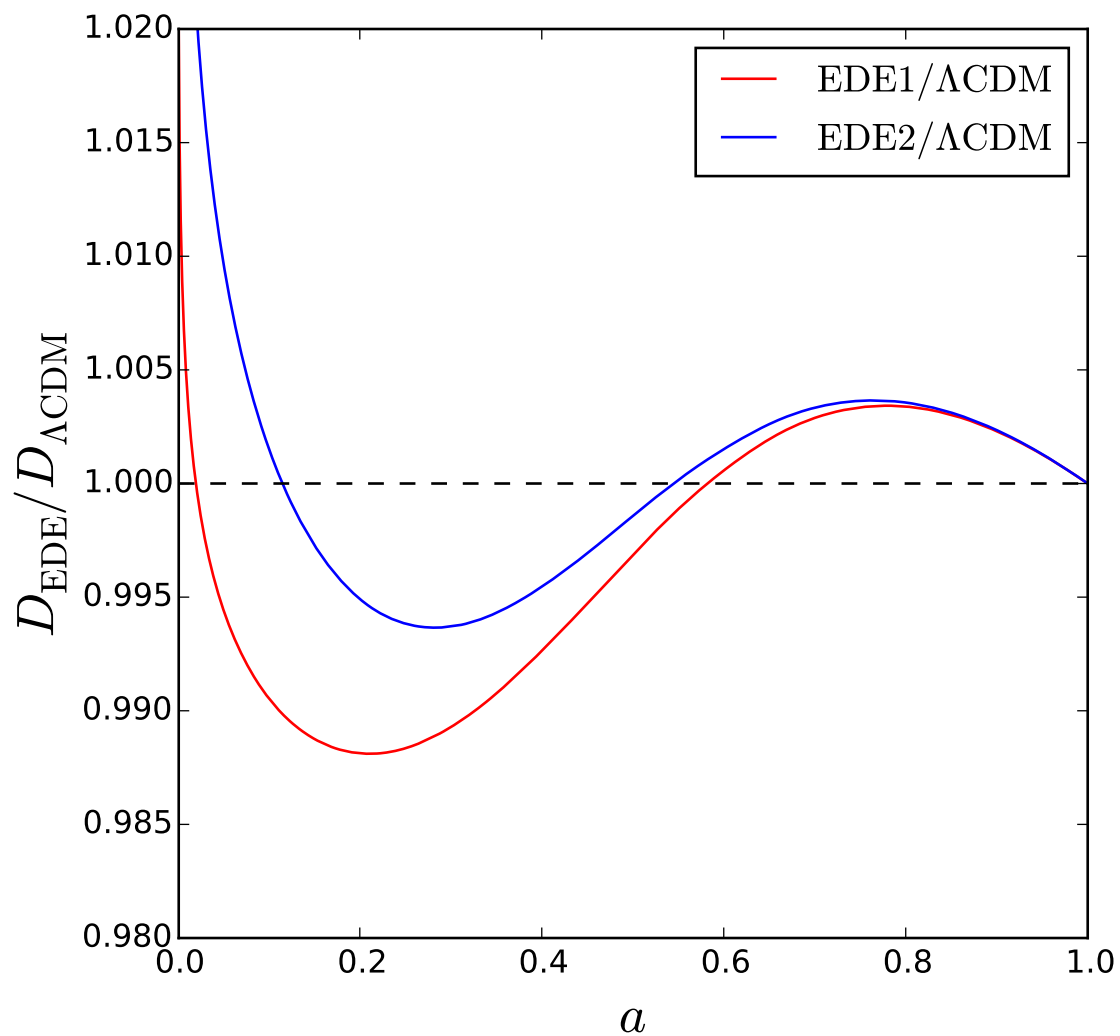
Figure 2.5: The ratio of the linear growth factor in the EDE models considered here compared to $\Lambda$CDM as labelled. The linear growth factor is normalized to unity at $z = 0$ in all models.
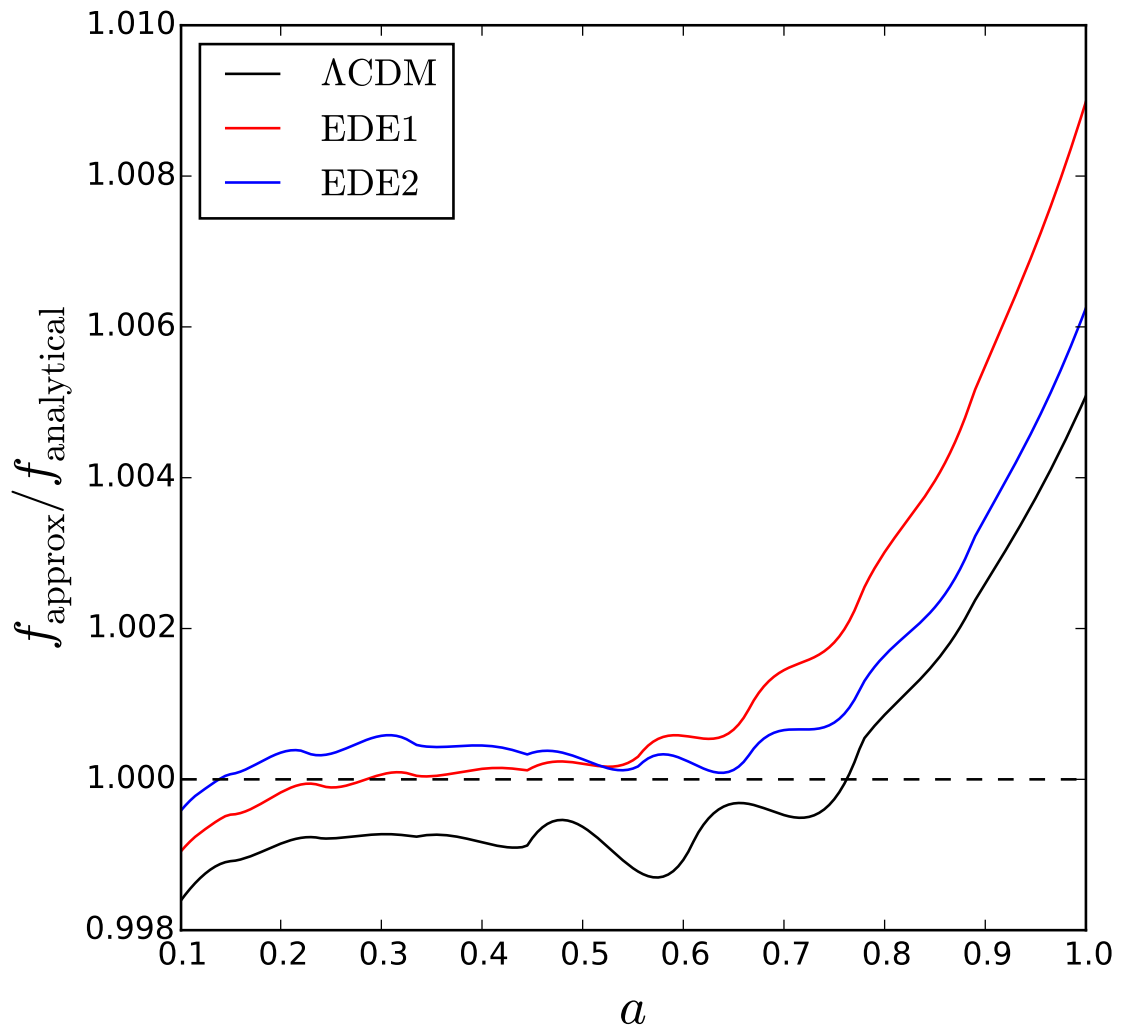
Figure 2.6: A comparison of growth rate obtained using an approximation, $f_{\mathrm{approx}}$, estimated from Eq. 2.2.7 and the analytical value, $f_{\mathrm{analytical}}$ calculated using Eq. 2.2.5 in the EDE and $\Lambda$CDM models as labelled.

written as a function of time,

$$P(k,t) = \frac{D(t)^2}{D(t_0)^2} P(k, t_0).$$ (2.2.4)

Here, $D(t_0)$ is the linear growth factor today and is obtained by solving the differential equation (Linder, 1998):

$$D'' + \frac{2}{3}\left(1 - \frac{w(a)}{1 + X(a)}\right)\frac{D'}{a} - \frac{3}{2}\frac{X(a)}{1 + X(a)}\frac{D}{a^2} = 0,$$ (2.2.5)

where

$$X(a) = \frac{\Omega_{\rm m}}{1 - \Omega_{\rm m}}e^{-3\int_a^1 d\ln a' w(a')}.$$ (2.2.6)

The linear growth rate is defined as $f = d\ln D/d\ln a$. Fig. 2.5 shows the ratio of the linear growth factor in the EDE1 and EDE2 models to that in $\Lambda$CDM. Before $z = 10$, the growth factor is enhanced by a few percent in the EDE1 and EDE2 compared with $\Lambda$CDM, before showing a reduction for $z \sim$ 2–10.

Although it is straightforward to obtain the linear growth factor by solving Eq. 2.2.5, some parametrizations of linear growth rate have become popular. Peebles (1976) proposed a widely used parametrization, $f(z) \approx \Omega_m^\gamma$, where $\gamma = 0.6$ is the growth index. Linder (2005) suggested the more accurate form

$$\gamma = 0.55 + 0.05[1 + w(z = 1)],$$ (2.2.7)

which gives $f = \Omega_m^{0.55}$ for a $\Lambda$CDM cosmology.

In order test the accuracy of the Linder parametrization for the growth factor, we plot in Fig 2.6 the approximate growth rate, $f_{\rm approx}$, given by Eq. 2.2.7 divided by the value $f_{\rm analytical}$ calculated from Eq. 2.2.5. For the EDE1 and EDE2 models and $\Lambda$CDM, the approximation reproduces the linear growth rate to better than 1% over the redshift range from $z = 0$ up to $z = 10$. Nevertheless, at late times the inaccuracy in the growth rate obtained from Eq. 2.2.7 is comparable to the magnitude of the departure from the $\Lambda$CDM growth rate, which means that the full calculation should be used.
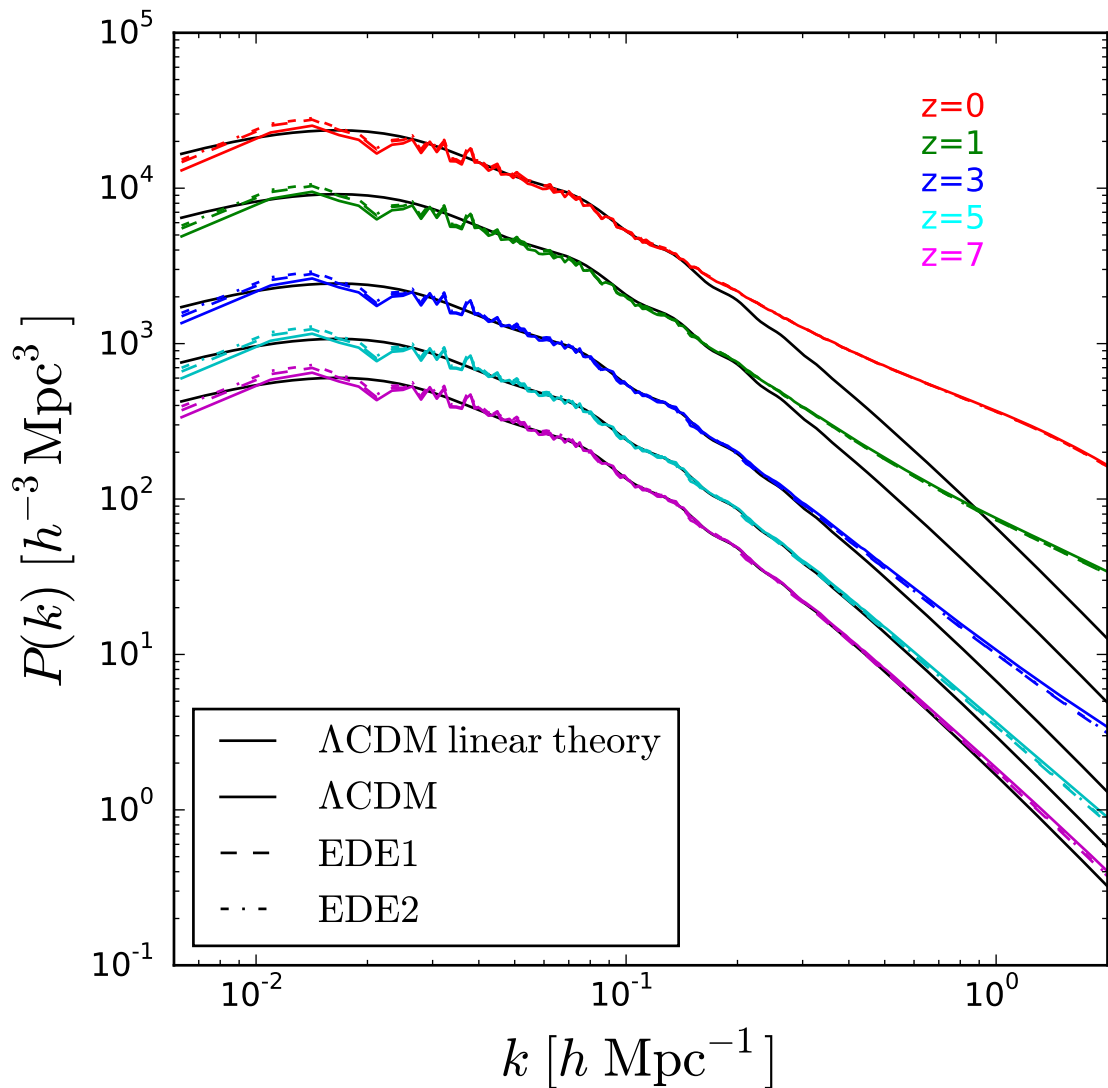
Figure 2.7: The matter power spectra measured in the EDE1, EDE2 and ΛCDM simulations. Different line styles refer to the results for different models and different colours show the measurements at different redshifts, as indicated by the key. The smooth black curves show the predictions of linear perturbation theory in ΛCDM. Differences between the EDE1 and EDE2 models and the ΛCDM results are apparent at very small and high wavenumbers.

### 2.2.4   N-body Simulations

We have carried out three large volume, moderate resolution N-body simulations for $\Lambda$CDM and the EDE1 and EDE2 cosmologies, using a memory-efficient version of the TreePM code GADGET-2(Springel, 2005), called L-GADGET2. The code was used in Jennings et al. (2010) and has been modified in order to allow a time dependent equation of state for dark energy. We assume a flat universe and use the cosmological parameters in Table 2.1. The simulations use grid initial conditions with $N = 2048^3$ dark matter particles in a computational box of a comoving length of 1500 $h^{-1}$Mpc. The particle mass is $3.413 \times 10^{10} h^{-1} M_\odot$ for $\Lambda$CDM and $3.064 \times 10^{10} h^{-1} M_\odot$ for the EDE1 and EDE2 models. The initial mean inter-particle separation is 0.732 $h^{-1}$Mpc. We adopt a comoving softening length of $\epsilon = 15$ $h^{-1}$kpc. The initial conditions were generated using the L-GENIC code (Springel et al., 2005), which has also been adapted to handle a time variable equation of state. A self-consistent linear theory power spectrum for each model is generated using CAMB (Lewis & Bridle, 2002). The normalisation extrapolated to $z = 0$ is $\sigma_8 = 0.8$ for all simulations. The starting redshift is $z = 199$. We have tested that the results presented have converged for these choices of particle number, softening length and starting redshift. In EDE model, matter obeys the same gravity and only the cosmic background evolution is modified comparing to $\Lambda$CDM. We expect the difference between EDE and $\Lambda$CDM is mainly on large scales. So we chose a relatively large simulation box in order to study large-scale structure, redshift space distortions and rare objects.

## 2.3   Results

Here we present a range of results from our N-body simulations: the matter power spectrum in real and redshift space (§ 2.3.1), the dark matter halo mass function (§ 2.3.2), and the distribution of counts-in-cells (§ 2.3.3).

### 2.3.1   Matter power spectrum

The power spectrum of fluctuations in the matter distribution is a key statistic that encodes information about the cosmological parameters and is the starting point

for determining many quantities, such as the clustering of galaxies and the weak gravitational lensing of faint galaxies. The presence of dark energy at early times in the EDE cosmologies can change the form of the matter power spectrum compared to that in $\Lambda$CDM and may allow us to distinguish between models. The use of N-body simulations allows this comparison to be extended into the nonlinear regime.

**The power spectrum in real space**

Fig. 2.7 shows the matter power spectra at redshifts $z = 0, 1, 3, 5, 7$ measured from the $\Lambda$CDM, EDE1 and EDE2 simulations, together with the linear perturbation theory power spectra for $\Lambda$CDM. At $z = 0$, the power spectra have very similar amplitudes at intermediate wavenumbers because the three models have been normalized to have the same value of $\sigma_8$ today ($\sigma_8 = 0.8$). The power spectra, however, are noticeably different at very small wavenumbers (large scales). There are also small differences apparent deep into the nonlinear regime at high wavenumbers (small scales).

The EDE models differ from $\Lambda$CDM on large scales at all plotted redshifts. This is due to the difference in the expansion histories in these models compared with that in $\Lambda$CDM. This changes the rate at which fluctuations grow, particularly around the transition from radiation to matter domination, which alters the shape of the turnover in the power spectrum (Jennings et al., 2010). To drill down further into the comparison between the power spectra in the models we now compare the simulation measurements after taking into account differences in the linear growth factor at a given redshift (as plotted in Fig. 2.5). Fig. 2.8 shows the ratio of matter power spectrum after dividing by the linear growth factor squared, $D(a)^2$, for each model. The EDE1 and EDE2 models differ from $\Lambda$CDM by up to 13% and 17% on large scales respectively, with the ratio showing a slight dependence on redshift. But the differences between the models on small scales (high $k$) are more modest, reaching at most around 5%. Using the linear growth factor in this way helps to isolate the impact of the different expansion histories in the models (see Jennings et al. 2010 for a more extended discussion of this comparison). When plotted in this way, the ratios of power spectra measured at different redshifts coincide. The
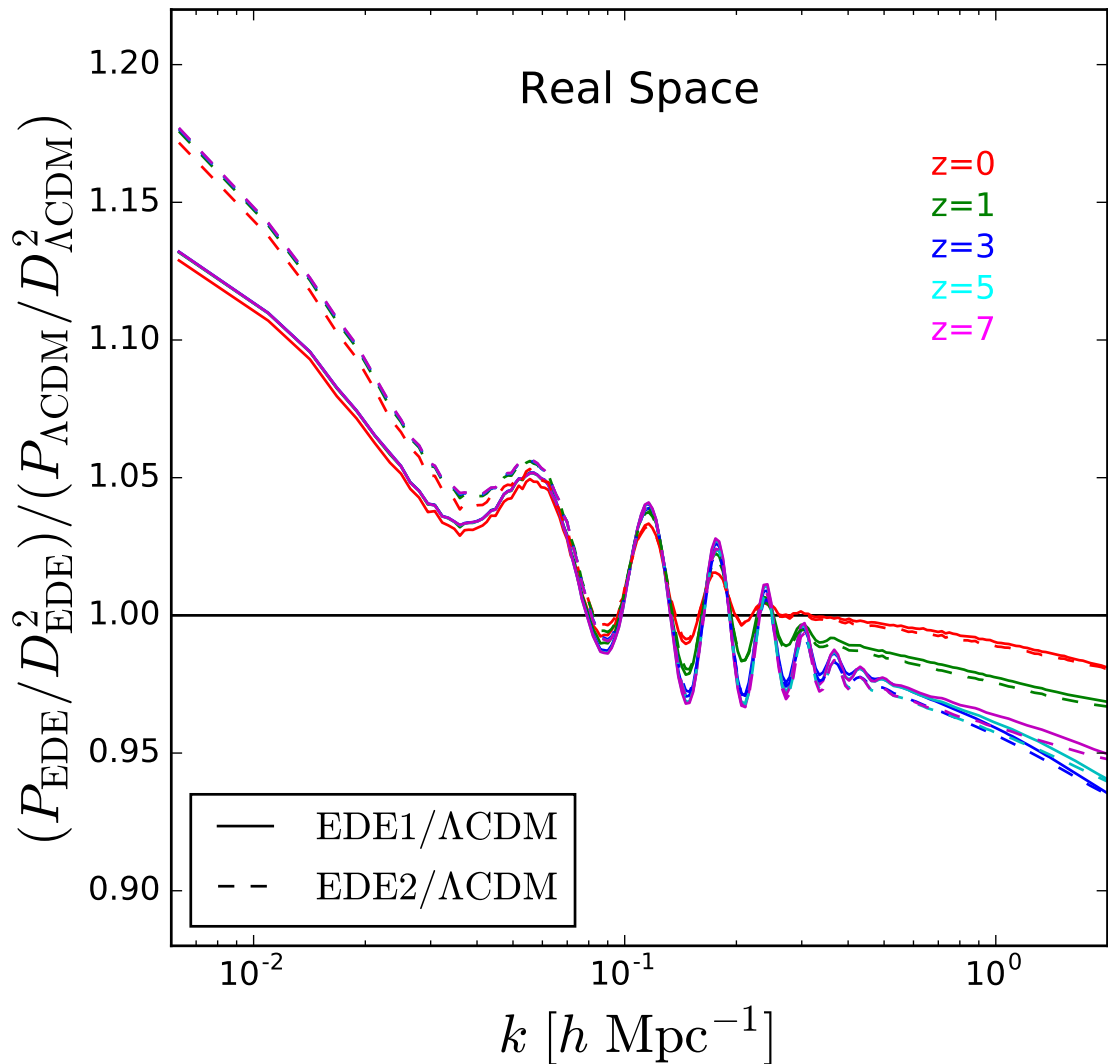
Figure 2.8: The ratio of matter power spectra measured in real space in the EDE1 and EDE2 simulations to those in ΛCDM. This ratio is plotted after taking into account differences in the linear growth factor at a fixed redshift between the models. The differences on large scales (small $k$) show that it is important to use a linear theory power spectrum in the simulations that is consistent with the expansion history and cosmological parameters in the EDE models.

residual differences at high wavenumbers are due to the different growth histories in the models.

The non-negligible difference in Fig. 2.8 illustrates the need to use a consistent linear theory power spectrum to generate the initial conditions in the N-body simulation rather than using a $\Lambda$CDM spectrum in all cases.

The conclusion of this subsection is that it should be possible to distinguish an EDE model from $\Lambda$CDM using the shape of power spectrum on large scales, well into the linear perturbation theory regime. The bulk of observational measurements of the power spectrum probe the clustering in "redshift" space, so next we extend the comparison to include the contribution from gravitationally induced peculiar velocities.

**The power spectrum in redshift space**

We model clustering in redshift space using the distant observer approximation. We adopt one axis as the line of sight direction and displace the particles along this axis according to the component of their gravitationally induced peculiar velocity in this direction. Even though we use a large simulation volume, there is still appreciable scatter in the clustering when viewed in redshift space, so we repeat this procedure for each axis in turn and average the results to obtain our estimate of the matter power spectrum in redshift space.

Fig. 2.9 shows the ratio of the redshift space power spectra measured in the simulations after removing differences in the linear growth factors of the Doran & Robbers cosmologies to that in $\Lambda$CDM. On large scales, the EDE power spectra are 10% - 20% higher in amplitude than the $\Lambda$CDM power spectrum, which is similar to the result found in real space. On small scales, due to the nonlinear effects, there are clear differences in the $P(k)$, but these are smaller than 5 per cent. However, unlike the case of the real space power spectra, dividing by growth factor squared does not reduce the differences between the ratios measured at different redshifts. Instead, the difference between the rations measured between the redshift space power spectra in a given pair of models increases slightly on large scales. This is because the linear growth factor does not account for all of the linear theory differences between the
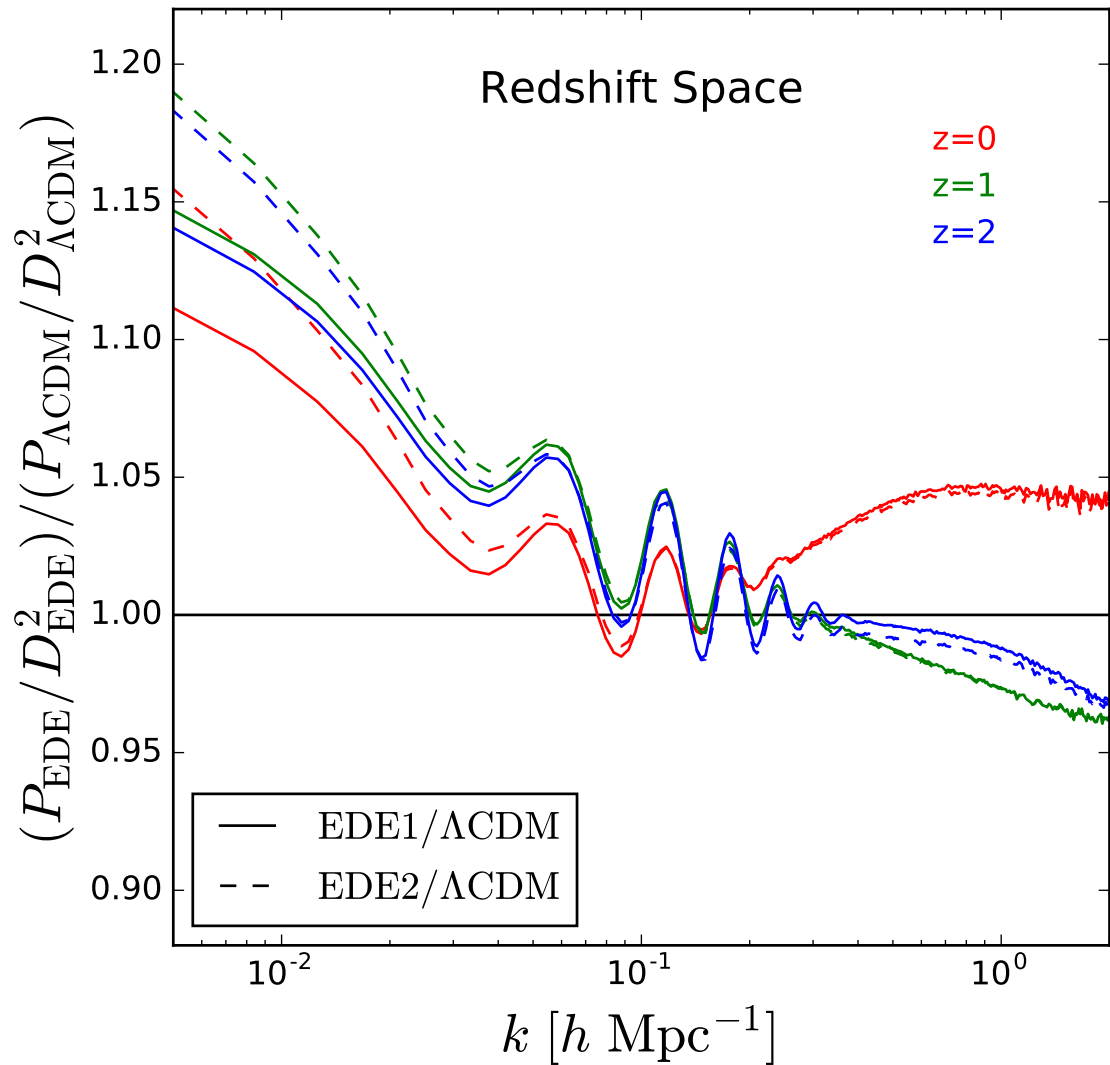
Figure 2.9: The ratio of redshift space power spectra measured in the EDE1 and EDE2 simulations after dividing by the square of the linear growth factor in each model at the redshift in question to that in ΛCDM as labelled (note that the range of redshifts compared in this plot is smaller than in Fig. 2.8).

power spectra in redshift space.

To further investigate the contributions of the velocity dispersion and nonlinearities to the form of the redshift space power spectrum, we compare the ratio of the spherically averaged power spectra in redshift space and real space in left column of Fig. 2.10. The linear theory prediction, known as the "Kaiser formula" given by $P^s(k, \mu) = P^r(k)(1 + \mu^2\beta)^2$, is plotted as black dashed lines in Fig. 2.10. Here $P_r(k)$ is the power spectrum in real-space, $\mu$ is the cosine of the angle between the line of sight and the peculiar motion of the dark matter particle and $\beta = f$ for the dark matter. The linear theory monopole ratio depends on redshift through the value of the matter density parameter. The value of linear growth rate is calculated using the parametrization $f(z) = \Omega^\gamma$, where $\gamma$ is given by Eq. 2.2.7. The error bars illustrate the scatter in $P^s(k)$ obtained by using the x, y, z directions in turn as the line-of-sight direction. At $z = 0$, the left panel of Fig. 2.10 shows that the Kaiser formula only fits the simulation results on very large scales, $k < 0.03h\mathrm{Mpc}^{-1}$, as reported by Jennings et al. (2011). The departure from the linear theory prediction is due to a combination of nonlinearities and the damping effects of peculiar velocities, even though this is often modelled as arising solely due to damping. Nonlinear effects are important for $k > 0.03h\mathrm{Mpc}^{-1}$ even though the linear regime is typically believed to hold out to $k \sim 0.1 - 0.25h\mathrm{Mpc}^{-1}$. The Kaiser prediction agrees with the simulation results over a slightly wider range of scales at higher redshifts because the nonlinear effects are smaller than they are that at $z = 0$. In the right panel of Fig. 2.10 we plot the ratio of the quadrupole to monopole moments of the redshift space power spectrum, $P_2^s(k)/P_0^s(k)$, for each cosmology at $z = 0$, 1 and 2. The Kaiser limit agrees with the simulation results for $k < 0.05h\mathrm{Mpc}^{-1}$ at $z = 0$ which is a slightly higher wavenumber than was the case for the monopole ratio. The departures from the redshift space distortions expected in $\Lambda$CDM (shown by the grey lines in Fig. 2.10) are small, and well within our estimated errors.

### 2.3.2 Halo mass function

The mass function of dark matter halos, defined as the number of halos per unit volume with masses in the range $M$ to $M + dM$, $n(M, z)$, is an important charac-
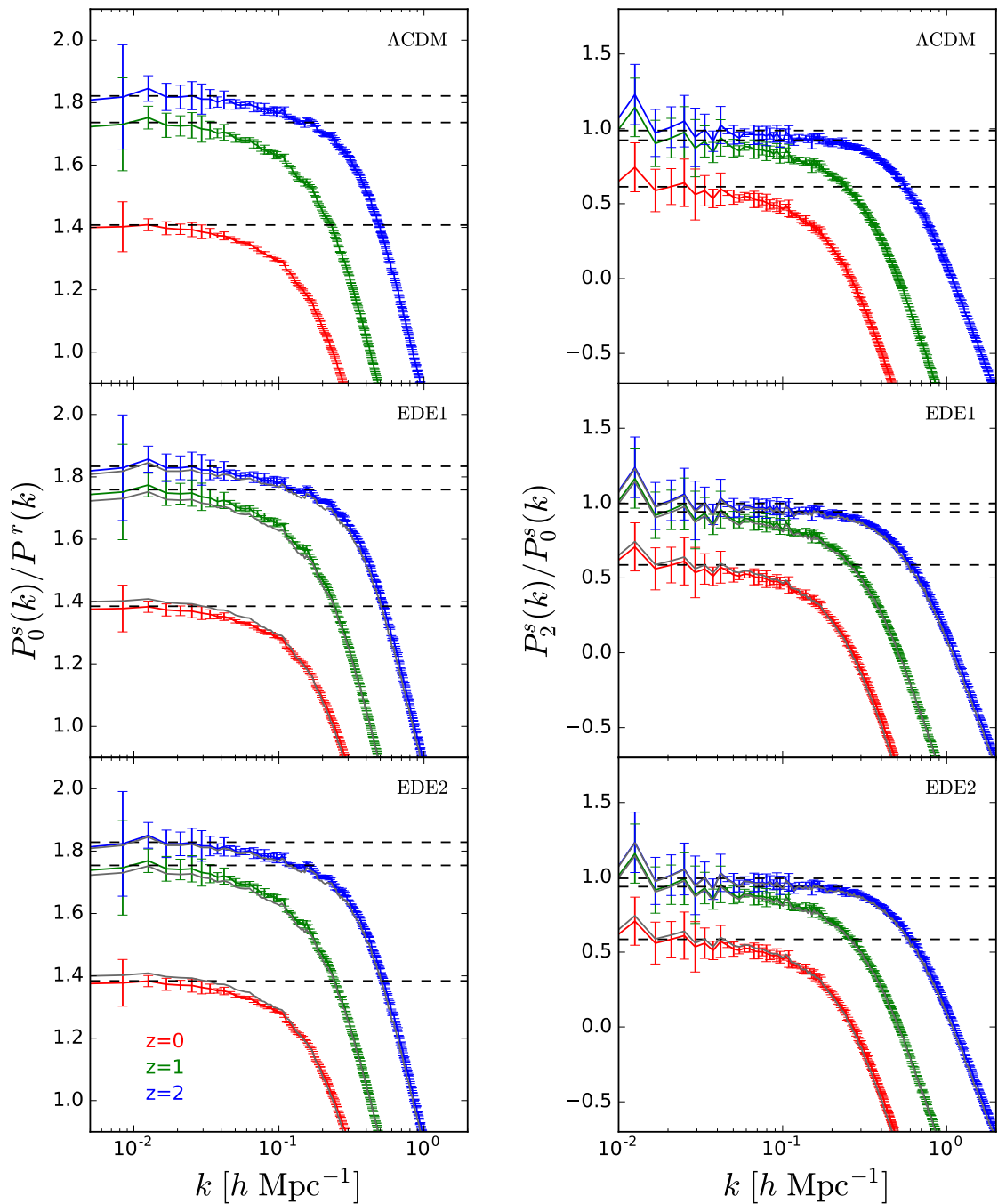
Figure 2.10: The distortion of clustering due to peculiar velocities. Left panel: the ratio of the monopole redshift power spectra to real space power spectra measured from the N-body simulations at $z = 0, 1$ and 2. Different colours show the results for different redshifts as labelled. The dashed lines show the linear theory prediction. Right panel: the ratio of the quadrupole to monopole moments of the redshift power spectra measured from the simulations. Each panel shows the result for a different model as labeled. For comparison, the $\Lambda$CDM measurements are reproduced as grey lines in the EDE1 and EDE2 panels
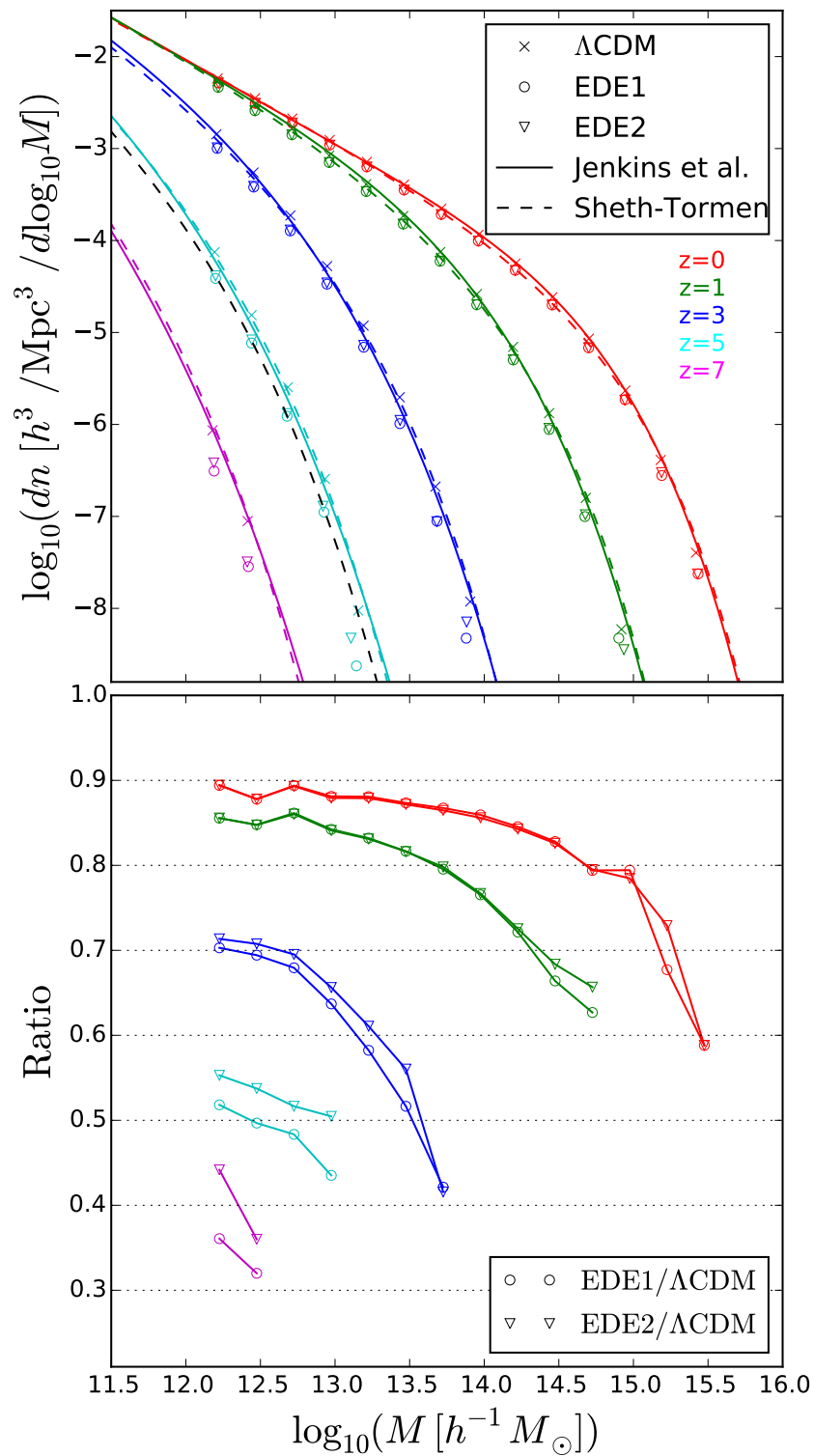
Figure 2.11: The mass function of dark matter halos measured from the simulations. The upper panel shows the halo mass functions at different redshifts. The crosses show ΛCDM, circles EDE1 and triangles EDE2. The solid and dashed lines show the Jenkins et al. and Sheth-Tormen mass functions respectively for ΛCDM. The lower panel shows the ratio of dark matter halo mass functions in the EDE1 and EDE2 cosmologies to that measured in ΛCDM.

teristic of the dark matter density field which is affected by the expansion rate of the Universe.

We use the friends-of-friends (FOF) algorithm (Davis et al., 1985) which is built into the L-GADGET2 code to identify dark matter halos, using a linking length of $b = 0.2$ times the mean inter-particle separation. We retain FOF groups down to 20 particles. In Fig. 2.11 we plot the halo mass functions measured from the ΛCDM, EDE1 and EDE2 simulations at $z = 0, 1, 3, 7$. For comparison we also plot the Jenkins et al. (2001) and Sheth & Tormen (1999) mass functions evaluated for ΛCDM. The lower panel of Fig. 2.11 shows the ratio of the mass functions measured in the EDE cosmologies to that in ΛCDM. The differences in the mass functions at low redshift ($z \leq 1$) are small, in agreement with results of Francis, Lewis, & Linder (2009). The EDE mass functions agree with ΛCDM to within 20% for halos with masses around $10^{12.0}$–$10^{13.5} h^{-1} M_{\odot}$ at $z = 1$.

The difference between the halo mass functions in EDE and ΛCDM increases with increasing redshift. This is due in part to the difference in the linear growth factors getting larger between the EDE and ΛCDM cosmologies going back in time from the present day. Also, because the simulations have a fixed mass resolution, the results probe rarer halos with increasing redshift. The abundance of these objects is sensitive to the matter power spectrum at smaller wavenumbers, where we found the largest differences between EDE and ΛCDM. At $z = 7$, ΛCDM predicts 2.5 times as many halos as are found in the EDE cosmologies.

This prediction could be tested by using a proxy for the halo mass function at high redshift, such as the galaxy luminosity function (Jose et al. (2011) proposed a similar test to probe the mass of neutrinos). To make the connection to the observable Universe, a model is needed to connect the mass of a dark matter halo to the properties of the galaxy it hosts. We have evaluated this approach by carrying out an abundance matching exercise between the halo mass functions and the observed luminosity function of galaxies in the rest-frame ultra-violet. This simple procedure assigns one galaxy to each dark matter halo, ignoring any contribution from satellite galaxies. The translation between halo mass and galaxy luminosity can be described by a mass-to-light ratio. Despite the large differences in the halo
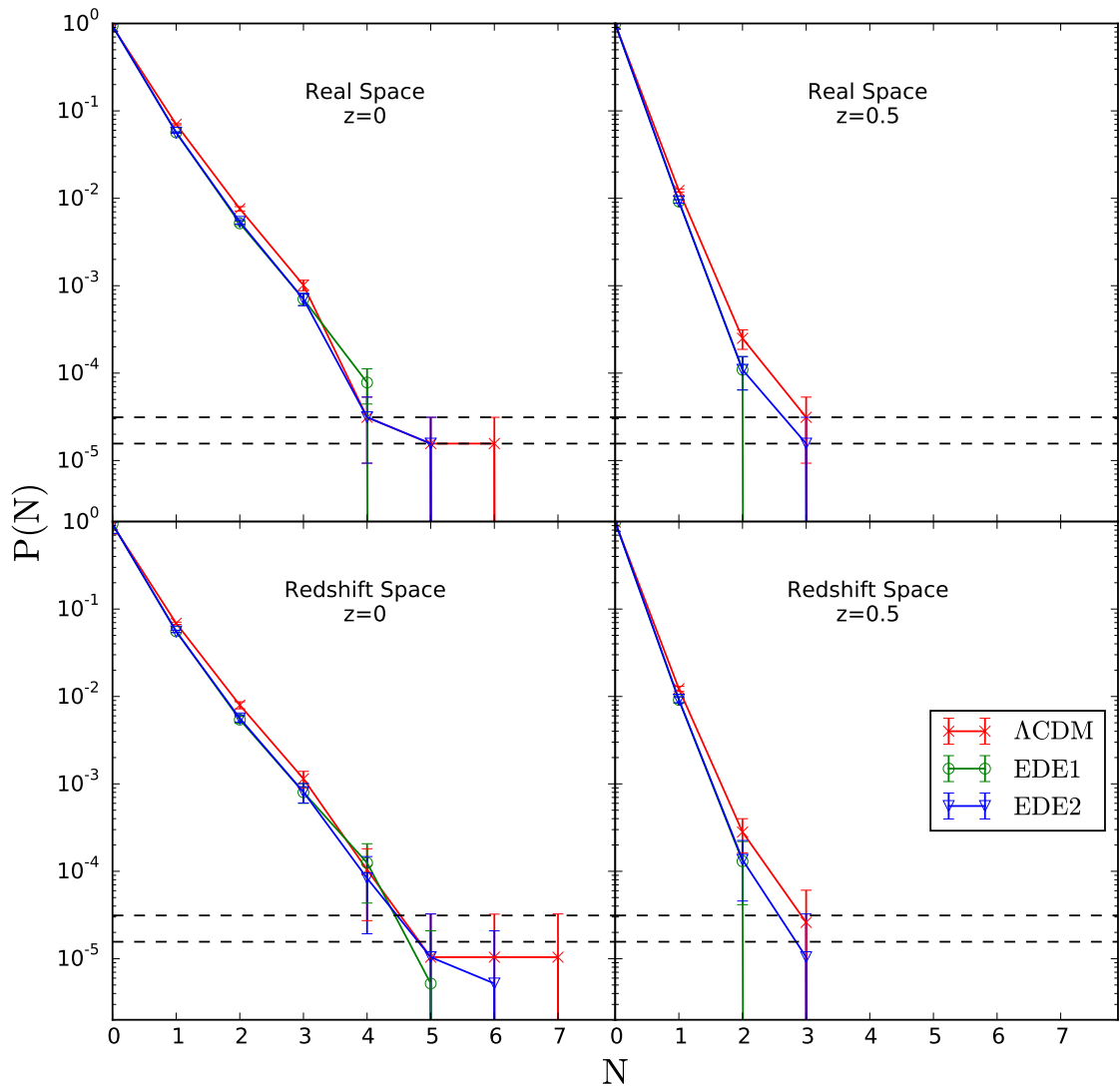
Figure 2.12: The counts in cells distribution for extreme structures. The probability distribution of finding a given number of halos with mass larger than $5 \times 10^{14}$ $h^{-1} M_\odot$ in cubic cells of side 37.5 $h^{-1}$Mpc. The x-axis is the number of halos in the cell. In the upper panels, the cell counts are measured in the real space, while in the lower panels the counts are measured in redshift space. The two dashed horizontal lines in each panel indicate the probability to find one cell and two cells in the whole simulation box.

mass functions between cosmologies, the differences in the implied mass-to-light ratios are quite modest and well within the current uncertainties in our knowledge of the galaxy formation process. Hence, we conclude that any of these cosmologies could be made to match the observed galaxy luminosity function at high redshift with plausible mass to light ratios, and that it would be difficult to use the galaxy luminosity function to distinguish between the models.

### 2.3.3 Extreme structures

We have seen in Section 2.3.1 that the power spectra of the $\Lambda$CDM and EDE energy models are similar on small scales, particularly once the differences between the expansion histories in the models have been taken into account. The power spectrum is a second moment of the density field and so does not probe the tails of the distribution of density fluctuations, which could carry the imprint of differences in the growth history of fluctuations.

Fluctuations in the density field can be quantified by measuring the distribution of fluctuations smoothed over cells, commonly referred to as counts-in-cells. Rather than formally measuring the higher order moments of the counts-in-cells distribution, which rapidly becomes infeasible even with simulations of the volume used here, we instead compare the high fluctuation tails of the distributions directly in different cosmologies.

Following Yaryura, Baugh, & Angulo (2011), in order to connect more closely with observables rather than looking at fluctuations in the overall matter distribution, we consider the counts-in-cells of cluster-mass dark matter halos. In particular, we look for "hot" cells that contain a substantial number of massive halos. The choice of halo mass and the definition of hot cells is motivated by results from the two-degree field galaxy redshift survey (2dFGRS). Croton et al. (2004) identified two hot cells in the 2dFGRS. Padilla et al. (2004) found 10 groups with an estimated mass over $5 \times 10^{14} \ h^{-1} \mathrm{M}_\odot$ in each cell, by cross matching the hot cells in the galaxy distribution with the 2dFGRS Percolation Inferred Galaxy Group catalogue (2PIGG catalogue, Eke et al., 2004).

Here we use a cubical cell of side 37.5 $h^{-1}$Mpc, which corresponds to a slightly

smaller volume than the equivalent size of the spherical cell used by Croton et al. (2004). We then count the number of dark matter halos with $M_{\mathrm{halo}} > 5 \times 10^{14} \, h^{-1} \mathrm{M}_\odot$ inside each cell. We use the jackknife method to estimate the errors on the distribution of counts (Shao, 1986; Norberg et al., 2009) . Put simply, the jackknife is a resampling technique which works by systematically leaving out each subset of data in turn from a whole dataset to generate "new" subsamples. Here a subset is defined to be a volume within the simulation. Then, the overall jackknife estimate of $\delta$ can be found by averaging over all the subsamples, given by

$$\delta_{\mathrm{Jack}} = \frac{1}{N} \sum_{i=1}^{N} \delta_i, \qquad (2.3.8)$$

where $N$ is the number of subsamples. The jackknife error is calculated as

$$\sigma_{\mathrm{Jack}} = \sqrt{(N-1) \sum_{i=1}^{N} \frac{(\delta_i - \delta_{\mathrm{Jack}})^2}{N}}. \qquad (2.3.9)$$

We use 64 spatial subsamples in our analysis, dividing each side of simulation box equally into four parts.

Fig. 2.12 shows the distribution of cell counts for the three cosmologies in both real space and redshift space at $z = 0$ and 0.5. The $x$-axis gives the number of halos per cell above the specified mass limit. The $y$-axis is the normalized probability to find such a cell. In redshift space, we also considered the scatter from using the three axes in turn as the line-of-sight. The high cell count tails are very similar, but $\Lambda$CDM consistently predicts more "hot" cells. The "hottest" cells only contain 7 halos in $\Lambda$CDM at $z = 0$, which is lower than suggested by the 2dFGRS superclusters. This could be because the FOF halo mass, which we used to select the halos, does not match the halo mass estimated from the galaxy group catalog. Yaryura, Baugh, & Angulo (2011) showed that by perturbing the FOF halo mass by the systematic bias and scatter expected in the masses returned by a group finder run on a galaxy catalogue, the number of hot cells increases.

Again, the differences between the predicted count distributions are smaller than the estimated errors on the measurement and so could only be probed by a survey

covering a volume that is much larger than our simulations.

## 2.4  Conclusions

One of the main science goals of future wide field galaxy surveys is to distinguish a cosmological constant from other scenarios for the acceleration of the cosmic expansion, such as dynamical dark energy models. Here we have examined a particular class of dynamical dark energy model which display a small but non-negligible amount of dark energy at early times, which are referred to as early dark energy models. Such models could be motivated by a choice of potential for the scalar field describing the dark energy. Instead, to confront these models with the currently available cosmological constraints in an efficient way, we chose to use a simple description in which the density parameter of the dark energy is parametrized as a function of the expansion factor, the present day values of the dark energy and matter density parameters, the present equation of state parameter of the dark energy and the asymptotic value of the density parameter of dark energy at early times. Once constrained, the model can be described by the resulting time dependence of the equation of state parameter.

The step of constraining the early dark energy model to reproduce current observations is a critical one. In fact, the best fitting models, even with the observational constraints available today favour models *without* any dark energy at early times, a conclusion that has already been reached by other studies (Planck Collaboration et al., 2014). Nevertheless, within the range of models that remain compatible with current data, it is possible to find examples with interesting amounts of early dark energy. Increasing the amount of early dark energy in the model tends to favour a more negative equation of state parameter at the present day than the canonical $w = -1$ which corresponds to the cosmological constant. We have investigated two models which, whilst not best fitting models, are still compatible with the observations at the $1 - \sigma$ (EDE1 with 1% of the critical density in dark energy at early times) and $2 - \sigma$ levels (EDE2 with 2% of the critical density in dark energy at early times); both models have $w_0 = -1.2$.

Previous simulation work on early dark energy models suggested that a clear signature that could be testable against $\Lambda$CDM is the halo mass function (Francis, Lewis, & Linder, 2009; Grossi & Springel, 2009). In a simple picture, the presence of a small but unignorable amount of dark energy at early epochs increases the rate at which the universe expands, making it harder for structure to form. If the models are set up to have the same value of $\sigma_8$ today, this means that structure has to form at a smaller expansion factor or earlier time in the early dark energy model. Hence, a larger number density of massive haloes is predicted in early dark energy models compared to $\Lambda$CDM.

Our results show that this simple picture of early structure formation with early dark matter is not a generic feature of these models. After constraining the models against current observations, we find that the evolution of the linear growth rate of fluctuations in the early dark energy models is remarkably close to that in $\Lambda$CDM. At the earliest epochs, the EDE2 growth rate exceeds that in $\Lambda$CDM by just 2% before lagging behind until catching up around $z \sim 0.8$ and then exceeding the $\Lambda$CDM growth rate by less than 0.5%.

The dark matter halo mass function in the early dark energy simulations shows *fewer* massive haloes than we find in the $\Lambda$CDM simulation. This difference in the halo mass function could be tested using the high redshift galaxy luminosity function (as suggested by Jose et al. (2011) to probe the nature of massive neutrinos). The difference in halo abundance is, however, modest, and could be accounted for by our lack of knowledge of the relevant galaxy formation physics. We find a small difference in the abundance of "hot cells" in the distribution of dark matter halos between early dark energy and $\Lambda$CDM, though this will be challenging to measure, requiring huge survey volumes.

The cleanest signature we have found of the presence of dark energy at early times is in the shape of the matter power spectrum. The more rapid expansion rate around the epoch of matter radiation equality in early dark energy models compared to $\Lambda$CDM changes the shape of the turn over in the matter power spectrum (Jennings et al., 2010). This effect is visible in the linear theory power spectrum and is present on scales on which we would expect scale dependent effects in galaxy

bias to be small (Angulo et al., 2008). To probe this effect it will necessary to retain the full shape information for the galaxy power spectrum, rather than isolating the scale of the baryonic acoustic oscillation feature (Sánchez, Baugh, & Angulo, 2008). Tentative measurements of the matter power spectrum on the scale of the turnover have already been made by the WiggleZ Dark Energy survey (Poole et al., 2013). Future large-area radio surveys conducted with the SKA pathfinder experiments, MeerKAT and ASKAP have the potential to probe the existence of early dark energy by providing more accurate measurements of the turnover in the power spectrum.

# Chapter 3

# Haloes and subhaloes in $f(R)$ gravity

## 3.1 Introduction

The observed accelerated cosmic expansion is one of the most puzzling problems in modern physics (e.g., Weinberg et al., 2013). In less than twenty years, it has motivated the proposal of a huge number of models. Apart from the current standard $\Lambda$CDM paradigm, in which the acceleration is driven by a cosmological constant $\Lambda$, such models are divided roughly in two classes. The first class introduces new physics in the particle sector and suggests that the acceleration is due to some new matter species, often known as dark energy. The second class proposes new physics in the gravity sector, so that the standard theory of gravity, Einstein's General Relativity (GR), is modified on cosmological scales to accommodate the accelerated expansion. This latter class of theories are commonly referred to as modified gravity (Clifton et al., 2012; Joyce et al., 2015) which is increasingly becoming an active research area.

For over a decade, the well-known $f(R)$ gravity (Carroll et al., 2004, 2005) model has been a leading modified gravity candidate to explain the cosmic acceleration, although it actually has a much longer history in other contexts. It is a subclass of the more general theory called the chameleon theory (Khoury & Weltman, 2004), in which an extra scalar degree of freedom is invoked, that can mediate a modification

to the standard gravitational force of GR (known as the fifth force). This deviation from GR is not necessarily ruled out by local experiments, as the theory can employ the chameleon mechanism (Khoury & Weltman, 2004) to suppress the fifth force in dense environments such as the Solar System (see below for more details about this so-called chameleon screening). This means that the theory could pass local gravity tests. However, in less dense environments, such as those encountered on cosmological scales, the deviation from GR becomes sizeable, which means that cosmology can provide a unique means to probe new physics of this kind.

There are several important features of $f(R)$ gravity, some of which seem to have not been emphasised enough. Firstly, it is a well accepted perception that $f(R)$ gravity is flexible and, thanks to its 4th-order field equations, can, in principle, accommodate arbitrary background cosmologies (see, for instance, He & Wang, 2013, for a concrete example of $\Lambda$CDM background cosmology). In spite of the general impression that '$f(R)$ gravity can accelerate the cosmic expansion', it should be noticed that there is no necessary connection between the 'acceleration' and 'modified gravity' parts of $f(R)$ gravity: the well-studied model of Hu & Sawicki (2007), as an example, can essentially be written as a cosmological constant *plus* a modification to the GR gravitational law. In this sense, $f(R)$ gravity is not a 'better' model than $\Lambda$CDM, but rather one with a different nature of gravity, the study of which can shed light on the question why GR is successful and whether cosmological data can disapprove it.

Secondly, the chameleon screening in $f(R)$ gravity is a mechanism that 'could work', but not necessarily 'will work' – whether it works depends on the system under consideration and the functional form of $f(R)$. Again, taking the Hu & Sawicki (2007) model for example: how efficiently the screening works is determined by a model parameter $|f_{R0}|$ (and another parameter $n$ which is often fixed; see below). Increasing this parameter makes it less likely for the screening to be effective. Values of $|f_{R0}| \lesssim 10^{-6}$ are more difficult to distinguish from GR using cosmological observations, implying a limit of cosmological constraints. On the other hand, there are recent claims that $|f_{R0}| = 10^{-6}$ could be in tension with astrophysical observations (see, e.g., Jain et al., 2013). Given that the chameleon mechanism works with

different efficiency in different environments, it is critical to examine whether these stringent constraints become weaker when the environments of the astrophysical systems are more accurately modelled. The same could be said about terrestrial tests of the chameleon theory (see, e.g., Brax et al., 2007a,b, for references to some pioneering works in this direction).

For this reason, the Hu & Sawicki (2007) $f(R)$ gravity model with $|f_{R0}| = 10^{-6}$ could be considered as being *borderline* between cosmological and astrophysical constraints: for higher values the model will probably have trouble with local and astrophysical tests, and for lower values the model is likely to be no longer interesting cosmologically. Here, we suggest a 'bisection' approach to the study of $f(R)$ gravity: we first conduct a detailed investigation of the cosmological and astrophysical implications of the model with $|f_{R0}| = 10^{-6}$, and then push the study and the resulting constraints to larger or smaller values based on the outcome. We hope to use this chapter, in which we will concentrate on the cosmological aspects, as an initial step in this direction, to motivate further, more in-depth, studies.

In this work, we employ one of the highest-resolution N-body simulations of $f(R)$ gravity currently available to study its effects on the properties of dark matter haloes and their subhaloes. These are the fundamental building blocks of the large-scale structure of our Universe and are closely connected with cosmological observations such as galaxy surveys. Previous studies have shown that the model considered here makes rather similar predictions to GR for many other cosmological observables, such as the matter and velocity power spectra (Li et al., 2013; Hellwing et al., 2013b; Zhao, 2014; Taruya et al., 2014), void properties (Cai et al., 2015; Zivick et al., 2015), redshift space distortions (Jennings et al., 2012), the integrated Sachs Wolfe effects (Cai et al., 2014) and X-ray scaling relations of clusters (Arnold et al., 2014), but the simulation resolution used have not been high enough to study haloes and subhaloes in great detail (see, e.g., Corbett Moran et al., 2015, for a recent high-resolution zoom-in simulation which has a different focus from that of this chapter).

This chapter is structured as following: In §3.2 we very briefly describe the $f(R)$ model studied here and summarise the technical specifications of our simulations. §3.3 and §3.4 present our detailed analyses of halo and subhalo properties respec-

tively, and comparisons with the $\Lambda$CDM model. Finally, we summarise and conclude in §3.5.

Throughout this chapter, we use the unit $c = 1$, where $c$ is the speed of light.

## 3.2 $f(R)$ gravity and simulations

In this section we briefly review the general theory of $f(R)$ gravity (§3.2.1), motivate the model which we focus on (§3.2.2) and describe the algorithm and technical specifications of our cosmological simulations (§3.2.3).

### 3.2.1 $f(R)$ gravity and chameleon screening

The $f(R)$ gravity model is designed as an alternative to dark energy to explain the accelerated expansion of the Universe. It generalises the Ricci scalar $R$ to a function of $R$ in the Einstein-Hilbert action,

$$S \quad = \quad \int \mathrm{d}^4 x \sqrt{-g} \, \frac{R + f(R)}{16\pi G}, \tag{3.2.1}$$

where $G$ is Newton's constant and $g$ is the determinant of the metric $g_{\mu\nu}$.

Minimising the action Eq. (3.2.1) with respect to the metric tensor $g_{\mu\nu}$ leads to the modified Einstein equation

$$G_{\mu\nu} + f_R R_{\mu\nu} - g_{\mu\nu} \left[ \frac{1}{2} f - \Box f_R \right] - \nabla_\mu \nabla_\nu f(R) = 8\pi G T^m_{\mu\nu}, \tag{3.2.2}$$

where $G_{\mu\nu}$ is the Einstein tensor, $f_R \equiv \mathrm{d}f/\mathrm{d}R$, $\nabla_\mu$ is the covariant derivative, $\Box \equiv \nabla^\alpha \nabla_\alpha$ and $T^m_{\mu\nu}$ the energy momentum tensor for matter fields. As $R$ contains second-order derivatives of $g_{\mu\nu}$, Eq. (3.2.2) has up to fourth-order derivatives. It is helpful to consider it as the standard Einstein equation for general relativity with an additional scalar field $f_R$. By taking the trace of Eq. (3.2.2), the equation of motion for $f_R$ can be obtained as

$$\Box f_R = \frac{1}{3} \left( R - f_R R + 2f + 8\pi G \rho_m \right), \tag{3.2.3}$$

where $\rho_m$ is matter density.

We consider a flat universe and focus on scales well below the horizon. On these scales, we can apply the quasi-static approximation by neglecting the time derivatives of $f_R$ in all field equations (see, e.g., Bose et al., 2015, for tests which show that this approximation works well for the model studied here). Then Eq. (3.2.3) simplifies to

$$\vec{\nabla}^2 f_R = -\frac{1}{3}a^2 \left[ R(f_R) - \bar{R} + 8\pi G(\rho_m - \bar{\rho}_m) \right], \qquad (3.2.4)$$

in which $\vec{\nabla}$ is the three-dimensional gradient operator and an overbar means we take the cosmological background value of a quantity. $a$ is the cosmic scale factor, normalised to $a = 1$ today. Similarly, the modified Poisson equation, which governs the Newtonian potential $\Phi$ in $f(R)$ gravity, can be simplified to

$$\vec{\nabla}^2 \Phi = \frac{16\pi G}{3}a^2(\rho_m - \bar{\rho}_m) + \frac{1}{6}\left[ R(f_R) - \bar{R} \right]. \qquad (3.2.5)$$

There are two distinct regimes of solutions to the above equations:

• when $|f_R| \ll |\Phi|$, the GR solution $R = -8\pi G\rho_m$ holds to a good approximation and one has $\vec{\nabla}^2 \Phi \approx 4\pi G\delta\rho_m$ where we have defined $\delta\rho_m \equiv \rho_m - \bar{\rho}_m$, as the matter density perturbation. The effect of modified gravity is suppressed in this regime, which is a consequence of the scalar field being *screened* by the chameleon mechanism (Khoury & Weltman, 2004).

• when $|f_R| \geq |\Phi|$, one has $|\delta R| \ll \delta\rho_m$ where $\delta R \equiv R - \bar{R}$, and so $\vec{\nabla}^2 \Phi \approx 16\pi G\delta\rho_m/3$. Compared with the standard Poisson equation in GR, we see a $1/3$ enhancement in the strength of gravity regardless of the functional form of $f(R)$. This is known as the *unscreened* regime, in which the chameleon mechanism does not work efficiently.

The chameleon mechanism is so named because it is most efficient in dense environments (or, more precisely speaking, regions of deep gravitational potential), where the scalar field $f_R$ acquires a heavy mass and the (Yukawa-type) modified gravitational force it mediates decays exponentially with distance so that it cannot be detected experimentally. The Solar System is one example of such an environment

where $f(R)$ gravity *might* be in the screened regime and thus viable (i.e., not yet ruled out by local gravity experiment). However, to determine whether a specific $f(R)$ model is *indeed* viable is much more difficult, because this depends on the large-scale environments of the Solar System, such as the Milky Way Galaxy and its host dark matter halo. To assess this therefore requires high-resolution numerical simulations that can accurately describe these environments, and this is one goal of this chapter. On the other hand, even if an $f(R)$ model passes local tests, there is still a possibility that it deviates significantly from GR on cosmic scales, where the chameleon mechanism is not as efficient. To study such deviations also requires accurate numerical simulations.

### 3.2.2 The $f(R)$ model of this work

In this work we study the model proposed by Hu & Sawicki (2007, hereafter HS), which is specified by the following functional form of $f(R)$:

$$f(R) = -M^2 \frac{c_1 \left(-R/M^2\right)^n}{c_2 \left(-R/M^2\right)^n + 1}, \qquad (3.2.6)$$

in which $c_1, c_2$ are dimensionless model parameters, and $M^2 \equiv 8\pi G \bar{\rho}_{m0}/3 = H_0^2 \Omega_m$ is another parameter of mass dimension 2; here $H$ is the Hubble rate and $\Omega_m$ is the present-day matter energy density in units of the critical density ($\rho_c \equiv 3H_0^2/8\pi G$). We always use a subscript $_0$ to denote the current value of a quantity unless otherwise stated.

There is no cosmological constant introduced in this model. However, when the background value of the Ricci scalar satisfies $|\bar{R}| \gg M^2$, $f(R)$ may be expanded as

$$\lim_{M^2/R \to 0} f(R) \approx -\frac{c_1}{c_2} M^2 + \frac{c_1}{c_2^2} M^2 \left(\frac{M^2}{R}\right)^n. \qquad (3.2.7)$$

When $c_1/c_2^2 \to 0$, $f(R)$ is a cosmological constant.

Under the same limitation, $|\bar{R}| \gg M^2$, we can simplify the trace of the modified

Einstein equation of this model as

$$-\bar{R} \approx 8\pi G\bar{\rho}_m - 2\bar{f} \approx 3M^2\left(a^{-3} + \frac{2c_1}{3c_2}\right). \tag{3.2.8}$$

This is approximately what we have for the background cosmology in the standard $\Lambda$CDM model, with the following mapping

$$\frac{c_1}{c_2} = 6\frac{\Omega_\Lambda}{\Omega_m}, \tag{3.2.9}$$

where $\Omega_\Lambda \equiv 1 - \Omega_m$.

By taking $\Omega_\Lambda \approx 0.7$ and $\Omega_m \approx 0.3$, we have $|\bar{R}| \approx 40M^2 \gg M^2$ today (remember that $|\bar{R}|$ is even larger at earlier times), and so the above approximation works well. Moreover, this can be used to further simplify the expression for $f_R$:

$$f_R \approx -n\frac{c_1}{c_2^2}\left(\frac{M^2}{-R}\right)^{n+1} < 0. \tag{3.2.10}$$

This can be easily inverted to obtain $R(f_R)$, which appears in the scalar field and modified Poisson equations as shown above. As a result, two combinations of the three HS model parameters, namely $n$ and $c_1/c_2^2$, completely specify the model. In the literature, however, this model is often specified by $f_{R0}$ instead of $c_1/c_2^2$, because $f_{R0}$ has a more physical meaning (the value of the scalar field today), and the two are related by

$$\frac{c_1}{c_2^2} = -\frac{1}{n}\left[3\left(1 + 4\frac{\Omega_\Lambda}{\Omega_m}\right)\right]^{n+1}f_{R0}. \tag{3.2.11}$$

We will focus on a particular HS $f(R)$ model with $n = 1$ and $|f_{R0}| = 10^{-6}$, which is sometimes also referred to in the literature as F6. Such a choice of $f_{R0}$ is made deliberately as a *borderline*: models with $|f_{R0}| \geq 10^{-5}$ are likely to already be in tension with cosmological observations (see, e.g., Lombriser, 2014, for a review of current constraints on $f(R)$ gravity), while those with $|f_{R0}| < 10^{-6}$ are generally hard to distinguish from $\Lambda$CDM.

### 3.2.3 Cosmological simulations of $f(R)$ gravity

The simulation used in this work was executed using the ECOSMOG code (Li et al., 2012). ECOSMOG is a modification to the publicly available N-body and hydro code RAMSES (Teyssier, 2002). New routines were added to solve the scalar field and modified Einstein equations in $f(R)$ gravity. This is a massively parallelised adaptive mesh refinement (AMR) code, which starts off from a uniform grid (the so-called domain grid) covering the cubic simulation box with $N_{dc}^{1/3}$ cells on each side. When the effective particle number in a grid cell exceeds a pre-defined criterion ($N_{ref}$), the cell is split into 8 daughter cells so that the code hierarchically achieves higher resolutions in dense environments. Such high resolutions are needed both to accurately trace the motion of particles and to ensure the accuracy of the fifth force solutions. The force resolution, $\epsilon_f$, is twice the size of the cell which a particle is in, and we only quote the force resolution on the highest refinement level.

The parameters and technical specifications of our simulations are listed in Table 3.1. The cosmological parameters are adopted from the best-fit $\Lambda$CDM cosmology of WMAP9 (Hinshaw et al., 2013). The simulation was evolved from an initial redshift $z_{ini} = 49$ to today, and the initial conditions were generated using the MPGRAFIC package (Prunet et al., 2008). For comparison, we ran a $f(R)$ and a $\Lambda$CDM simulation using exactly the same initial conditions and the same technical specifications (we have used the $\Lambda$CDM initial conditions for the $f(R)$ gravity simulation because these two models are practically indistinguishable at epochs as early as $z_{ini} = 49$). Unlike the early dark energy model in Chapter 2, $f(R)$ model has almost the same background evolution as $\Lambda$CDM. The gravity is only modified on low density region at late time of the Universe. So we chose a small simulation box in order to have high particle mass resolution. The small size of our simulation box implies that the properties of high-mass objects, such as their number densities, could be subject to run-by-run variations. However, the fact that our $f(R)$ and GR simulations start from the same initial conditions helps to suppress the run-by-run variation when we look at the relative difference between the predictions of the two models.

With $512^3$ particles in a box of size $L_{box} = 64h^{-1}$Mpc, this is currently the highest

Table 3.1: The parameters and technical specifications of the N-body simulations of this work. $\epsilon_\mathrm{s}$ is the threshold value of the residual (see, e.g., Li et al., 2013, for a more detailed discussion) for the convergence of the scalar field solver. Note that $N_\mathrm{ref}$ is an array because we take different values at different refinement levels, and that $\sigma_8$ is for the $\Lambda$CDM model and only used to generate the initial conditions – its value for $f(R)$ gravity is different but is irrelevant here.

| parameter | physical meaning | value |
|---|---|---|
| $\Omega_m$ | present fractional matter density | 0.281 |
| $\Omega_\Lambda$ | $1 - \Omega_m$ | 0.719 |
| $\Omega_b$ | present fractional baryon density | 0.046 |
| $h$ | $H_0/(100 \text{ km s}^{-1}\text{Mpc}^{-1})$ | 0.697 |
| $n_s$ | primordial power spectral index | 0.971 |
| $\sigma_8$ | r.m.s. linear density fluctuation | 0.820 |
| $n$ | HS $f(R)$ parameter | 1.0 |
| $f_{R0}$ | HS $f(R)$ parameter | $-1.0 \times 10^{-6}$ |
| $L_\mathrm{box}$ | simulation box size | $64\ h^{-1}\text{Mpc}$ |
| $N_\mathrm{p}$ | simulation particle number | $512^3$ |
| $m_\mathrm{p}$ | simulation particle mass | $1.52 \times 10^8 h^{-1}M_\odot$ |
| $N_\mathrm{dc}$ | domain grid cell number | $512^3$ |
| $N_\mathrm{ref}$ | refinement criterion | 3, 3, 3, 3, 4, 4, 4, 4... |
| $\epsilon_\mathrm{s}$ | scalar solver convergence criterion | $10^{-8}$ |
| $\epsilon_\mathrm{f}$ | force resolution | $1.95\ h^{-1}\text{kpc}$ |
| $N_\mathrm{snap}$ | number of output snapshots | 122 |
| $z_\mathrm{ini}$ | redshift when simulation starts | 49.0 |
| $z_\mathrm{final}$ | redshift when simulation finishes | 0.0 |
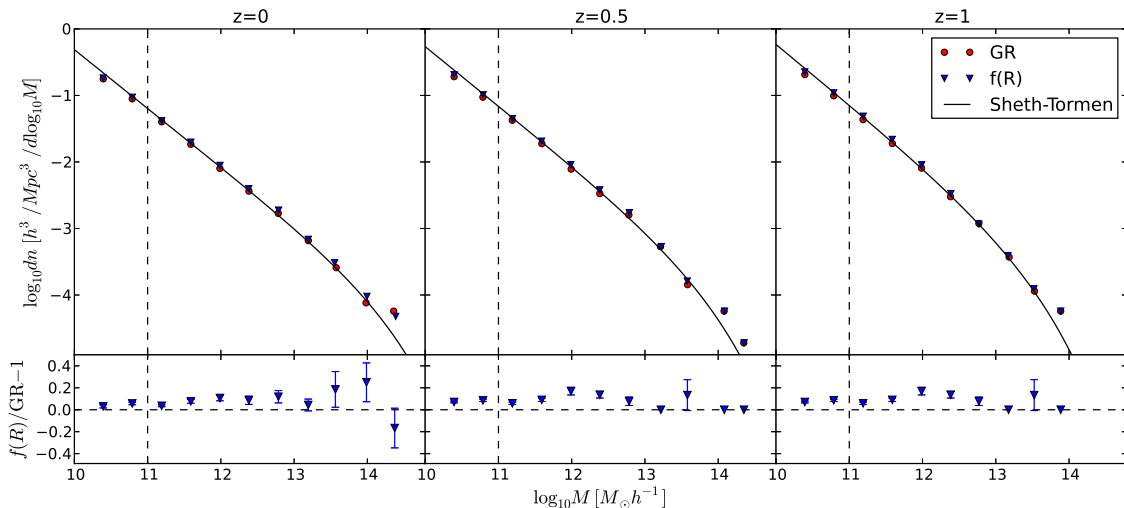
Figure 3.1: Comparison of differential halo mass functions in GR (red circles) and F6 (blue triangles) with the Sheth & Tormen (1999) prediction for GR, at three redshifts – $z = 0.0$ (left panel), $0.5$ (middle panel) and $1.0$ (right panel). The relative difference between the two models is plotted in the bottom panels. Haloes are identified using a FoF algorithm with linking length 0.2. As we only have one realisation, the error bars are estimated from subsampling by dividing the simulation box into eight subboxes of equal size; the difference between F6 and GR mass functions, $\Delta n_i$, was computed for each subbox $i$, and its mean value ($\langle \Delta n \rangle$) and standard deviations ($\sigma_{\Delta n}$) were obtained using the values from the 8 subboxes; the relative difference was then calculated as $\langle \Delta n \rangle / \langle n_{\mathrm{GR}} \rangle$, with the error bars obtained in the standard way of error propagation. The vertical dashed line indicates a cut of our FoF halo catalogue at $\sim 700$ particles, or $M_{\mathrm{FoF}} \sim 10^{11} h^{-1} M_{\odot}$, for illustrative purpose, above which there is good agreement between the GR mass functions and the Sheth-Tormen fitting formulae (better than 10%).

resolution *cosmological* simulation of $f(R)$ gravity which runs to $z = 0$. Another high-resolution $f(R)$ simulation has been conducted (Corbett Moran et al., 2015), in which the zoom-in technique was used to study the effects of $f(R)$ gravity on a Virgo-cluster-scale dark matter halo. Both simulations are purely dark matter. Recently, a hydrodynamical simulation was carried out by Arnold et al. (2015), which had a higher particle resolution and focused mainly on a different model parameter and early times, at which the model studied here is almost indistinguishable from GR.

## 3.3 Properties of dark matter halos

In this section we will concentrate on the properties of dark matter haloes measured from our simulations. Dark mater haloes are the most basic blocks of the large-scale structure and host the formation and evolution of galaxies. Therefore, the study of their properties is of great importance to the understanding of the fundamental nature of gravity. A number of halo properties have been studied in detail in the context of $f(R)$ gravity, such as the angular momentum, spin, velocity dispersion (Lee et al., 2013; He et al., 2015), velocity profile (Gronke et al., 2015) and screening (Zhao et al., 2011a; Li et al., 2012; He et al., 2014). The improved resolution of our simulations enables us to study a wider range of the physical properties of haloes.

### 3.3.1 Halo mass functions

The differential mass function, $\mathrm{d}n(M, z)/\mathrm{d}\log M$, defined as the number of dark matter haloes per unit logarithmic mass found per unit volume, is an important theoretical and observational statistic of the dark matter density field. Indeed, the abundance of dark matter haloes is sensitive to the underlying cosmological model. Both N-body simulations and (semi-)analytical formulae have been used to predict the halo mass function (see, e.g., Sheth & Tormen, 1999; Jenkins et al., 2001; Reed et al., 2007, for some examples of analytical mass function fitting formulae).

In order to compare with the above-mentioned fitting formulae, we use the friends-of-friends (FoF) group-finding algorithm to identify dark matter haloes, using a linking length of 0.2 times the mean inter-particle separation (Davis et al.,

1985).

In Fig. 3.1, we plot the differential halo mass function measured from our simulations, along with the theoretical prediction for GR from Sheth & Tormen (1999) (upper panels), and the relative difference between $f(R)$ gravity and GR (lower panels) at $z = 0$ (left), 0.5 (middle) and 1.0 (right). For the mass range we consider, the Sheth & Tormen (1999); Jenkins et al. (2001) & Reed et al. (2007) fitting formulae all agree reasonably well and so we only plot one of them. We can see from the upper panels that the fitting formula describes very well the FOF halo mass function for GR at the redshifts studied, down to a halo mass of about $2 - 3 \times 10^{10} h^{-1} M_\odot$ (which corresponds to ∼200 simulation particles). The mismatch at masses above $\sim 10^{14} h^{-1} M_\odot$ is due to the lack of volume for our small simulation box.

Fig. 3.1 (lower panels) indicates that the differential halo mass function for F6 model studied here is up to ∼20% larger than the result for a ΛCDM model with the same cosmological parameters. The difference is purely a result of the modified gravitational force in the F6 model. However, due to the strong chameleon screening in this model, the enhancement is very mild and hard to detect observationally. This is why we call F6 a borderline model – it probably represents the limit achievable by many cosmological observations for the near future, even though it might still potentially be ruled out by employing certain observables (e.g., Schmidt, 2010; Zhao et al., 2011b; Bel et al., 2015; Lombriser et al., 2015), or using astrophysical observations (e.g. Jain et al., 2013).

Inspecting the lower panels of Fig. 3.1 more closely, we observe the trend that for very massive haloes, the mass functions for $f(R)$ gravity and GR agree, which is because the chameleon mechanism works efficiently for such haloes to suppress the effects of modified gravity. Disagreement between the two models appears below some critical mass, which increases with time, because at late times the chameleon mechanism is less efficient at suppressing modified gravity. Finally, at very low halo masses, we see the trend that GR starts to produce more haloes than $f(R)$ gravity, which is a result of a larger fraction of small haloes having been absorbed into big haloes in $f(R)$ gravity (Li & Efstathiou, 2012).

It is well known that certain properties of dark matter haloes, such as the mass
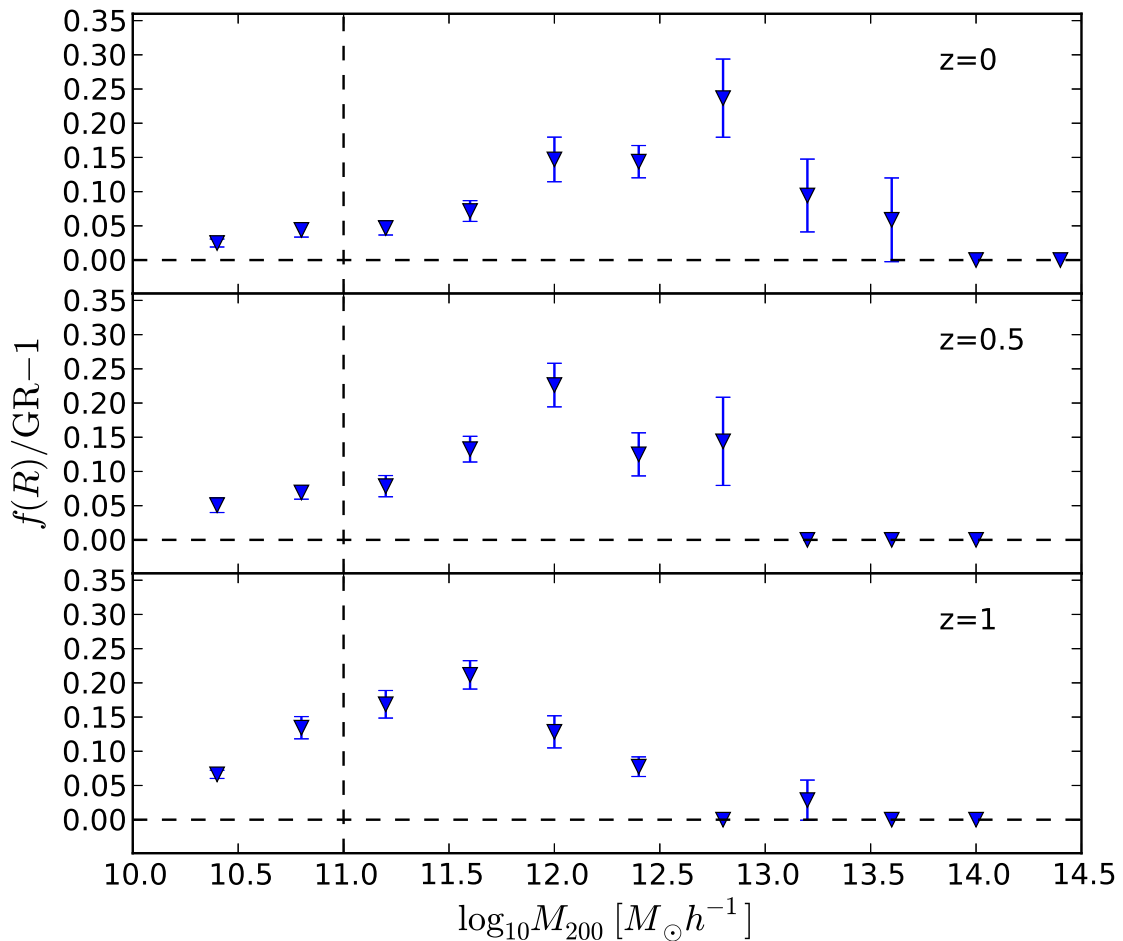
Figure 3.2: The ratios of the differential halo mass functions between $f(R)$ gravity and GR, for the same three redshifts as in Fig. 3.1. Here the halo mass is $M_{200}$, defined as the mass within the radius at which the average density 200 times the critical density. The error bars are calculated in the same way as in Fig. 3.1. The vertical dashed line indicates roughly the smallest halo mass (700 particles, or $M_{200} \sim 10^{11} h^{-1} M_\odot$) we have used in the analyses of this chapter.

function, depend on the halo definition used (e.g., White, 2001; Sawala et al., 2013). In the above, to make comparison with the Sheth-Tormen formulae, we have used FOF haloes. When studying halo properties, what is more often used in the literature is $M_{200}$, the mass inside the radius $r_{200}$ within which the average density is 200 times the *critical* density, $\rho_c$. To check whether the choice of the halo definition affects our result, we plot in Fig. 3.2 the difference between the $f(R)$ and GR mass functions when using $M_{200}$, again at $z = 0.0$ (upper panel), 0.5 (middle) and 1.0 (lower panel). We find the same qualitative features as in the lower panels of Fig. 3.1, but also some quantitative differences in the curves. In particular, the curves are smoother and better-behaved when using $M_{200}$, which may be because the FOF haloes are too irregular in their shapes and gravity is enhanced with different efficiency in different parts of the haloes, which can contaminate the screening effect expected for ideal spherical haloes (see, e.g., Li & Efstathiou, 2012; Li & Lam, 2012; Lombriser et al., 2013, 2014, for more discussion about the expected behaviour of the $f(R)$ halo mass function).

We will use $M_{200}$ in the rest of this chapter, because of its wide use in the literature. Furthermore, to ensure good resolution of halo structure, we will conservatively restrict our analysis to haloes with more than 700 particles ($M_{200} \gtrsim 10^{11} h^{-1} M_\odot$). Even cut at $\sim$400 particles, we have found that the FoF mass functions at $z = 0, 0.5$ and 1 show agreements with fitting formulae better than 10%.

### 3.3.2 Mass distribution inside haloes

The inner structure of dark matter haloes provides invaluable information about their formation history, which can also be affected by the nature of gravity. In this subsection, we look at the dark matter density profiles and concentration-mass relations for haloes in the two models.

In Fig. 3.3, we show the stacked halo dark matter density profiles at three redshifts $z = 0.0$ (left), 0.5 (middle) and 1.0 (right). The distances from halo centres, as plotted on the horizontal axis, are rescaled by $r_{200}$, and all haloes with $M \geq 10^{11} h^{-1} M_\odot$ in our simulations are divided into 5 mass ranges as indicated in the legend (the highest mass bin does not show up in the $z = 1.0$ panel, since at
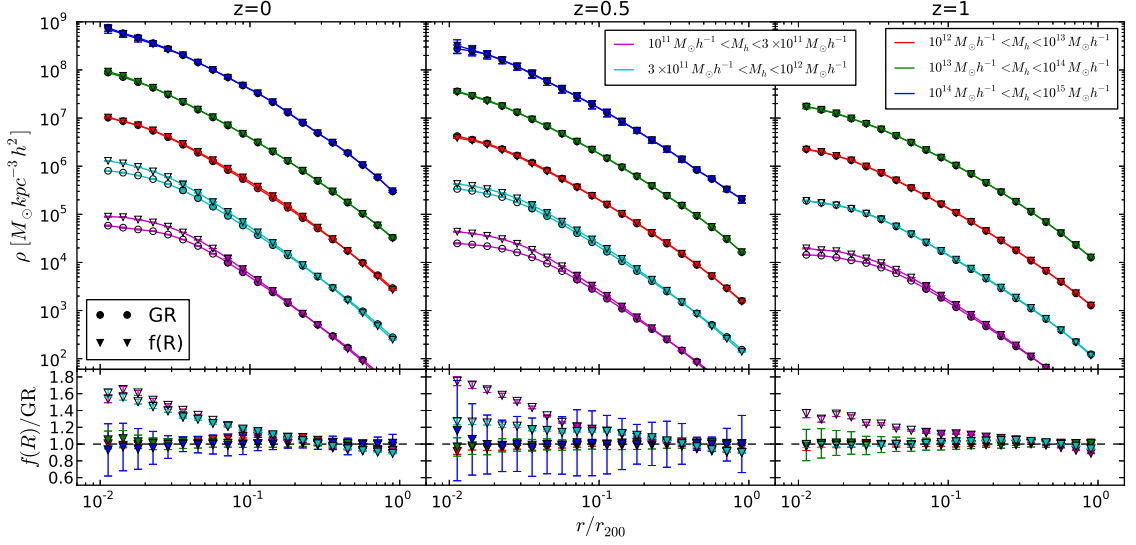
Figure 3.3: Stacked dark matter halo density profiles for five mass bins (indicated by the legend) at three epochs: $z = 0.0$ (left panel), 0.5 (middle panel) and 1.0 (right panel). *Upper panels*: density profiles – results from the GR simulation are shown as circles while the $f(R)$ results are shown as triangles; the solid curves connect the symbols and the halo mass increases from the bottom curves to the top curves. *Lower panels*: the corresponding ratios between $f(R)$ gravity and GR which deviate from unity more for smaller mass bins. Open symbols are used when the distance from halo centre is smaller than the force resolution (which happens only in the lowest mass bin). The error bars are 1-$\sigma$ standard deviations for all haloes in each radius bin. To assist visualisation, in the top panels, we have rescaled the stacked density profiles of haloes within the mass bins $10^{14} \sim 10^{15} h^{-1} M_\odot$, $10^{12} \sim 10^{13} h^{-1} M_\odot$, $3 \times 10^{11} \sim 10^{12} h^{-1} M_\odot$ and $10^{11} \sim 3 \times 10^{11} h^{-1} M_\odot$ by factors of 10, 0.1, $10^{-2}$ and $10^{-3}$ respectively. The numbers of haloes in each bin, starting from the most massive one, are respectively (numbers for the F6 simulation are in parentheses): 7 (7), 72 (78), 200 (232), 509 (586), 1558 (1714), 3758 (3936) at $z = 0$, 3 (3), 62 (62), 194 (215), 539 (624), 1665 (1968), 4224 (4554) at $z = 0.5$, and 0 (0), 48 (49), 152 (156), 508 (564), 1730 (2047), 4404 (5177) at $z = 1.0$.
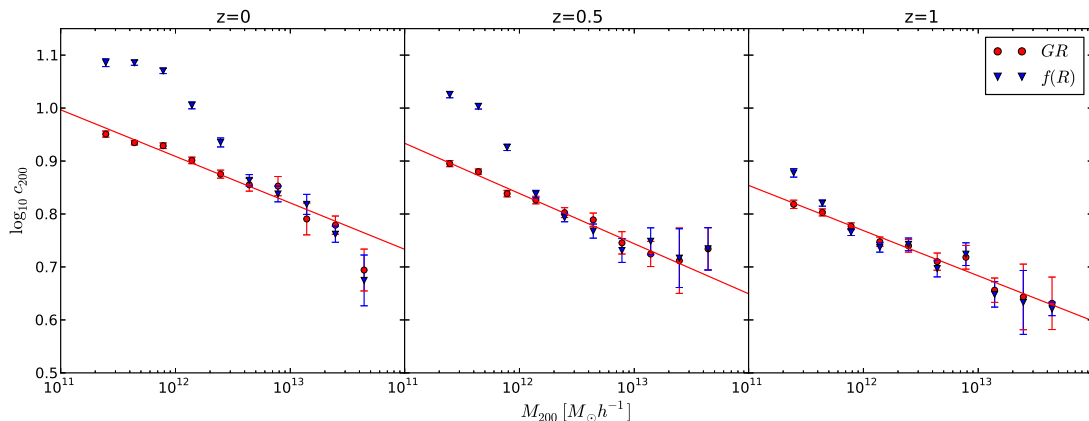
Figure 3.4: Dark matter halo concentrations $c_{200}$ as a functions of $M_{200}$ at three redshifts, $z = 0.0$ (left panel), 0.5 (middle panel) and 1.0 (right panel). Results for GR (F6) are shown using red circles (blue triangles), and the curves are power-law fits of the $c$-$M_{200}$ relations: in the case of GR (red solid line), the relation can be fitted using a single power law for the whole mass range, while for F6 this is no longer true and so we do not show any fitting. The error bars are obtained as the 1-$\sigma$ standard deviation of all haloes in each given mass bin.

that time the very massive haloes have not formed in great numbers). Note that the widths of mass bins are different, and we do not make finer subdivisions of the three most massive bins since the model differences are small there, an observation we discuss now.

From Fig. 3.3, we see that the density profiles of haloes more massive than $10^{13} h^{-1} M_\odot$ show almost no difference between the two models at all three redshifts, because these haloes are very efficiently screened by the chameleon mechanism. The haloes in the mass bin $10^{11} \sim 10^{12} h^{-1} M_\odot$ have up to 60% higher density towards their centres in $f(R)$ gravity than in GR, because the screening efficiency is weaker. Thus, Milky-Way-sized haloes have steeper inner profiles in $f(R)$ gravity. Note, however, that as the force resolution of our simulations is $\sim 2\ h^{-1}$kpc, we show the results within 5 times of it, i.e., $\sim 10\ h^{-1}$kpc, using open rather than filled symbols. We have explicitly checked that $10 h^{-1}$ kpc is roughly equal to the Power convergence radius (Power et al., 2003; Schaller et al., 2015) in our smallest halo mass bins ($10^{11} \sim 10^{12} h^{-1} M_\odot$), and is larger than the convergence radius for other halo mass bins shown in Fig. 3.3. Though the Power radius is found by testing convergence on simulations with tree (and not AMR) codes, the physics of collisional relaxation

used in its derivation is the same in our simulations, and so we use it as a reference. We conclude therefore that the region within $0.1 \times r_{200}$ of Milky-Way-sized (and smaller) haloes in $f(R)$ gravity has a significantly steeper density profile than in GR, and will further confirm this by studying the halo concentration-mass relations below.

By comparing the three panels in Fig. 3.3, it is also evident that the differences in the inner density profiles of the two models grow in time. This is as expected because the effect of modified gravity is cumulative, and also because at late times the chameleon screening is weaker in general, which leads to stronger modifications to GR. In particular, haloes with masses below $\sim 3 \times 10^{11} h^{-1} M_\odot$ already show significant discrepancy between F6 and GR at $z = 1$, and for haloes from the mass bin $3 \times 10^{11} \sim 10^{12} h^{-1} M_\odot$ the discrepancy starts at later times because of more efficient chameleon screening, although by $z = 0$ the model differences have become roughly the same for these two bins.

Next, we fit the dark matter density profiles in the two models using the Navarro-Frenk-White (Navarro et al., 1996, 1997, NFW) formula, which is given by

$$\rho(r) = \frac{\rho_{\mathrm{s}}}{(r/r_{\mathrm{s}})(1 + r/r_{\mathrm{s}})^2}, \tag{3.3.12}$$

in which $\rho_{\mathrm{s}}$ and $r_{\mathrm{s}}$ are the scale density and scale radius of the halo. The $\rho_{\mathrm{s}}$ and $r_{\mathrm{s}}$ parameters are connected to the halo mass, $M_{200}$ (or equivalently, the virial radius $r_{200}$), and concentration, $c$ (note that we have neglected the subscript in $c_{200}$ for brevity), through

$$\rho_{\mathrm{s}} = \frac{200\rho_{\mathrm{c}}}{3} \frac{c^3}{[\ln(1 + c) - c/(1 + c)]}, \tag{3.3.13}$$

$$c = r_{200}/r_{\mathrm{s}}. \tag{3.3.14}$$

In practice, we obtain the $M_{200}$ and $r_{200}$ of each halo according to the spherical over-density definition, and estimate $c$ using Eq. (3.3.14) from the best-fitting $r_s$. Lombriser et al. (2013) found that haloes in $f(R)$ gravity can be well described by

the NFW formula Eq. (3.3.12). In this work, we have further confirmed this by explicitly checking the $\chi^2$ goodness-of-fit, in which we found that Eq. (3.3.12) works almost equally well in GR and $f(R)$ gravity (with marginally smaller $\chi^2$ for haloes between $\sim 10^{12} - 10^{13} h^{-1} M_\odot$ in $f(R)$ gravity), though the concentration parameters can be different, as we shall show below.

Fig. 3.4 shows the halo concentration-mass relation, $c(M_{200})$, also at three redshifts $z = 0.0$ (left), 0.5 (middle) and 1.0 (right), from which one can see clearly that the most massive haloes have nearly the same concentration in the two models, because the effects of modified gravity are efficiently screened in these objects. It is well known from early studies that the halo concentration in $\Lambda$CDM simulations is given by a power-law function of mass (e.g., Bullock et al., 2001; Zhao et al., 2003; Neto et al., 2007; Duffy et al., 2008; Maccio' et al., 2008; Giocoli et al., 2010; Dooley et al., 2014), and our $\Lambda$CDM simulation shows the same result as illustrated by the red curves in Fig. 3.4 (neglecting the scatter at large halo masses, which is due to the small numbers of haloes there). Recent simulations and modelling have indicated that the mass dependence of the halo concentration can be more complicated and is not a simple powerlaw across the whole halo mass range (e.g., Prada et al., 2012; Sanchez-Conde & Prada, 2014; Ludlow et al., 2014; Ng et al., 2014). However, our GR simulation has too small a dynamical range to be affected by this.

In $f(R)$ gravity, however, this is no longer true. Indeed, here we find a turning mass scale $M_*$, below which the halo $c$-$M_{200}$ relation shows a clear deviation from a single power law and becomes higher than in GR. We have checked this discovery by running the Amiga Halo Finder (Knollmann & Knebe, 2009, AHF), which employs a different method to measure halo concentrations, by using the relation between the maximum circular velocity and halo mass for NFW haloes, and found good agreement. We also make an additional test by fitting the halo density profiles to the Einasto formula (Einasto, 1965; Navarro et al., 2004), because it is known in $\Lambda$CDM that the shape of spherically averaged halo density profiles deviates systematically (though only slightly) from the two-parameter NFW formula and can be better described by the three-parameter Einasto formula (Gao et al., 2008). The Einasto fitting is less sensitive to the radius range used in the fitting, but in the test we only

use radial bins outside the Power et al. (2003) convergence radius. Again, we have found very good agreement with Fig. 3.4. Finally, in Fig. 3.4 we have included all haloes, and in the last test we have also checked the results for relaxed haloes only, using the criteria proposed by Neto et al. (2007). We find that such a selection of relaxed haloes makes very little difference in the concentration-mass relation, which agrees well with the findings of Gao et al. (2008). Since the main focus of this chapter is the comparison between $f(R)$ gravity and GR, we shall not show the plots from those tests.

A possible reason for the difference in the concentration-mass relations of the two models studied here is the following: the turning mass scale, $M_*$, which itself depends time, is roughly a threshold mass for the fifth force screening in $f(R)$ gravity at each given time. Less massive haloes are unscreened and have deeper potentials than GR haloes with the same mass, which can make particles move towards the central regions and lead to higher concentrations. The increase of $M_*$ with time reflects the simple fact that as time goes on more massive haloes become unscreened.

Similar behaviour has also been found in other modified gravity theories. As an example, Barreira et al. (2014a,b) find that, for models in which the strength of gravity increases rapidly in time, halos tend to be more concentrated (and vice versa). In chameleon-type theories, including $f(R)$ gravity, the screening makes the situation more complicated, but the general picture is that haloes tend to be more concentrated if the model has had an efficient screening at early times (such as F6) because, at late times when screening is 'switched off', the potentials inside haloes deepen suddenly, and matter particles tend to fall towards the halo centre (Li & Zhao, 2010; Zhao et al., 2011a). Finally, in the phenomenological ReBEL model of Nusser et al. (2005), in which a scalar-mediated Yukawa-type fifth force helps in boosting the structure formation from early times, Hellwing et al. (2013a) notice that the halo concentration is higher for all halo masses. These authors compare the kinetic and potential energies in their virialized haloes, and find that the ratio between the two is actually smaller than in ΛCDM haloes of same masses (cf. Fig. 11 in that paper). Even though the fifth force in the ReBEL model starts to

effect from early times, the fact that it has a finite range (not longer than $1h^{-1}\mathrm{Mpc}$ in the models simulated by Hellwing et al. (2013a)) means that the enhanced gravity could not affect regions beyond $\sim 1h^{-1}\mathrm{Mpc}$: this is similar to the behaviour of the fifth force in F6 for our small haloes, which is possibly why the effect on the halo concentrations is also similar in the two cases.

Another possible reason for the different $c$-$M$ relations in F6 and GR is the different halo formation histories in the two models. As is mentioned above, haloes which form at earlier times generally have higher concentration because the mean matter density is higher when they collapse. Consider two (small) haloes of the same mass in GR and in F6: it is more likely that the latter has a larger fraction of its present-day mass assembled at later times, and thus its inner region is smaller, forms earlier and is more concentrated (in other words, a halo with mass $M_1$ in F6 is likely to have a mass $M_2 < M_1$ in GR and thus have a higher concentration than a GR halo of mass $M_1$). It would be useful to disentangle the two effects affecting halo concentrations, but this is difficult because a modified gravitational force will always simultaneously affect both the halo accretion history and halo potential, except in cases where the screening is very strong inside haloes, such as in the cubic Galileon model (Barreira et al., 2014b). We shall leave such a study for future work.

We caution that the result for F6 may not quantitatively hold for HS $f(R)$ models with other values of $n$ or $f_{R0}$, or to other $f(R)$ or chameleon models. The complicated physics that determines the concentration implies that the $c$-$M_{200}$ relation needs to be studied on a case-by-case basis in general.

### 3.3.3   Halo formation histories

The formation of dark matter haloes is a complicated process, in which frequent mergers and the accretion of smaller haloes hierarchically lead to the formation of larger haloes. In this picture, large haloes form later when the environmental density is lower, and thus have lower concentrations than small haloes, as we have seen in the previous subsection.

As the gravitational force is enhanced in $f(R)$ gravity, is has been speculated that the matter clustering is stronger and as a result dark matter haloes form earlier in
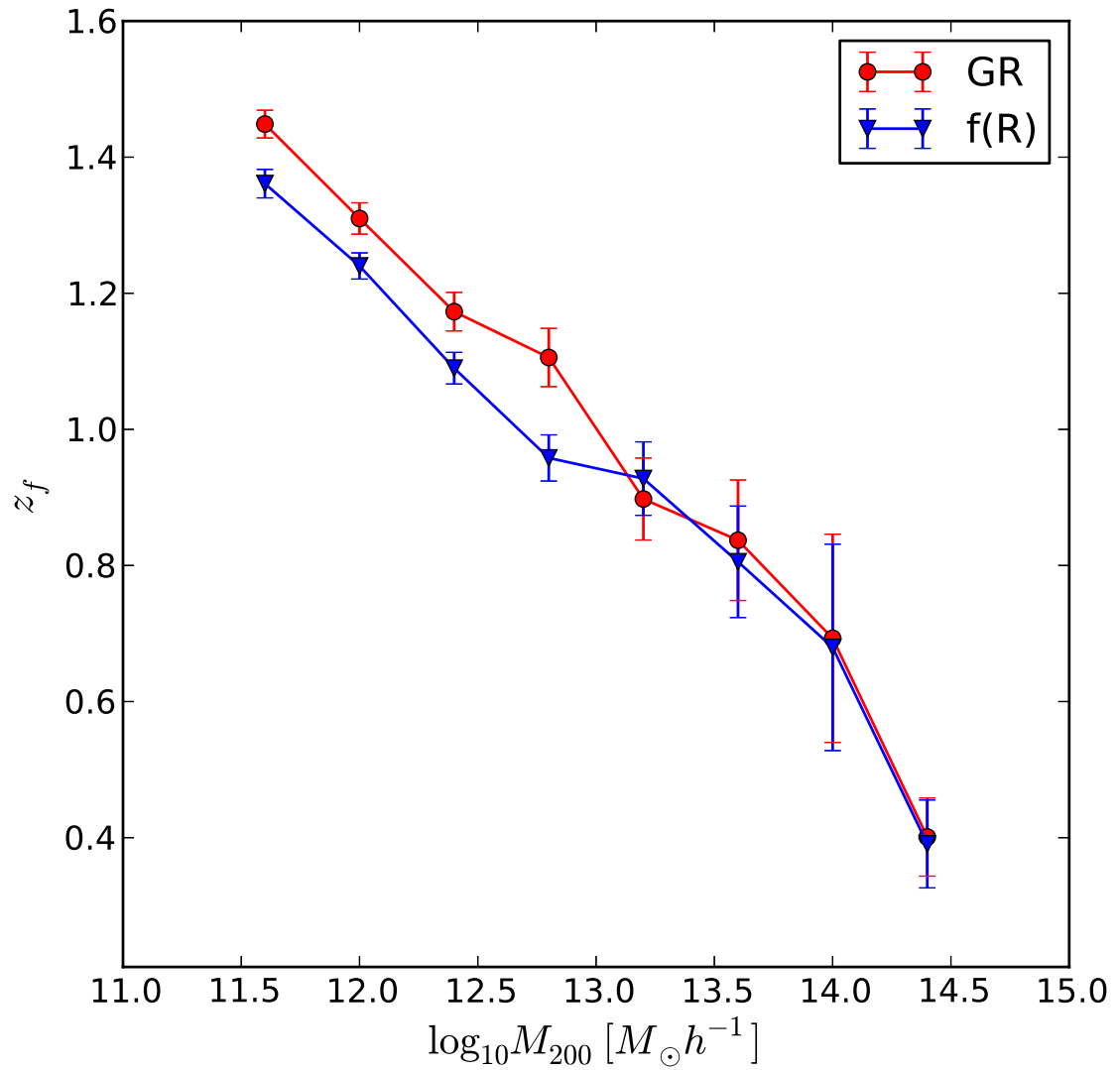
Figure 3.5: The halo formation time $z_f$ as a function of $M_{200}$, from our GR (red circles and curve) and F6 (blue triangles and curve) simulations. Error bars are 1-$\sigma$ standard deviations.

our $f(R)$ model than in GR. For example, a previous study by Hellwing et al. (2010) found that in the ReBEL model, the Yukawa-type fifth force helps to form haloes at higher redshift than in the standard $\Lambda$CDM model, and therefore can potentially move reionization to earlier times as implied by CMB observations. Here, we want to study the halo formation times in our F6 simulations.

In order to follow the growth of a halo with time, we start with the halo at the present time and identify its most massive progenitor from the previous snapshot. We repeat this procedure until the halo mass is too small to be resolved anymore, and define the halo formation time as the redshift, $z_f$, at which the most massive progenitor halo has assembled half of its mass at $z = 0.0$. This formation time has been widely used in the literature (e.g., Lacey & Cole, 1993; Gao et al., 2004), although other definitions have also been used (e.g., Wechsler et al., 2002).

In Fig. 3.5, we plot the halo formation time $z_f$ as a function of $M_{200}$. In both models, the results agree with the above hierarchical picture that low-mass haloes form earlier. When comparing the two models, we can see that haloes more massive than $10^{13}h^{-1}M_{\odot}$ form at nearly the same redshift in GR and F6, showing again that the chameleon mechanism works efficiently for these haloes to suppress the effects of modified gravity. Less massive haloes, on the other hand, form slightly *earlier* in GR than in F6. This result seems to disagree with the general pattern found in Hellwing et al. (2010) in the ReBEL model, and seems in contrast to the naive expectation that the enhanced gravitational force in F6 boosts the hierarchical structure formation.

To explain this behaviour, we need to again carefully examine the subtle differences between different models. In ReBEL, there is a Yukawa-type fifth force between particles, whose strength decays with distance but does not change in time. This implies that the fifth force starts to boost structure formation from early times, resulting in haloes forming earlier. In the case of F6, gravity is suppressed at redshift $z \gtrsim 1$, and even at $z \lesssim 1$ it is only enhanced for smaller haloes. This means that:

(i) the formation history of very massive haloes (e.g., $M \gtrsim 10^{13}h^{-1}M_{\odot}$) does not see the effect of an enhanced gravity, as we have seen above;

(ii) less massive haloes evolve in a similar manner as in GR at $z \gtrsim 1$, but grow
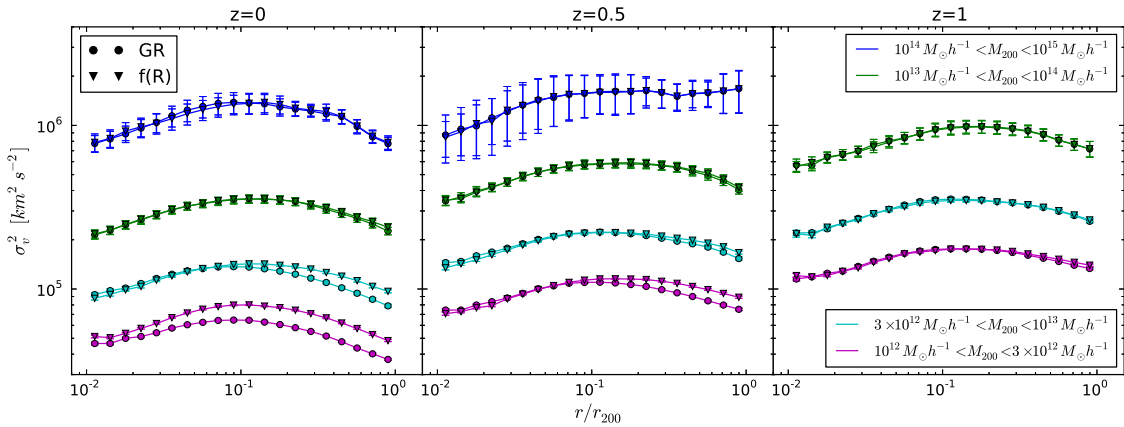
Figure 3.6: The stacked velocity dispersion profiles from our $f(R)$ (filled triangles) and GR (filled circles) simulations, at three redshifts: $z = 0$ (left panel), $z = 0.5$ (middle panel) and $z = 1$ (right panel). We show the results for four bins of the host halo mass increasing from the bottom curves to the top curves, and indicated in the legend (we have divided the mass bin $10^{12} \sim 10^{13} h^{-1} M_\odot$ into two sub-bins because this is the only bin which shows difference between F6 and GR). The solid curves simply connect the symbols, and the error bars show the 1-$\sigma$ scatter around the mean.

more rapidly at $z \lesssim 1$, and as such they are more massive than their GR counterparts at present. As $z_f$ is defined to be the time when a halo has gained half of its current mass (denoted by $M_{1/2}$), the halo would have a larger $M_{1/2}$ in F6 than in GR. But small haloes typically grow to $M_{1/2}$ at $z \gtrsim 1$, before when there is little difference between GR and F6, and so it takes the halo longer to acquire a mass of $M_{1/2}$ in F6 than in GR, which means that the halo forms *later* in $f(R)$ gravity. This, of course, is purely a result of the definition of $z_f$, and does *not* imply that matter clusters more slowly in F6.

Therefore, like the concentration, the halo formation time also depends sensitively on the nature of gravity. Even for two models in both of which gravity is enhanced, the behaviour of $c(M_{200})$ or $z_f(M_{200})$ can be qualitatively different. For this same reason, the results for $z_f$ for F6 can not be generalised to other variants of the HS $f(R)$ model or other $f(R)$ models without careful tests.

### 3.3.4 Halo velocity dispersion profiles

Before leaving this section, we study the velocity dispersion profile in our simulations, which is defined as

$$\sigma_v(r)^2 \equiv \frac{1}{\Delta N_p} \sum_{i \in \Delta r} (\vec{v}_i - \vec{v}_h)^2, \tag{3.3.15}$$

in which $i \in \Delta r$ means that particle $i$ sits in a spherical shell from radius $r - \Delta r/2$ to $r + \Delta r/2$, and $N_p$ is the number of particles within this shell. $\vec{v}_i$ and $\vec{v}_h$ are the particle and host halo velocities respectively, and the latter is calculated as the average of the velocities of the 25% most bound particles in the host halo. The halo velocity dispersion is a more direct characterisation of the potential inside a halo; it is determined by the dynamical (Schmidt, 2010; Zhao et al., 2011b) or effective (He et al., 2015) mass of a halo, and is enhanced by the modified force for unscreened haloes (Lee et al., 2013; He et al., 2015).

In Fig. 3.6 we show the velocity dispersion profiles measured from our simulations at $z = 0.0$ (left), 0.5 (middle) and 1.0 (right). Thanks to the chameleon screening, the difference between the two models for haloes more massive than $\sim 10^{13} h^{-1} M_\odot$ is almost undetectable. Haloes in the mass range $10^{12} - 10^{13} h^{-1} M_\odot$ can have significantly higher velocity dispersion in $f(R)$ gravity than in GR, and the deviation increases with the distance from the halo centre, since the screening in $f(R)$ gravity is relatively weak inside small halos, particularly in their outer regions in which matter density is low. We also notice that the enhancement of velocity dispersion is weaker at earlier times, due to stronger chameleon screening and less time for the fifth force to take effect.

The result confirms that particles bound in unscreened haloes have higher kinetic energy to balance the extra potential produced by the fifth force. This implies that measurements of galaxy velocity dispersions in galaxy groups, such as the Local Group, may not be able to give reliable estimates of the true masses of the systems. For example, to use such measurements to find the underlying mass requires a good understanding of the screening, which in turn requires an accurate knowledge of the true mass (as well as the environmental effects). Therefore, a trial-and-error

procedure would be needed to improve the mass estimation iteratively from some initial guess, and each iteration needs to be calibrated by high-resolution simulations which take into account the full environmental effects and other complexities such as irregular shapes of haloes and distributions of their massive satellites.

On the other hand, if we indeed live in an unscreened region in $f(R)$ gravity, but choose to interpret our measurements of galaxy velocity dispersions in the incorrect framework of GR, then the estimated mass will be biased high compared with its true value. We will briefly mention one of its implications below. In any case, it is clear that $f(R)$ gravity would make the already uncertain estimates of the Milky Way mass even more complicated.

## 3.4 Properties of substructures

In the previous section we analysed the simulation results of various halo properties in our F6 and GR simulations. In this section, we turn our attention to the properties of subhaloes in these models.

In hierarchical structure formation, halo merger events leave plenty of remnant structures that survive as subhaloes in the descendent haloes. As galaxies form inside haloes and migrate with them, subhaloes then exist as the host sites of satellite galaxies in galaxy groups and clusters. The properties of subhaloes and their evolution history (i.e., the subhalo merger tree) provide the backbone for models of galaxy formation (see, e.g., Baugh, 2006, for a review). The abundance and distribution of subhaloes also has important implications for the indirect detection of dark matter, for example by boosting the dark matter annihilation signal (e.g., Gao et al., 2012; Han et al., 2012a).

The fact that subhaloes form through hierarchical mergers can also be utilised to identify them. Here we will use the tracking subhalo finder Hierarchical Bound-Tracing (Han et al., 2012b, HBT) to identify subhaloes. Starting from isolated haloes at an earlier snapshot, HBT identifies their descendants at subsequent snapshots and keeps track of their growth. As soon as two haloes merge, HBT starts to track the self-bound part of the smaller progenitor as a subhalo in each subsequent
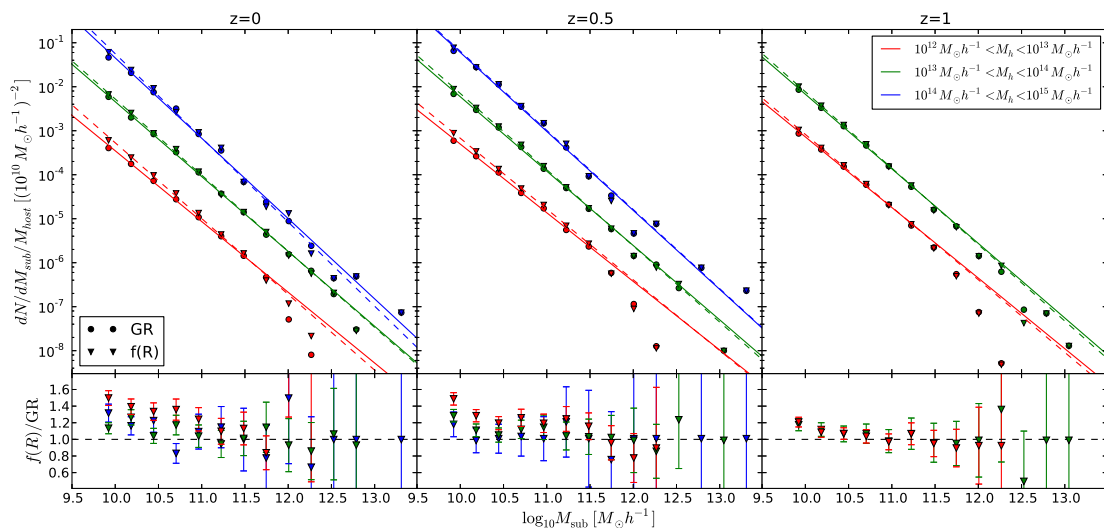
Figure 3.7: The differential subhalo mass function $\mathrm{d}N/\mathrm{d}M_{\mathrm{sub}}$ as a function of the subhalo mass $M_{\mathrm{sub}}$, at three redshifts – $z = 0.0$ (left panel), $z = 0.5$ (middle panel) and $z = 1.0$ (right panel). The lower subpanels show the ratio between the F6 and GR results, and the binning scheme of host halo masses is indicated by different colours as shown in the legends (note that the highest mass bin does not exist in the right panels because at $z = 1$ haloes more massive than $10^{14}h^{-1}M_{\odot}$ does not exist in great numbers). The error bars (only shown in the lower subpanels for clarity) are 1-$\sigma$ standard deviations in each subhalo mass bin similarly as in the halo mass function plots. For guide eyes, we also plot the power-law fitting results of the subhalo mass functions using lines with the same colours (solid for GR and dashed for F6).

snapshot. With a single walk through all the snapshots, all the subhaloes formed from halo mergers can be identified in this way. Such a unique tracking algorithm enables HBT to largely avoid the resolution problem suffered by configuration space subhalo finders (Muldrew et al., 2011; Han et al., 2012b; Onions et al., 2012). By construction, HBT also produces clean and self-consistent merger trees that naturally avoid subtle defects such as missing links and central-satellite swaps common to many other tree builders (Srisawat et al., 2013; Avila et al., 2014).

### 3.4.1 Subhalo mass functions

Similar to haloes, the abundance of subhaloes can be described by a subhalo mass function (SHMF). The SHMF is known to depend on the size of their host haloes (Gao et al., 2004; van den Bosch et al., 2005) in $\Lambda$CDM simulations, but is close to

a universal power law function of the subhalo mass, $M_{sub}$, when normalised by the host halo mass, $M_{host}$.

In Fig. 3.7 we plot the SHMF for three bins of host halo mass, $10^{12} \sim 10^{13} h^{-1} M_\odot$, $10^{13} \sim 10^{14} h^{-1} M_\odot$, $10^{13} \sim 10^{14} h^{-1} M_\odot$ (see the legends), at three redshifts, $z = 0$ (left), 0.5 (middle) and 1 (right). For clarity, the results for the highest (lowest) mass bin are shifted upwards (downwards) by a decade. A quick visual inspection of Fig. 3.7 indicates that the power-law relation holds true for the ΛCDM (circles and solid lines) and F6 (triangles and dashed lines) simulations as well, though the slope has a weak dependence on the host halo mass (lower for low-mass host haloes). To check this result, we tested HBT on a simulation using a different N-body code (described in Jing & Suto, 2002) and found the same tendency. We also tested our simulations using the Rockstar code (Behroozi et al., 2013) to identify subhaloes, but did not notice any dependence of this slope on the host halo mass. Therefore, we conclude that this is likely due to the subhalo finding algorithm we use, which finds more massive and extended subhaloes than some other algorithms (Han et al., 2012b). We note that, even though the SHMF from HBT has a lower slope than the result from Rockstar, it is consistently higher for the range of subhalo mass shown in Fig. 3.7. Because we are mainly interested in the relative differences between models in this chapter, we will leave a more detailed comparison of different algorithms to a future separate work and not show a plot for the comparison.

From Fig. 3.7 we find that the difference between F6 and GR is smaller for more massive host haloes and at earlier times, because in both cases the chameleon screening is more efficient and effects of modified gravity more strongly suppressed. Differences between the two models also tend to be larger for small subhaloes, with F6 predicting $20 \sim 50\%$ more subhaloes with $M_{sub}$ between $10^{11}$ and $10^{10} h^{-1} M_\odot$ than GR in host haloes of mass $10^{12} \sim 10^{13} h^{-1} M_\odot$. This implies that the enhanced gravity in the $f(R)$ model studied here can help produce a substantially higher abundance of substructures in Milky-Way-sized dark matter haloes. We will discuss the implication of this in the context of Milky Way satellite abundances below when discussing the subhalo velocity function.

Note that an enhanced gravity will not only boost the clustering of matter and

formation of subhaloes, but can also increase the stripping of matter from subhaloes inside haloes (and thus decrease subhalo masses). Our results above suggest that the latter effect is subdominant.

### 3.4.2 Subhalo spatial distributions

Next we focus on the spatial distribution of subhaloes inside their host haloes. Naturally, one expects this distribution to depend on the nature of gravity,though this dependence can be weakened by the chameleon screening by the host haloes in $f(R)$ gravity.

Gao et al. (2004) showed that the spatial distribution of subhaloes does not have a significant dependence on their host halo masses. In our $\Lambda$CDM simulations we have found the same result, as shown in Fig. 3.8, in which we plot the cumulative radial number distributions of subhaloes as circles for $\Lambda$CDM. We show in different colours the results for three mass bins of host haloes, all at $z = 0$, which agree well with each other.

To see the effect of $f(R)$ gravity, we also plot the corresponding results from the F6 simulation in Fig. 3.8 using triangles. There is very little difference from the GR results, possibly because of the efficient screening. Notice that here we have only shown results for host haloes more massive than $10^{13}h^{-1}M_{\odot}$, in which the modified gravity effects are strongly suppressed as we have seen above. The results for smaller host haloes are not shown since they are noisier due to resolution limitations.

### 3.4.3 Subhalo velocity function

Subhaloes reside in the high-density environments within their host haloes, and experience constant tidal stripping, which strips mass from their outer parts. Their mass could change significantly during their evolution. Therefore, in the literature people often use the maximum circular velocity $V_{\mathrm{max}}$ instead, because it depends primarily on the inner part of a (sub)halo.

Following Gao et al. (2004), in Fig. 3.9 we plot the differential abundance of subhaloes as a function of $V_{\mathrm{max}}$, also known as the subhalo velocity function (SHVF).
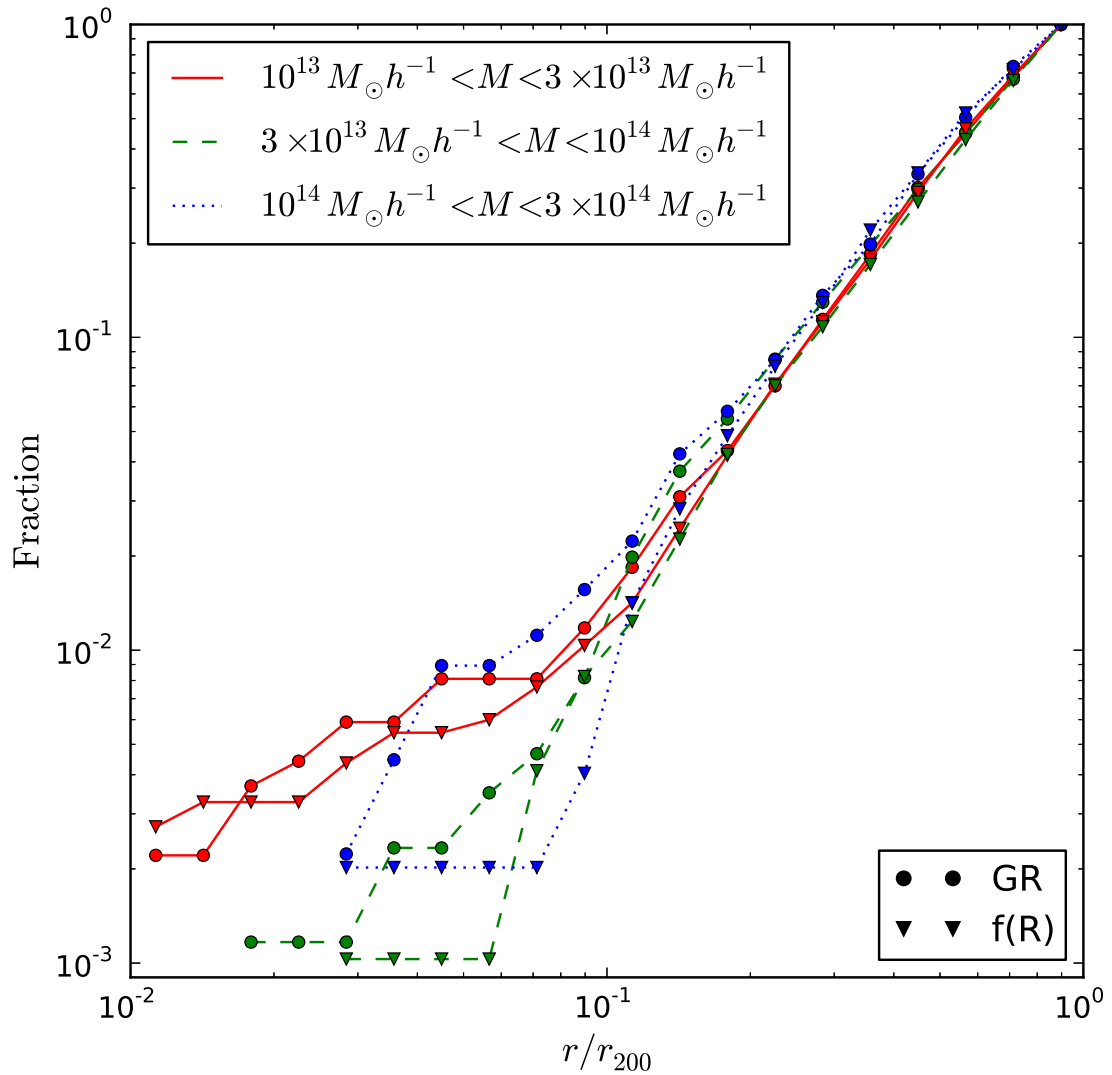
Figure 3.8: The cumulative radial number distributions for subhaloes, for three mass bins of their host haloes as indicated by the legends. The vertical axis is the fraction of subhaloes within $r/r_{200}$, and we show the results for both F6 (triangles) and GR (circles) at $z = 0$.
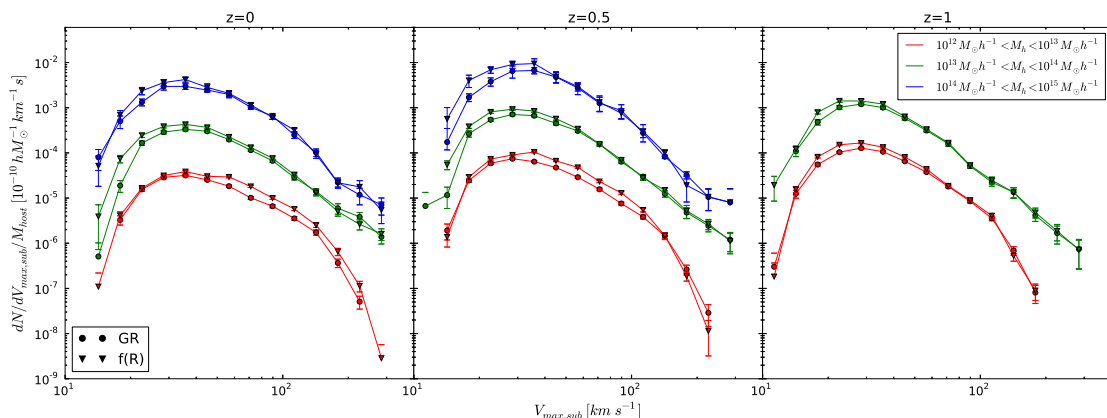
Figure 3.9: The differential subhalo velocity functions from our $f(R)$ (filled triangles) and GR (filled circles) simulations, at three redshifts: $z = 0$ (left panel), $z = 0.5$ (middle panel) and $z = 1$ (right panel). We show the results for three bins of the host halo mass increasing form the bottom curves to the top curves, and indicated in the legend; the solid curves simply connect the symbols. Note that the number of subhaloes in each bin is normalised by the total mass of the host halo. The results for the highest (lowest) host halo mass bin are artificially shifted upwards (downwards) by a decade to make the plot clearer. Error bars show the 1-$\sigma$ scatter around the mean.

The $\Lambda$CDM results in the range of 30 km/s $\lesssim V_{\max} \lesssim$ 200 km/s are well described by a universal power-law function, in agreement with findings in the literature (e.g., Gao et al., 2004; Dooley et al., 2014) (note that we have shifted the curves for different host halo mass bins for clarity), and drop off at small (large) $V_{\max}$ is due to the resolution limit (finite box size).

In $f(R)$ gravity, the qualitative behaviour of the SHVF is similar, but the enhanced gravity leads to quantitative differences. For more massive host haloes, the difference is most significant at small $V_{\max}$, which correspond to smaller subhaloes that are less screened and therefore have formed in higher abundances; in contrast, larger subhaloes, with larger $V_{\max}$, are better screened and so their abundances do not change significantly from the GR predictions. For less massive host haloes, there is a noticeable boost in the subhalo abundance even for large subhalo $V_{\max}$, since the host haloes have become less screened since earlier times and substructures have more time to grow there. This dependence on host halo mass in principle implies a deviation from a universal SHVF, although the effect we see in Fig. 3.9 is fairly weak.

The enhanced SHVF at $V_{\max} \gtrsim 30\,\mathrm{km/s}$ for host haloes with mass of $\sim 10^{12} h^{-1} M_\odot$ seems to suggest that the missing massive satellite problem of the Milky Way galaxy is worse in $f(R)$ gravity, since in the latter the observed number of dwarf galaxies remains the same while the theoretically predicted number of massive subhaloes is larger. Wang et al. (2012) argue that the missing satellite problem is not serious enough to motivate a revision to the $\Lambda$CDM paradigm, but what we saw above in Fig. 3.9 certainly seems to make $f(R)$ gravity disfavoured. However, there are complicated issues which preclude a definite conclusion. For example, most measurements of the Milky Way halo actually predict its dynamical mass, which can be 1/3 heavier than the true mass in $f(R)$ gravity – hence, with a given rotation speed of the Milky Way disk, the actual mass of the halo could be smaller than what we currently think. Also, galaxy formation can also be different in $f(R)$ gravity, so that the way in which galaxies populate massive subhaloes might be different, making a direct comparison with $\Lambda$CDM even harder. We will leave detailed studies of these issues to future works.

## 3.5 Discussions and conclusions

To briefly summarise, in this chapter we have employed a very high-resolution simulation to study the properties of dark matter haloes and subhaloes of a $f(R)$ gravity model. This model is a variant of that proposed by Hu & Sawicki (2007), with parameters $n = 1$ and $|f_{R0}| = 10^{-6}$. We argue that this is a borderline model that should be studied as a first step towards a more rigorous constraint on $f_{R0}$ combining cosmological and astrophysical observations. We regard this as a realistic model which is not yet apparently ruled out by current data.

The simulations we use in our analyses have $512^3$ particles in a cubic box of size $L_{\mathrm{box}} = 64 h^{-1} \mathrm{Mpc}$, with a background cosmology chosen to be that of the best-fit WMAP9. This cosmology is more updated and more realistic than those of the previous $f(R)$ simulations conducted by us (e.g., Li et al., 2013), and the resolution here is also significantly higher, making it possible to study subhaloes in detail. Our halo catalogue is constructed using a standard friend-of-friend linking method, and

the subhaloes were found using the HBT algorithm of Han et al. (2012b).

Due to the efficient chameleon screening, this $f(R)$ model shows small deviations from $\Lambda$CDM in general. For example, the halo mass function shows at most $\sim 20\%$ enhancement compared with the $\Lambda$CDM result between $z = 0$ and $z = 1$, with the deviation propagating to more massive haloes as time passes, in agreement with the semi-analytical predictions of Li & Efstathiou (2012). The dark matter distribution inside halos is almost identical in this $f(R)$ model as in $\Lambda$CDM for haloes more massive than $\sim 10^{13} h^{-1} M_\odot$, again due to the chameleon screening; however, for smaller haloes, the screening is less efficient, which results in a deepening of the total potential and subsequently a steepening of the density profile. As a result, the halo concentration-mass relation is enhanced for such low-mass haloes and can no longer be described by a simple power law (as for $\Lambda$CDM). The stronger gravitational force in this $f(R)$ model also enhances the growth of small haloes, but mainly at late times and as a result the halo formation time (i.e., the time by which a halo has gained half of its present-day mass) is actually later than in $\Lambda$CDM. We stress that these conclusions hold only for this specific $f(R)$ model, and there is evidence suggesting that other models could behave qualitatively differently because of the complicated behaviour of gravity. We also notice enhanced halo velocity profiles in this $f(R)$ model, confirming various previous work (e.g., Corbett Moran et al., 2015; Gronke et al., 2015; He et al., 2015).

The stronger gravity also helps to produce more substructures, mainly in host haloes less massive than $\sim 10^{13} h^{-1} M_\odot$ because of the weaker screening therein, and for subhaloes less massive than $10^{12} h^{-1} M_\odot$. We find that Milky Way-sized haloes could host up to $20 \sim 50\%$ more subhaloes in the mass range $10^{10} \sim 10^{11}\ h^{-1} M_\odot$ in the studied $f(R)$ model than in $\Lambda$CDM. The subhalo mass function can be fitted using a simple power law, as in $\Lambda$CDM, but with different parameters. We do not find a noticeable difference in the radial distribution of subhaloes inside their host haloes between the two models, though. The higher abundance of substructures is confirmed in the subhalo velocity functions, which seems to make the missing satellite problem of the Milky Way worse. However, we stress that there are caveats in interpreting the result at its face, due to the further complexities in observationally

determining halo mass in the context of modified gravity.

Overall, we find that halo and subhalo properties of this borderline $f(R)$ model are close to the $\Lambda$CDM predictions for massive haloes, confirming previous results that this model is difficult to distinguish from $\Lambda$CDM using cosmological observations. However, a substantial deviation might be found in less massive haloes such as that of our Milky Way, which is in agreement with the findings of previous low resolution simulations. This indicates that the dynamics of systems such as the Local Group can be sensitive to modifications of gravity of this kind and strength. This should be a focus of further studies in the future, following the recent progress in zoom simulations made by Corbett Moran et al. (2015).

As mentioned above, this is a first step of a more detailed study of this borderline model, and here we have not touched the topic of astrophysical constraints, which is much more complicated. Studies of Jain et al. (2013) and Vikram et al. (2014) have demonstrated the potential of using astrophysical systems to improve the constraints on $f_{R0}$. It would be useful to have a better understanding of the impact that environmental screening could have on those constraints. As in $f(R)$ models the local behaviour of gravity usually depends on its environment at much larger scales, high-resolution or zoom simulations are important for calibrating the interpretation of astrophysical observations. They are also important because they can provide more realistic quantifications of the environments for stellar evolution, which depends on the nature of gravitation sensitively (Davis et al., 2012).

Obviously, improved constraints may or may not rule out this $f(R)$ gravity model. However, with the progress in both numerical simulations and theoretical modelling, we are on a path towards better understanding. In such a sense, we are currently in the state of LIMINALITY[1], and much effort is still in need to pass it.

---

[1]In the literature of Education, LIMINALITY refers to the suspended state of partial understanding, which is unsettling and lacks of authenticity. Such a state can be crossed and re-crossed many times, and its final crossing marks the opening of a world of new knowledge.

# Chapter 4

# Halo environment and screening in $f(R)$ gravity

## 4.1 Introduction

One class of models used to explain the mysterious accelerating cosmic expansion, without invoking the addition of an exotic dark energy component (Copeland et al., 2006), assume that the standard model of gravity, general relativity (GR), breaks down on cosmological scales and needs to be modified. Such 'modified gravity' theories (Clifton et al., 2012; Joyce et al., 2015) have generated considerable interest in the cosmological community in recent years. Even though so far there has been no widely-accepted alternative to the standard GR+$\Lambda$CDM model, in which the cosmic acceleration is driven by a positive cosmological constant, the study of possible alternatives could shed light on a question to which an answer is long over-due: does GR hold on cosmological scales (Koyama, 2016; Joyce et al., 2016)? With a number of large cosmological surveys having finished, on going, kicking off and being planned (e.g., Heymans et al., 2012; Anderson et al., 2014; Abbott et al., 2016b; Laureijs et al., 2011; Levi et al., 2013; Merloni et al., 2012; LSST Dark Energy Science Collaboration, 2012), it is optimistic that we will soon enter a new era of research in this field.

Usually, it is assumed that a single gravitational equation governs the behaviour of gravity in the whole classical regime, which covers a huge range from the smallest

scales where gravity has ever been tested (sub-millimetre) to scales comparable to the observable Universe. Therefore, any model of gravity can be tested on various scales and must pass all these tests in order to be viable. Given that GR has been well-established in the Solar system or other systems of relatively small size, such as binary pulsars (Taylor & Weisberg, 1982) and black holes (Abbott et al., 2016a), the behaviour of modified gravity models is expect to make the transition from being GR-like on small scales to predicting a cosmic acceleration on large scales. One way to achieve this, which has been the topic of intensive study in recent years, is via a screening mechanism, which suggests an environmental dependence of gravity: in environments similar to the solar system GR is recovered, while allowing the scope for deviations in environments beyond the reach of current gravity experiments. In such models, two atoms would feel different gravitational forces due to one another depending on whether they are on Earth or in a low-density region.

The presence of a screening mechanism, in certain classes of modified gravity theories, not only leads to theoretical difficulties, such as highly nonlinear gravitational field equations which render linear perturbation analyses more or less useless, but also has very practical implications for the testing of such models. Using the example above, the mutual gravity of the two atoms depends on their location. In other words, it is possible that the accurate prediction of the behaviour of gravity on the smallest scales (e.g., in lab experiments) depends on the actual status (and knowledge) of the much larger-scale environment, such as the hosting galaxy or whether or not the galaxy is in a group or cluster.

Although the term 'environment' has been used extensively in the literature, its precise meaning varies substantially both in theory and in practice. First of all, when we stated above that screening happens in dense environments *similar* to that of the Solar System, the *similarity* can be in terms of local matter density (as in the case of the symmetron model, Hinterbichler & Khoury, 2010), the local Newtonian potential (as in the chameleon model, Khoury & Weltman, 2004; Mota & Shaw, 2007), or derivatives of the potential (as in the cases of the Galileon (Dvali et al., 2000; Nicolis et al., 2009; Deffayet et al., 2009) and K-mouflage (Brax & Valageas, 2014b,a) models).

On top of that, in reality, environment is often defined in terms of what one has from simulations or observations. For example, in a simulation with particle data, it is natural to define the environment of a halo as the average matter density in a spherical region of a given size around the halo, but this will be difficult to reproduce in observations, where instead one can quantify the environment by looking at how many galaxies are neighbouring a given galaxy (having more neighbours is usually an indication that a galaxy is in a high-density environment). Alternatively, using weak lensing one can construct maps of gravitational potential, by which the environment can also be quantified. Although the different measurements of environment rely on different physical quantities – density, potential or derivatives of the potential – and are therefore presumably suitable for testing the different theoretical screening mechanisms as mentioned above, as we shall see, there is a good correlation among them (e.g., a high-density region often has deeper gravitational potential and larger derivatives of the potential). This, together with the fact that there are only a limited number of ways to measure environment in observations, suggests that pragmatically all definitions of environment should be tried to see how best to understand the screening of modified gravity.

In addition, for objects with extensive sizes, such as those encountered in cosmology, depending on what we look at, the objects themselves can be part of the environment. For example, if we consider a massive galaxy cluster which hosts a galaxy, then the cluster itself (excluding the galaxy) serves as part of the environment of the galaxy, along with the larger-scale environment that in which cluster is embedded. It can sometimes be useful to distinguish between the self-screening and environmental screening of the cluster, with the former defined as the screening of modified gravity caused by the cluster assuming that it is embedded in a vacuum. In practice, definitions of environment do not always separate the two effects cleanly, as we shall see below.

The effect of environmental screening in modified gravity was investigated previously for the chameleon (Zhao et al., 2011b) and symmetron (Winther et al., 2012) models, but these studies used one particular definition of environment, and were based on relatively low-resolution $N$-body simulations. It is our purpose to further

these studies in two ways: (i) We will try other definitions of environment in addition to the one adopted in Zhao et al. (2011b) and Winther et al. (2012), to study how robust the qualitative conclusions of these studies are to the various definitions. In particular, this will tell us whether the different ways to measure environment observationally can corroborate or complement each other; (ii) Our study here is based on a higher-resolution simulation, which will enable us to resolve smaller dark matter haloes to study the screening in different parts (e.g., inner vs outer) of a halo, and to investigate the screening of subhaloes as well. The study of these low-mass objects will be useful for accurately understanding how gravity behaves in such systems, which have been suggested to provide the strongest astrophysical constraints on potential deviations from GR (e.g., Jain et al., 2013). The screening of modified gravity from these low mass halo also depends more sensitively and complicatedly on their environments.

The model studied here is a variant of $f(R)$ gravity (Carroll et al., 2004, 2005) as proposed by Hu & Sawicki (2007). With suitable model parameters, this model is a special case of the chameleon-type theory studied by Zhao et al. (2011b) and many other authors. Despite being a special case with a rather ad-hoc form of the gravitational action, the model is quite representative in the sense that similar qualitative behaviours can be found in other variants of viable $f(R)$ models, or more generally chameleon models (see, e.g., Brax et al., 2012a, 2013), or even symmetron or dilaton (Brax et al., 2010, 2012b) models. Therefore, it can be used as a test case to estimate constraints on certain classes of deviations from GR.

The layout of this chapter is as follows: in §4.2 we briefly describe the model, the simulation and the way used to find haloes/subhaloes; in §4.3 we briefly introduce the different definitions of environment to be tested, and have a look at their correlations with each other using the simulation; in §4.4 we show the environmental screening effects using these different environment definitions and in §4.6 we discuss the implications of our results and conclude.

Throughout the chapter we use the convention that a subscript $_0$ (overbar) denotes the current (cosmic mean) value of a quantity. We use the unit $c = 1$ ($c$ is the speed of light) unless otherwise stated.

## 4.2 Simulations of $f(R)$ gravity

$f(R)$ gravity is the most well-studied modified gravity theory in the context of understanding the origin of the cosmic acceleration, and there is a large body of literature on various aspects of this model. In order to avoid unnecessary repetition, we shall restrain from devoting space to yet another introduction to it. Interested readers are referred to the review articles (e.g., De Felice & Tsujikawa, 2010; Sotiriou & Faraoni, 2010) for full details, or to one of the research papers for shorter but still self-contained descriptions, e.g. Shi et al. (2015), which not only concisely describes the essential ingredients of $f(R)$ gravity sufficient for understanding this chapter, but also introduces the LIMINALITY simulation which this work is based on.

The LIMINALITY simulation is a dark matter only $N$-body simulation of a certain variant of the Hu-Sawicki $f(R)$ gravity model (Hu & Sawicki, 2007). It was run using the ECOSMOG code (Li et al., 2012), which itself is based on the publicly available $N$-body code RAMSES (Teyssier, 2002), but includes new modules and subroutines to solve the modified Einstein equations in $f(R)$ gravity. This is an effectively parallelised adaptive mesh refinement (AMR) code, which starts with a uniform grid (the domain grid) covering the cubic simulation box with $N_{\mathrm{dc}}^{1/3}$ cells on a side. If the effective particle number in a grid cell becomes greater than a pre-defined criterion ($N_{\mathrm{ref}}$), the cell is split into eight "son" cells, and in this way the code hierarchically achieves ever higher resolution in dense environments. Such high resolution is necessary to accurately trace the motion of particles and guarantee the accuracy of the fifth force solutions. The force resolution, denoted by $\epsilon_{\mathrm{f}}$, is taken as twice the size of the cell where a particle is physically located, and we quote $\epsilon_{\mathrm{f}}$ on the highest refinement level. The simulation and model parameters are summarised in Table 3.1.

In $f(R)$ models, the strength of gravity is enhanced compared to GR, and the size of the enhancement depends on the local gravitational potential (e.g., Khoury & Weltman, 2004), ranging from 0 inside deep potential wells (where screening takes place) to a maximum of enhancement $1/3$ in regions with shallow potential. The maximally $1/3$ enhancement of gravity is a generic property of the models,

regardless of the technical details (e.g., whether it is Hu-Sawicki or some other variant), the latter only affecting the transition between 0 and 1/3 (e.g., whether at a given spacetime position the modification to GR is screened or not). Following the convention used in the literature, we call the difference between the modified and standard GR gravitational forces the *fifth force*. If screening happens, the fifth force vanishes, and in unscreened regions it is an attractive force 1/3 the strength of standard Newtonian gravity, giving a total force of 4/3 the GR force.

The Hu-Sawicki $f(R)$ model studied is a particular case specified by a parameter $f_{R0} \equiv \left[ \mathrm{d}f(\bar{R})/\mathrm{d}\bar{R} \right]_0 = -10^{-6}$. This case is of particular interest here, since the deviations from GR it predicts on cosmological scales are still allowed by current observations (see, e.g., Cataneo et al., 2015; Liu et al., 2016, for some of the latest cosmological constraints on $|f_{R0}|$; note that a smaller $|f_{R0}|$ indicates a weak deviation from GR); while stronger constraints are suggested from smaller scales, a precise quantification of the constraints requires a good knowledge about whether (and how well) dark matter haloes and subhaloes are screened (Jain et al., 2013). In the literature, this model is often called F6; throughout the chapter, when we talk about $f(R)$ model, we mean F6 unless clearly otherwise stated. With $512^3$ particles in a box of size $L_{\mathrm{box}} = 64 \ h^{-1}\mathrm{Mpc}$, the LIMINALITY simulation is currently the highest resolution cosmological simulation of $f(R)$ gravity that runs from $z = 49$ until $z = 0$, with full information of the fifth force recorded. As a result, it is ideal for the analysis of the screening of dark matter haloes and their substructures (which would be poorly resolved should the resolution be too low).

The dark matter halo catalogue used in our analyses was obtained using the friends-of-friends (FoF) group-finding algorithm, with a linking length of 0.2 times the mean inter-particle separation (Davis et al., 1985). We used the tracking subhalo finder Hierarchical Bound-Tracing (Han et al., 2012b, HBT) to identify subhaloes. HBT works in the following way: (i) starting from isolated haloes at a previous snapshot, it finds their descendants in subsequent snapshots and keeps track of their evolution; (ii) when two haloes merge, it tracks the self-bound part of the less massive progenitor as a subhalo in subsequent snapshots. In this way, all the subhaloes formed from halo mergers can be identified with a single walk through all

Table 4.1: The different definitions of environment used in this chapter. See the main text for more details (§4.3).

| name | symbol | parameter(s) | equation |
|---|---|---|---|
| conditional nearest neighbour | $D_{N,f}$ | $f = 1$, $N = 1, 10$ | Eq. (4.3.1) |
| spherical overdensity | $\delta_R$ | $R = 5, 8 h^{-1} \mathrm{Mpc}$ | Eq. (4.3.2) |
| shell overdensity | $\delta_{R,R_{\min}}$ | $R_{\min} = R_{\mathrm{halo}}$ | Eq. (4.3.3) |
| experienced gravity | $\Phi_\star$ | None | Eq. (4.3.8) |
| total gravity | $\Phi_+$ | None | Eq. (4.3.8) |

the snapshots. This algorithm enables HBT to largely avoid the resolution problem encountered by configuration-space subhalo finders.

## 4.3   Environment definitions

As directly measuring the distribution of mass is not always possible, observers usually use the distribution of galaxies to estimate the density around galaxies. There are quite a few different methods to estimate the environmental dependence of galaxy properties. Table 1 in Haas et al. (2012) briefly summarised the environmental measures used in the literature. In simulations, using similar environmental measure makes it convenient to compare with observational results. On the other hand, the density field can be directly measured using simulation particles. These quantities are in principle more accurate than indirect environmental measures.

In this section, we briefly introduce the different definitions of environment we use.

### 4.3.1   Conditional nearest neighbour

Galaxies that live in denser environments preferentially have closer neighbours. Following this principle, the conditional nearest neighbour environment measure of a halo with mass $M_L$ is defined as the distance $d$ to its $N$th nearest neighbour halo whose mass is at least $f$ times as large as $M_L$ (Haas et al., 2012). This quantity is rescaled by the virialized radius $r_{NB}$ of the neighbouring halo to define $D_{N,f}$ as

$$D_{N,f} = \frac{d_{N,M_{NB}/M_L \geq f}}{r_{NB}}. \tag{4.3.1}$$

A halo with large value of $D_{N,f}$ indicates a paucity of nearby halos, implying that the halo lives in a low-density environment.

In the context of modified gravity, this environment definition was previously used in Zhao et al. (2011b) and Winther et al. (2012). It has the added freedom of varying the values of $N$ and $f$ to allow continuous quantitative changes in $D_{N,f}$. It is also more directly connected to observations, as we can treat haloes and subhaloes are proxies to clusters and galaxies in the real Universe.

$D_{N,f}$ is also a more faithful definition of environment, because the halo of mass $M_L$ itself is not counted as a neighbour (in other words, $D_{N,f} \neq 0$). However, this definition is not completely independent of $M_L$, as $M_L$ is used in the condition $M_{NB}/M_L \geq f$ (which is why we name it the *conditional* nearest neighbour). This could lead to the unphysical consequence that for very massive haloes, which are likely to live in dense environments, it is more difficult to find neighbours with $M_{NB} \geq fM_L$. Hence $D_{N,f}$ is large, implying that such halos are in low-density environments. We shall bear this in mind when analysing our results.

## 4.3.2   Spherical & shell overdensity

In observations, counting the number of neighbouring galaxies in a fixed volume around a galaxy is another way to measure the environment, as a higher galaxy number density indicates a denser environment. Although galaxies are biased tracers of the underlying matter density field, techniques have been developed to reconstruct the density field from observational distributions of galaxies (e.g., Kitaura et al., 2010; Platen et al., 2011; Ata et al., 2017).

Given our purely theoretical interest, we measure the dark matter density in a spherical volume around a halo, which we define as the spherical overdensity environment. This is expressed as

$$1 + \delta_R \equiv \frac{\rho(\leq R)}{\bar{\rho}} = \frac{N(\leq R)}{\bar{N}}, \tag{4.3.2}$$

where the $R$ is the radius (in units of $h^{-1}\mathrm{Mpc}$) of the spherical volume, $N$ is the number of particles found in this volume and $\bar{N}$ is the mean number of dark matter

particles in a volume of size $4\pi R^3/3$.

By definition, the spherical overdensity environment measure $\delta_R$ includes the contribution from the halo at the centre of the spherical volume. One can define similarly a 'shell overdensity' environment as

$$1 + \delta_{R,R_{\min}} \equiv \frac{\rho(R_{\min} \leq r \leq R)}{\bar{\rho}} = \frac{N(R_{\min} \leq r \leq R)}{\bar{N}}, \qquad (4.3.3)$$

where we exclude the particles within a minimum radius $R_{\min}$ given by $R_{\text{halo}} \leq R_{\min} < R$, with $R_{\text{halo}}$ being the radius of the central halo.

### 4.3.3 Experienced gravity

While the dark matter density as used in defining $\delta_R$ and $\delta_{R,R_{\min}}$ is not directly measurable, its effects can be observed in various ways, such as gravitational lensing and galactic dynamics, that probe the lensing and dynamical potential respectively. Even though the two potentials may not coincide with each other in theories of modified gravity, they both serve as a good characterisation of environment. Indeed, lensing and galaxy dynamics are governed respectively by the potential and its derivative, so using these to define the environment may be particularly useful for models in which the screening depends on these quantities.

In our simulation, the potentials of the Newtonian gravity and the total gravitational force in $f(R)$ gravity on every simulation particle are output separately. Here, we use only the Newtonian potential as an environment measure, since in the $f(R)$ model studied the lensing potential (which can be reconstructed from lensing observations) satisfies the standard Poisson equation as the Newtonian potential in GR subject to corrections which are negligible in practice.

The Newtonian potential at any given position inside a dark matter halo receives contributions from both self gravity (i.e., the potential due to the halo itself) and environment (i.e., that caused by material outside the halo). The self-gravity contribution can be calculated analytically given that haloes satisfy the usual Navarro-Frenk-White (Navarro et al., 1996, 1997, NFW) density profile even in $f(R)$ gravity (Lombriser et al., 2012; Shi et al., 2015). Subtracting this from the total Newtonian

potential at the position, which is given by our simulation, leads to the environment measure which we dub "experienced gravity".

To be explicit, the Newtonian potential of a spherical halo is given as

$$\Phi(r) = \int_0^r \frac{GM(r')}{r'^2} \mathrm{d}r' + C, \tag{4.3.4}$$

in which $GM(r)/r^2$ is the gravitational force at distance $r$ from the centre of the halo, and $C$ is an integration constant that can be fixed using $\Phi(r \to \infty) = \Phi_\infty$, the Newtonian potential infinitely far away from the halo.

The NFW density profile of a spherical halo is given by

$$\frac{\rho(r)}{\rho_c} = \frac{\beta}{\frac{r}{R_s}\left(1 + \frac{r}{R_s}\right)^2}, \tag{4.3.5}$$

where $\rho_c$ is the critical density for matter, $\beta$ and $R_s$ are two fitting parameters. Plugging this into Eq. (4.3.4), it can be derived that

$$\int_0^r \frac{GM(r')}{r'^2} \mathrm{d}r' = 4\pi G\beta\rho_c R_s^3 \left[\frac{1}{R_s} - \frac{\ln\left(1 + \frac{r}{R_s}\right)}{r}\right], \tag{4.3.6}$$

and so

$$C = \Phi_\infty - 4\pi G\beta\rho_c R_s^2. \tag{4.3.7}$$

Here, if halo is isolated, then $\Phi_\infty = 0$. But in $N$-body simulations or the real Universe, no halo is totally isolated from the others. So $\Phi_\infty$ does not always go to zero. Therefore, we replace $\Phi_\infty$ by $\Phi_\star$, which is the potential produced by all the other haloes at the position of a given halo. The Newtonian potential in the halo can then be written as

$$\Phi(r) = \Phi_\star - 4\pi G\beta\rho_c \frac{R_s^3}{r} \ln\left(1 + \frac{r}{R_s}\right), \tag{4.3.8}$$

in which $\Phi_\star$ is our definition of the experienced gravity environment measure, and $\Phi(r)$ is directly measured from our simulation. The second term on the right-hand side of Eq. (4.3.8) is the self-gravity contribution which is calculated from the NFW

fitting parameters (i.e, $\beta$, $R_s$) of every individual dark matter halo, cf. Eq. (4.3.5). This way to compute $\Phi_\star$ was previously used in, e.g., Li et al. (2011).

Assuming that the size of a given halo is much smaller than the Universe or the simulation box, we would expect the environment measure $\Phi_\star$ to stay roughly constant inside a halo. In Eq. (4.3.8), both $\Phi(r)$ and the self-gravity term on the right-hand side take different values at different $r$ ($r \leq R_{\text{halo}}$), which means that there is no *a priori* guarantee that $\Phi_\star$ is the same everywhere at $r \leq R_{\text{halo}}$. In Appendix A, we perform a check of the constancy of $\Phi_\star$ and show that the $\Phi_\star$ environment measure works quite well.

Finally, we note that $\Phi_\star$, although a good measurement of the environment of a dark matter halo, is not what gravitational lensing reconstructions give us as the latter do not distinguish between self and environmental contributions. For this reason we define another measure, called total gravity, or $\Phi_+$, which is the average of $\Phi(r)$, cf. Eq. (4.3.8), inside the halo ($r \leq R_{\text{halo}}$). Neither $\Phi_\star$ nor $\Phi_+$ have free parameters, unlike $D_{N,f}$, $\delta_R$ and $\delta_{R,R_{\text{min}}}$.

Table 4.1 summarises our environment measures. Before looking at how the screening depends on environment, in Fig. 4.1 we first have a look at the correlation between the different environment measures themselves. Note that a strong correlation is present between the spherical overdensity ($\delta$) and experienced gravity ($\Phi$) definitions, which is as expected given the relationship between the gravitational potential and local matter density. $D_{1,1}$, on the other hand, correlates much less tightly with the other measures, because of the complexities in inferring matter density from the galaxy number density (or in our case, the halo density). $D_{10,1}$, in contrast, seems to correlate more tightly with the other measures, due to two reasons:

(1) $D_{10,1}$ encompasses more (10 rather than 1) massive haloes, and so for the same value it characterises a denser environment than $D_{1,1}$; it is also less affected by outliers such as haloes residing in a low-density environment but which happen to have a neighbour nearby.

(2) For the same reason above, $D_{10,1}$ takes on a different range of values than $D_{1,1}$. Because $D_{10,1}$ is shown using a logarithmic scale in Fig. 4.1, the variation is
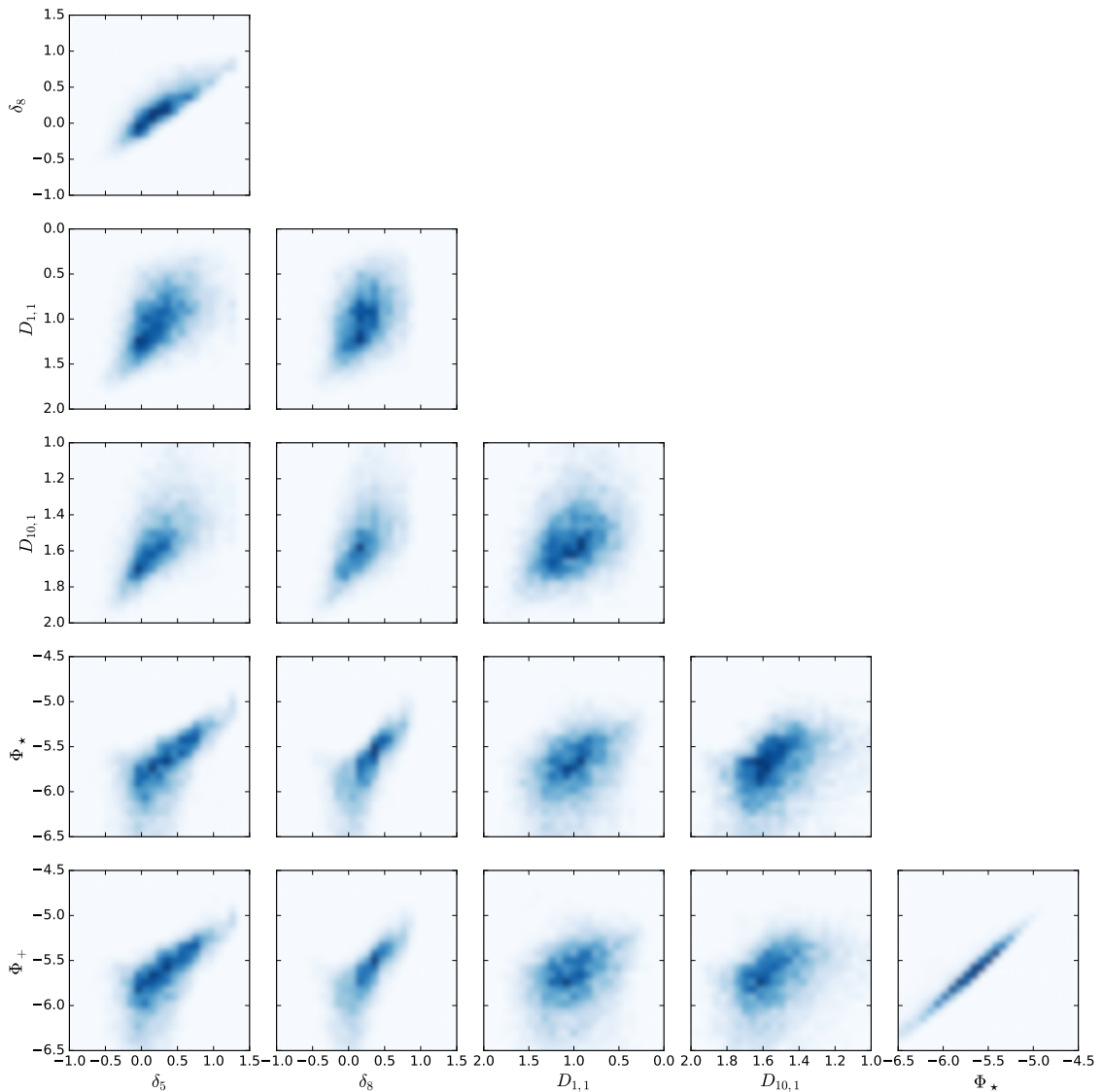
Figure 4.1: The correlations between the different environment measures defined in §4.3. The different panels compare different pairs of environment definitions, whose values are shown on the two axes of the panel. The number density of haloes in a given environment is colour coded, with darker (lighter) blue meaning more (fewer) haloes having that environment. The results are obtained using the ΛCDM version of the LIMINALITY simulation. Note that due to space limitations not all environments used in the latter part of this chapter are compared here.

actually larger on the range of $1.5 < \log D_{10,1} < 2$ than that for $0.5 < \log D_{1,1} < 1.5$. This makes $D_{10,1}$ appear to be more strongly correlated with the other measures visually.

Overall, the conclusion is that the different environment measures tested here do correlate reasonably well with one another.

## 4.4 Environment measures and screening

We use $M_{200}$ as halo mass, which is the mass inside the radius $r_{200}$ within which the average density is 200 times the critical density, $\rho_c$. In our analysis, dark matter haloes are binned into four mass ranges as $1 \sim 3 \times 10^{11} \mathrm{M}_\odot/h$, $3 \times 10^{11} \sim 1 \times 10^{12} \mathrm{M}_\odot/h$, $1 \times 10^{12} \sim 1 \times 10^{13} \mathrm{M}_\odot/h$ and $1 \times 10^{13} \sim 1 \times 10^{14} \mathrm{M}_\odot/h$. Note that the $10^{11} \sim 10^{12} \mathrm{M}_\odot/h$ haloes are divided into two smaller bins. As the effects of modified gravity are efficiently screened in massive haloes, the main difference between F6 and GR is in these low-mass halos.

Here, we study how the modified gravitational force and potential behave in different environments, for the environment measures introduced above. To this end, we define the *fifth-force-to-gravity ratio* (or *fifth force ratio* in short) as the ratio between the magnitude of the fifth force in $f(R)$ gravity (see §4.2) and that of the standard Newtonian force. This quantity approaches 0 in screened regions and 1/3 in unscreened regions, but can take any value in between (the transition region). We will also use the *fifth force potential* which is expressed in units of $2\Phi_N/3$, where $\Phi_N$ is the potential for the standard Newtonian gravity (Zhao et al., 2011a). Note that the fifth force potential is dimensionless, going to 0 in screened regions and 1/2 in unscreened regions.

Our simulation outputs the fifth force and potential at the positions of all simulation particles. We measure the fifth force ratio and fifth force potential in two ways: the average over the values at the positions of all particles inside $R_{\mathrm{halo}} = R_{200}$, and the value at halo centres, the latter being obtained by averaging all the particles within $r \leq 0.2R_{200}$ given the uncertainty in defining the halo centre, and call these $R_{c200}$ and 'halo centre' respectively. The second case is relevant for the screening of
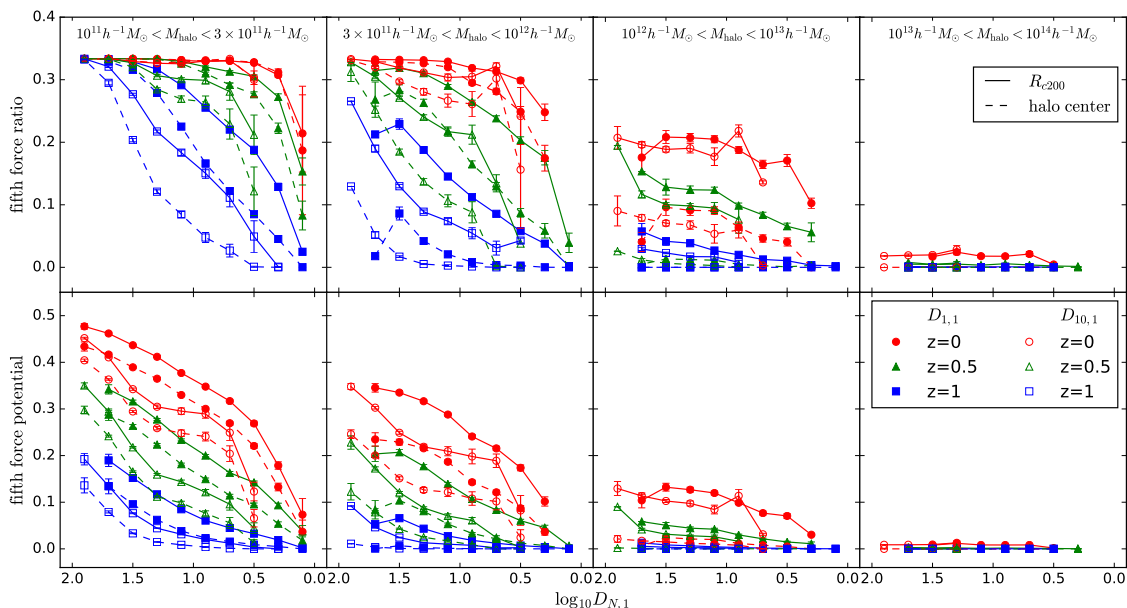
Figure 4.2: The fifth force ratio (top panels) and fifth force potential (bottom panels) as a function of the conditional nearest neighbour halo environment $D_{1,1}$ (filled symbols) and $D_{10,1}$ (open symbols) at $z = 0$ (red), 0.5 (green) and 1 (blue). The halo samples are divided in to four mass bins as indicated on the top of each panel. The solid lines show the results measured from all particles within $r_{200}$, and the dashed lines are measured from the halo centres only (see the text for more details).

the fifth force inside central galaxies which are at the centres of their host haloes, while the first case can be used for satellite galaxies.

## 4.4.1 Conditional nearest neighbour

In GR, $D_{1,1}$ is known to represent the local dark matter density well and to be almost uncorrelated with the mass of the halo. In $f(R)$ gravity, Zhao et al. (2011b) confirmed that the mass independence of $D_{1,1}$ still holds. We adopt both $D_{1,1}$ and $D_{10,1}$, which are derived from the first and tenth nearest neighbours heavier than the halo, respectively, as the conditional nearest neighbour environment definitions.

Fig 4.2 shows the fifth force ratio (upper panels) and the fifth force potential (lower panels) against these two conditional nearest neighbour halo environmental measures, in the four halo mass bins (as indicated on the top of the different panels) at $z = 0$ (red circles), 0.7 (green triangles) and 1(blue squares). At all three redshifts and in all four mass bins, there is a noticeable trend that the fifth force ratio and potential both increase with $D$. As larger values of $D$ correspond to lower-density

environments, this agrees with the naive theoretical prediction that the haloes living in low-density regions are more likely to be unscreened. Also, we can see clearly that the most massive halos have negligible fifth force potentials, because of the efficient screening in these objects. The increase of fifth force ratio from 0 to 1/3 represents the transition from unscreened to screened haloes. At the same redshift, the transition occurs at smaller $D$ for lower-mass haloes. Inside the same halo mass bin, the screening is stronger at higher redshifts, because the Universe is denser at early times.

The halo centre (dashed curve) always has a smaller fifth force ratio and potential than the average in the whole halo (solid curve). This is as expected, as the NFW profile has higher density in the inner region of a halo than at its outskirts, which means that screening is stronger in the inner part. The difference between halo centre and $R_{c200}$ is particularly strong for the halo mass bin $10^{12} \sim 10^{13} \mathrm{M_\odot}/h$ at $z < 0.5$, which is also true for less massive haloes at higher redshifts ($0.5 < z < 1$; blue and green curves in the two left columns). This is again because at a given redshift the fifth force inside haloes with a certain mass goes through a transition from screened to unscreened, and these haloes can be in a state such that their inner parts are well screened while the outer regions remain unscreened. This transition starts from smaller haloes first, and progressively affects more massive haloes at later times. This observation is relevant if one is interested in the screening of central galaxies in haloes.

As the tenth nearest larger neighbouring halo of a given halo is always farther away than the nearest larger neighbour, and yet is not necessarily larger in size, for a given halo we have $D_{1,1} < D_{10,1}$. Conversely, $D_{1,1}$ represents a less dense environment than the same value of $D_{10,1}$ does. In Fig. 4.2, the fifth force ratio curves corresponding to the $D_{10,1}$ environment measure (open symbols) are always below those for $D_{1,1}$ (filled symbols), confirming that screening is stronger for denser environments. Note that the $D_{10,1}$ curves shift to larger values along the $x$-axis compared to the $D_{1,1}$ curves.
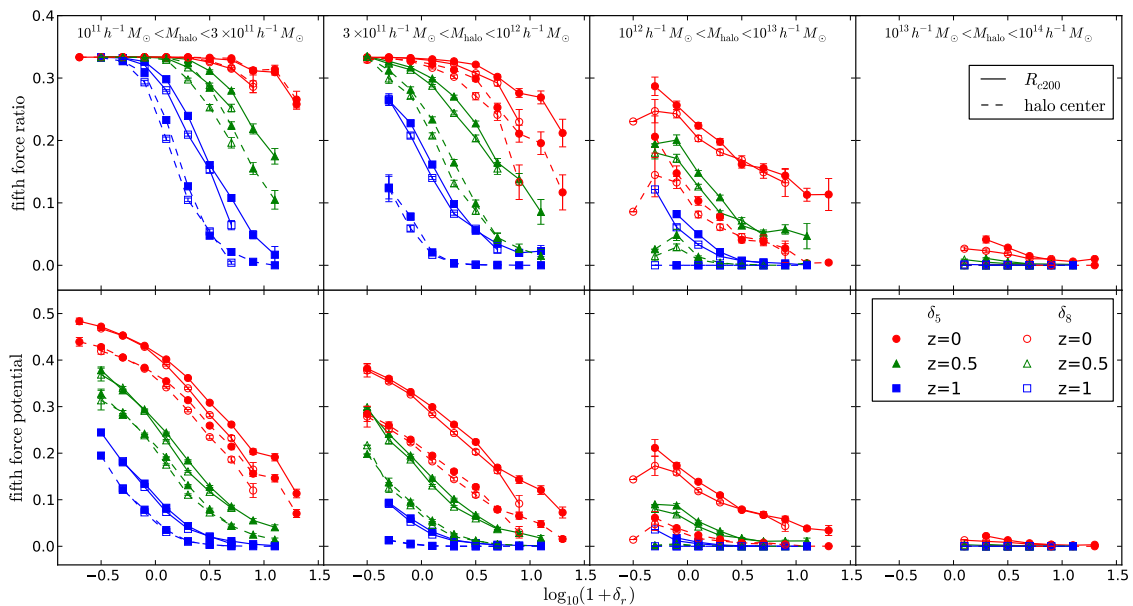
Figure 4.3: The fifth force ratio (top panels) and fifth force potential (bottom panels) as a function of the spherical overdensity halo environment $\delta_5$ (filled symbols) and $\delta_8$ (open symbols) at $z = 0$ (red), 0.5 (green) and 1 (blue). The halo samples are divided in to four mass bins as indicated on the top of each panel. The solid lines show the results measured from all particles within $R_{200}$, and the dashed lines are measured from the halo centres only (see the text for more details).

## 4.4.2 Spherical overdensity

We use spherical volumes with radii of $5h^{-1}\mathrm{Mpc}$ and $8h^{-1}\mathrm{Mpc}$ around the dark matter halo centre to measure the density contrast, devoted $\delta_5$ and $\delta_8$. These values are used in Li et al. (2012) to ensure the spherical volumes are neither too large (otherwise they will not be a faithful representation of the local environment) nor too small (otherwise the definition of environment will be too noisy and sensitive to the presence of the central halo in the spherical volume). Physically, these numbers are up to a few times the Compton wavelength of the scalar field for the redshift range we are interested in, and the region enclosed is most relevant to the dynamical state of the scalar field[1].

Fig. 4.3 plots the spherical overdensity measures against the fifth force ratio and

---

[1]Although, if the region is too small, e.g., smaller than the scalar field's Compton wavelength, then the scalar field will be affected by matter outside, making the environment definition insufficient. Similarly, if the spherical region is too large, it may contain matter which does not have a significant impact on the scalar field in the central halo, again making the definition less relevant.

potential, which has the same format as Fig. 4.2. We can see clearly the similar overall trend that the fifth force ratio and potential decrease with $\delta_R$. Here, a larger value of $\delta_R$ means higher density region, which in turn means the fifth force is more likely to be screened, again, as expected.

For the same value of $\delta_5$ and $\delta_8$, $\delta_8$ represents an environment with higher matter density because it manages to have the same $\delta$ in a bigger volume even though matter over-density is generally expected to be lower at larger radii from the centre. Correspondingly, Fig. 4.3 shows that the screening is stronger for $\delta_8$. However, the difference is small, because even $5h^{-1}\mathrm{Mpc}$ is already significantly bigger than the halo radius.

Comparing Fig. 4.3 to Fig. 4.2, it can be seen that these two plots are qualitatively similar to each other. This serves as a cross check that both environment definitions can be applied to infer the screening of galaxies for an observed galaxy catalogue. We also checked the results by using the shell overdensity definition, $\delta_{R,R_{\min}}$, where $R_{\min} = R_{\mathrm{halo}} = R_{200}$ and $R = 5h^{-1}\mathrm{Mpc}, 8h^{-1}\mathrm{Mpc}$, and found only tiny differences from Fig. 4.3; so we will not show them here.

### 4.4.3 Experienced and total gravity

Finally, we consider the experienced and total gravity measures of halo environment, which are defined using the Newtonian potential produced at the position of a halo by matter outside the halo and by all matter (including that from the halo itself) respectively.

In order to fit the NFW profile, we divide the halo radius, $R_{200}$, into twenty bins equally spaced in logarithmic scale (see Shi et al. (2015) for more details), and then measure the mass density of every spherical shell. $\Phi_\star$ is then calculated using Eq. (4.3.8) and the NFW parameters resulting from the fit, in which $\Phi(r)$ is read from the simulation output and spherically averaged for every shell. The $\Phi_\star$ calculated in this way has small fluctuations across different shells, mostly due to numerical noise, but in Appendix A we can see that the fluctuations are insignificant. The value of $\Phi_\star$ used is the average over all spherical shells.

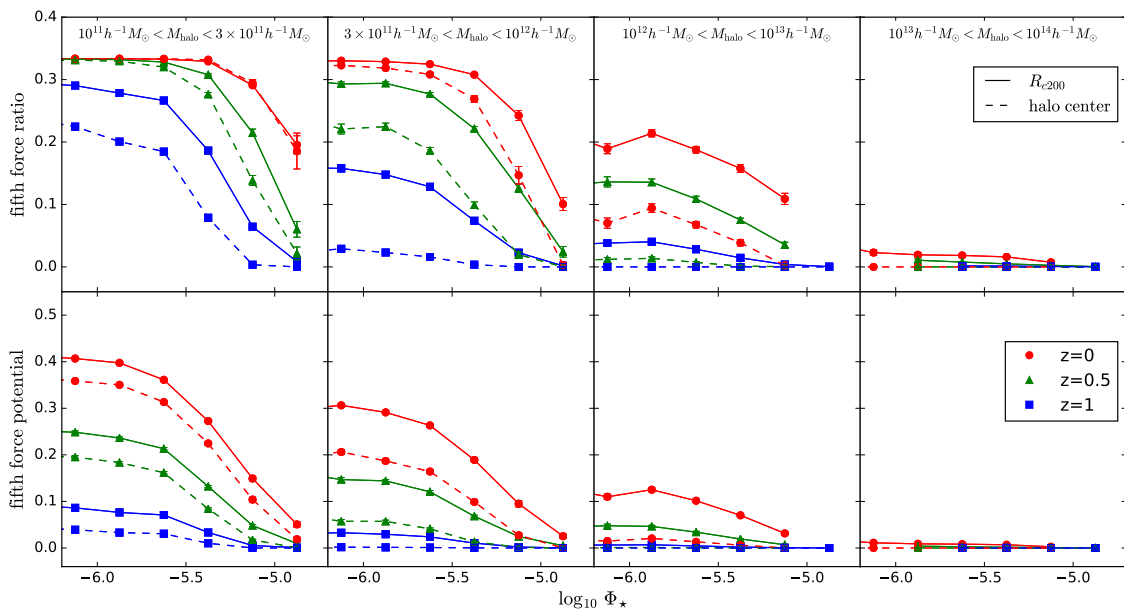Fig. 4.4 shows how the fifth force ratio and fifth force potential depend on $\Phi_\star$ for

Figure 4.4: The fifth force ratio (top panels) and fifth force potential (bottom panels) as a function of the experienced gravity halo environment $\Phi_\star$ (filled symbols) at $z = 0$ (red), 0.5 (green) and 1 (blue). The halo samples are divided into four mass bins as indicated on the top of each panel. The solid lines show the results measured from all particles within $R_{200}$, and the dashed lines are measured from the halo centres only (see the text for more details).

the four mass bins considered. We can see a similar overall trend to that in Figs. 4.2 and 4.3, that more massive haloes living in denser environments (i.e., larger $|\Phi_\star|$) are better screened, but there is also a noticeable difference, namely the curves in Fig. 4.4 are smoother and the scatter smaller. The latter, in particular, implies that this definition of environment is better for the study of the chameleon screening. This is not unexpected, since it is well known that the condition for screening – the thin-shell condition (Khoury & Weltman, 2004) – is explicitly determined by the Newtonian potential that an object feels.

In Fig. 4.5 we present the same result as in Fig. 4.4, but with $\Phi_\star$ replaced by $\Phi_+$. All features discussed in Fig. 4.4 remain, with only slight quantitative changes. In particular, the curves are smooth and the scatter is small. As $\Phi_+$ is the total potential at the position of a dark matter halo, it is what weak lensing (tomography) observations will give us; this is unlike $\Phi_\star$, which is the potential at the position of the halo produced by everything but the halo itself, and thus is a more theoretical definition of 'environment'.
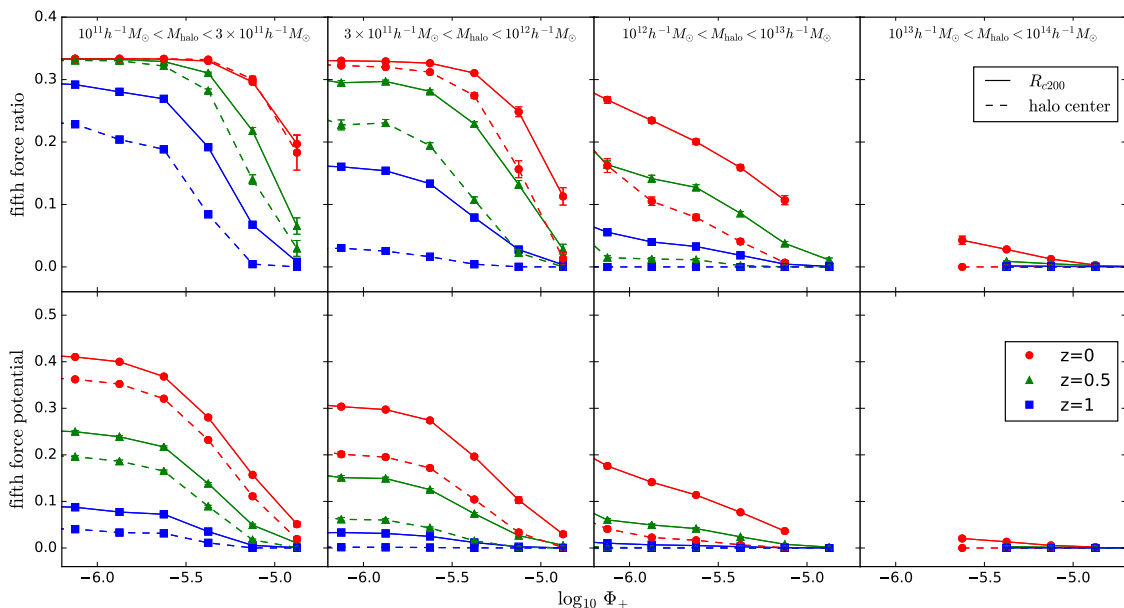
Figure 4.5: The fifth force ratio (top panels) and fifth force potential (bottom panels) as a function of the total gravity potential halo environment $\Phi_+$ (filled symbols) at $z = 0$ (red), 0.5 (green) and 1 (blue). The halo samples are divided into four mass bins as indicated on the top of each panel. The solid lines show the results measured from all particles within $R_{200}$, and the dashed lines are measured from the halo centres only (see the text for more details).

## 4.5 Environmental screening of subhaloes

With the current knowledge of galaxy formation, galaxies mostly form from the cooled gas inside dark matter substructures in haloes. Thus, instead of arbitrary positions inside haloes, we are more interested in the substructures (or subhaloes), where galaxies and stars reside such that tests of gravity are possible, for example, by studying the effect of modified gravity on stellar evolution and properties (Davis et al., 2012; Jain et al., 2013). Since subhaloes represent small density peaks inside a halo, with densities higher than their immediate surroundings, it is reasonable to expect the chameleon screening inside them to be stronger than outside them. Many modified gravity simulations, however, do not have sufficient resolution to resolve subhaloes. As a result, Corbett Moran et al. (2015) propose to approximate the fifth force ratio inside a subhalo, which is at a distance $r$ from the centre of its host halo, to be the average value at all dark matter simulation particles inside a thin shell with radius range $[r - \Delta r/2, r + \Delta r/2]$. The LIMINALITY simulation has high
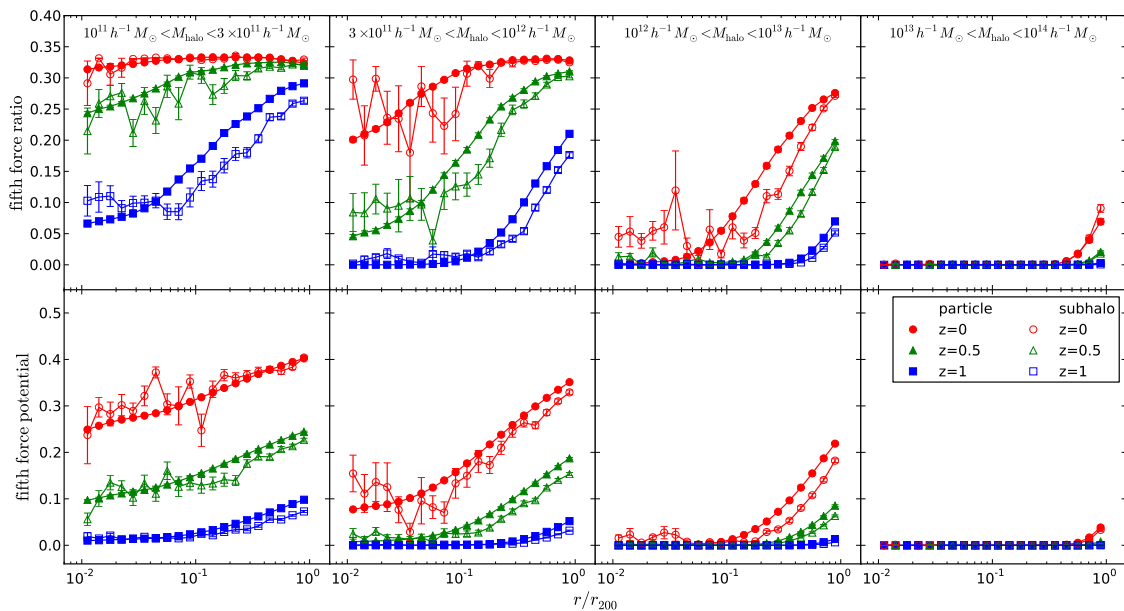
Figure 4.6: The stacked fifth force ratio (upper panels) and fifth force potential (bottom panels) profiles within halo radius $R_{200}$ at $z = 0$ (red circles), 0.5 (green triangles) and 1 (blue squares). In each panel we show the comparison between the quantities measured by all simulation particles (filled symbols) and that measured by subhaloes (open symbols).

enough resolution for us to check the validity of this approximation.

In Fig. 4.6, we show the fifth force ratio and fifth force potential as a function of the radial distance from the halo centre ($r/R_{200}$), for subhaloes (open symbols) and dark matter particles (filled symbols). We can see that inside the most massive haloes (the rightmost column) and the least massive haloes (the leftmost column), the degree of screening is similar for dark matter particles and subhaloes. For the former, both particles and subhaloes are perfectly screened, which is why there is little difference; for the latter, at low redshifts, both particles and subhaloes are unscreened, such that again there is no difference.

For haloes of intermediate masses (the middle columns), however, the screening is consistently stronger in subhaloes where densities are higher than their immediately surroundings, as expected. However, the difference is generally small, because the Newtonian potential inside subhaloes is not dramatically deeper than outside. Although the curves for subhaloes are noisier due to poor statistics, they follow the trend of the curves for dark matter particles, which suggests that the approximation of Corbett Moran et al. (2015) can provide a reasonable conservative estimate of

screening in subhaloes even for lower-resolution simulations where subhaloes may be unresolved.

Fig 4.6 (filled symbols) also helps to visualise the 'screening profile' inside dark matter haloes. We can see how the inner parts of haloes are completely screened for massive haloes, while more and more volume becomes unscreened for smaller haloes and at lower redshifts. In particular, we note that the transition from screened to unscreened regions is quite slow.

## 4.6 Discussion and conclusions

We have investigated the effect of environment on the efficiency of chameleon screening in $f(R)$ gravity. Based on a high-resolution $N$-body simulation (Shi et al., 2015), we have checked the various ways to define the 'environment' of a dark matter halo. The definitions can be roughly put into three categories:

1. counting how many galaxies or, in $N$-body simulations, haloes, a given halo has as neighbours which satisfy certain requirements on their mass and/or distance from the considered halo;

2. estimating the underlying (nonlinear) dark matter density given the halo/galaxy number density;

3. using the Newtonian potential caused by the matter density field at the positions and surroundings of a given halo.

Each of these classes of environment definitions can be further divided depending on the precise physics included and parameters used, and the resulting definitions are given in Table 4.1. In Fig. 4.1 we show the correlations of the different environment measures, where we find overall a good agreement between all of them.

We then study how the screening of the fifth force inside dark matter haloes depends on the environment that these haloes live in. Our analysis reconfirms the well known result that the screening is stronger for more massive haloes which live in dense environments. More importantly, the result also shows a reasonable agreement between the different environment definitions, hence verifying the robustness of the latter. This will have important implications for the construction of 'screening maps'

from observed galaxy catalogues (see, e.g., Jain et al., 2013), which is an essential step for predicting precisely how gravity changes its behaviour inside galaxies, which in turn can be used to constrain any deviations from GR. Since the model we study, F6, deviates only slightly from GR, being able to confidently rule it out will push the boundary of cosmological tests of gravity firmly into a new regime.

These different environment measures require different analyses of observation data: the conditional nearest neighbour measure can be directly applied to observed galaxy catalogues, the spherical overdensity measure requires a reconstruction of the matter density field from the observed galaxy field, while the experienced gravity measure requires a derivation of the 3-dimensional Newtonian (and lensing) potential, which can be obtained by using weak lensing tomography. Because systematical errors in these analyses could lead to mis-identification of the environment, one can combine the different environment definitions if observational data allow.

We have also considered the screening of the fifth force inside dark matter subhaloes, and confirmed that the screening is stronger than in their host main haloes on average, as subhaloes have higher densities than their surroundings. However, the difference is small and the fifth force at the positions of simulation particles can act as a reasonable upper bound of subhaloes at the same positions. This result is useful, since it means that lower-resolution simulations of chameleon $f(R)$ gravity, even though unable to accurately resolve subhaloes, can still provide useful information about how well the fifth force is screened inside subhaloes and the galaxies in them.

Using our results, we will be able to make screening maps of the Universe. This will be left for a future work.

# Chapter 5

# How many galaxies will the Euclid redshift survey see?

## 5.1 Introduction

Understanding galaxy formation and the nature of dark energy are two of the most important and challenging problems in modern astrophysics and cosmology. Galaxy surveys provide powerful tools to investigate both issues. One of the lessons learned from previous surveys is the paramount importance of careful modelling of the survey data for the extraction of robust astrophysical results. Such modelling is best achieved using large cosmological N-body simulations to create mock versions of the real survey. Mock catalogues is essential to fully exploit and interpret the observed data from galaxy surveys. Mocks can help in various ways. For example, they can help to study selection biases and incompleteness arising from the selection of galaxies, to calibrate errors and explore systematic effects, to test new techniques to constrain cosmological parameters, etc. Building mock catalogues for different cosmological models can make direct predictions for dark energy surveys in order to distinguish $\Lambda$CDM and non-standard models.

The Euclid survey, which is scheduled for launch in 2021, will map the 3-dimensional distribution of matter in the Universe in order to show how dark energy affects the expansion history. To achieve this, Euclid is designed to measure accurate redshifts of tens of millions of galaxies and the shapes of more than a billion galax-

ies to study galaxy clustering and weak gravitational lensing. These measurements
will constrain cosmological parameters and alternative gravity models. The Euclid
survey is designed to measure the near infrared spectroscopy in wavelength range
$1100 - 2000$nm. The corresponding H$\alpha$ emitters in the redshift range $0.7 < z < 2.1$
are one of the main targets of Euclid survey. In this chapter, we use the Durham
semi-analytical galaxy formation model, GALFORM (Cole et al., 2000), to predict
the luminosity function of H$\alpha$ emitters (H$\alpha$LF). This is important because current
surveys of H$\alpha$ emitters cover solid angles that are orders of magnitude smaller than
Euclid. It is hard to match an empirical prediction of how many galaxies Euclid will
see. Current version of the GALFORM models are calibrated mostly using local ob-
servations in the optical and near-IR, but no emission line data. We test and explore
the validation of the GALFORM predictions for H$\alpha$ emitters, in order to determine
the number of objects above the Euclid mission's flux sensitivity threshold. This
number, along with the clustering of H$\alpha$ emitters determines the signal-to-noise in
power spectrum measurement of galaxy clusters, which influences the dark energy
figure of merit.

## 5.2  GALFORM

The Durham semi-analytical galaxy formation model, GALFORM, was firstly in-
troduced in Cole et al. (2000). It builds on the ideas from Cole (1991) and White &
Frenk (1991). Based on the initial inception, the subsequent revisions, as described
in Bower et al. (2006), Lagos et al. (2011), Gonzalez-Perez et al. (2014) and Lacey
et al. (2016), introduce more detailed and improved modelling of physical processes
and galaxy properties. In this section, we give a brief introduction to GALFORM.

GALFORM models galaxy formation from its beginning, the linear power spec-
trum of density fluctuations in a specific cosmology, to the end, predicted properties
for the galaxy population at different redshifts. The general picture of galaxy for-
mation is gas collecting and cooling in dark matter haloes, which then leads to
star formation; this process is regulated by feedback such as supernovae. Modelling
galaxy formation in GALFORM is treated in two stages. Firstly, the formation of

dark matter haloes is modelled according to the gravitational collapse of the dark matter. The cosmic structure grows hierarchically such that smaller halos form earlier and then accrete or merge over time to create larger halos. The halo merger tree is built using the outputs of N-body simulations or a Monte Carlo technique based on the extended Press-Schechter theory (Peacock & Heavens, 1990), to track the growth and merger of dark matter haloes. In the second stage, GALFORM describes the baryonic physics using a set of equations within the dark matter merger tree. These semi-analytical equations are designed to model the complicated and important physical processes related to galaxy formation. The baryonic matter in GALFORM falls into five components: (i) hot halo gas, (ii) cold gas in galaxies, (iii) ejected gas outside the virial radius of haloes, (iv) stars and (v) supermassive black holes. GALFORM essentially tracks the exchange of mass and metals between them. Disc galaxies form through the cooling of hot gas, whereas the bulge or spheroidal galaxies form either by a galaxy merger event or following a disc instability. Star formation happens in the cold molecular. The feedback from supernovae reheats the cold gas to hot gas, whilst the heating from active galactic nuclei (AGNs) stops the gas cooling in the first place. As these physical processes are complex and somewhat poorly understood, GALFORM introduces a number of "free" parameters. These parameters are physical and not statistical, and are calibrated by comparing the predictions of the model against a set of observational data. Also, the available parameter space is also highly depending on the model itself. A more powerful model which can predict a wider range of galaxy properties would have a smaller parameter space available than a more naive model.

In this chapter, we use the halo mergers tree from Millennium simulation (Springel et al., 2005), and MillGas simulation which has the same particle number and box size as the but use the WMAP7 cosmology (Guo et al., 2013). The GALFORM recipes, Bow06, Lagos12, Gonzalez13 and Lacey14 (Bower et al., 2006; Lagos et al., 2011; Gonzalez-Perez et al., 2014; Lacey et al., 2016), are used to make predictions for the number and properties of H$\alpha$ emitters.

## 5.3    Emission lines in GALFORM

H$\alpha$ emission originates from the HII region of galaxies, and its luminosity is proportional to the number of Lyman continuum photons. In GALFORM, the HII regions are assumed to have a uniform density of 10 hydrogen particles per cm$^3$, and each HII region has one ionising star in the center with an effective temperature of 45000 K. GALFORM calculates the number of Lyman continuum photons using eight HII region models, which are developed by Stasińska (1990), spanning a range of metallicities. The ionising parameter of these HII region models is depending on their metallicity, but the actual value is nearly invariant around $10^{-3}$.

The main uncertainty in H$\alpha$ line is the dust extinction. In GALFORM, the attenuation by dust at a given wavelength is computed using the results of a radiative transfer model, in which the inclination of the galaxy, the cold gas mass and metallicity are required to input. GALFORM treats the dust in galaxies as two components: diffuse dust (75%) and molecular clouds (25%). The diffuse component is assumed to follow the distribution of stars. Stars are assumed to have the same metallicity as their birth molecular clouds, and will escape from their birth molecular clouds after 1 million years time. The more detailed modelling of dust extinction can be seen in Gonzalez-Perez et al. (2013).

## 5.4    Empirical luminosity functions

Apart from semi-analytical models, empirical luminosity functions can be employed to make forecasts for galaxy redshift surveys. The Euclid survey will use the H$\alpha$ emission line to measure the redshifts of galaxies. The H$\alpha$LF at $z > 0.7$ is one of the major inputs to forecast cosmological constraints from Euclid. There are plenty of existing H$\alpha$LF measurements since Gallego et al. (1995), which cover a wide redshift range from 0 to 2.3. However, these measurements show large uncertainties and are often inconsistent with one another. It is impossible to recommend a unique model with only its statistical error associated, because this would be based on a predefined evolutionary and luminosity function shape. In this chapter, following Pozzetti et al. (2016), we use three different forms of empirical functions (named

"Model 1", "Model 2" and "Model 3") to describe the evolution in redshift of the observed HαLFs. Different subsets of input data and treatment of systematic errors are used to explore the uncertainties and robustness of the predictions. Full details can be found in Table 1 of Pozzetti et al. (2016). In this section, we give a brief review of the three empirical luminosity functions in turn.

### 5.4.1 Model 1

This model uses the Schechter parametrization (Schechter, 1976) for the LFs,

$$\phi(\log_{10} L, z)d\log_{10} L = \ln 10 \; \phi^\star \left(\frac{L}{L^\star}\right)^{(\alpha+1)} e^{-L/L^\star} \; d\log_{10} L, \tag{5.4.1}$$

where $\phi^\star(z)$ is the characteristic density of Hα emitters, $\alpha$ is the faint-end slope and $L^\star(z)$ is the luminosity at which the HαLF falls exponentially from the extrapolated faint-end power law.

The time evolution for $L^\star(z)$ was introduced in Geach et al. (2010).

$$L^\star(z) = L_0^\star \times (1+z)^\delta, \tag{5.4.2}$$

and the evolution of $\phi^\star$ used is

$$\phi^\star(z) = \begin{cases} \phi_0^\star \times (1+z)^\epsilon, & \text{for } z < z_{\text{break}} \\ \phi_0^\star \times \frac{(1+z_{\text{break}})^{2\epsilon}}{(1+z)^\epsilon}. & \text{for } z > z_{\text{break}} \end{cases} \tag{5.4.3}$$

The subscript 0 represents $z = 0$.

The model parameters are constrained using the observed luminosity functions at different luminosities and redshifts using a $\chi^2$ approach. The best-fitting values are: $\alpha = -1.35$, $L_0^\star = 10^{41.5}$erg/s, $\phi_0^\star = 10^{-2.8}$Mpc$^{-3}$, $\delta = 2$, $\epsilon = 1$, $z_{\text{break}} = 1.3$.

### 5.4.2 Model 2

Model 2 uses the same Schechter function for the LFs, but adopts a different evolutionary form for $L^\star(z)$

$$\log_{10} L^\star(z) = -c(z - z_{\text{break}})^2 - \log_{10} L^\star_{z_{\text{break}}}, \tag{5.4.4}$$

and $\phi^\star(z)$ is regarded as a constant.

The fitting method and observational data used to constrain Model 2 is the same as Model 1. The value of the parameters are $\alpha = -1.4$, $\phi^\star = 10^{-2.7}\text{Mpc}^{-3}$, $c = 0.22$, $z_{\text{break}} = 2.23$, $L^\star_{z_{\text{break}}} = 10^{42.59}\text{erg/s}$.

### 5.4.3 Model 3

This model takes a broken power law functional form for the LFs:

$$\phi(\log_{10} L, z)d\log_{10} L = \ln 10\ \phi^\star \left(\frac{L}{L^\star}\right)^{(\alpha+1)} \left[1 + (e-1)\left(\frac{L}{L^\star}\right)^\Delta\right]^{-1} d\log_{10} L, \tag{5.4.5}$$

where $L^\star$ is a function of redshift:

$$\log_{10} L^\star(z) = \log_{10} L^\star_\infty + \left(\frac{1.5}{1+z}\right)^\beta \log_{10} \frac{L^\star_{0.5}}{L^\star_\infty}, \tag{5.4.6}$$

and $\phi^\star(z)$ is a constant. In this model, $\Delta$ is the difference between the bright and faint-end slopes. $\beta$ controls the sharpness of the fall-off in $L^\star$ at low redshift.

The parameters of Model 3 are constrained using the data from HiZELS (Sobral et al., 2013), WISP (Colbert et al., 2013), and NICMOS (Yan et al., 1999; Shim et al., 2009) only. The procedure was designed specifically for use only in the redshift ranges under consideration for the Euclid and WFIRST-AFTA slitless surveys (in particular at $0.7 < z < 2.23$). The best-fitting values obtained using a Monte Carlo Markov chain are $\alpha = 1.587$, $\phi^\star = 10^{2.920}\text{Mpc}^{-3}$, $\Delta = 2.288$, $L^\star_\infty = 10^{42.956}\text{erg/s}$, $L^\star_{0.5} = 10^{41.733}\text{erg/s}$, $\beta = 1.615$. Model 3 is not recommended for use at $z < 0.6$ because it does not incorporate the low-redshift data.
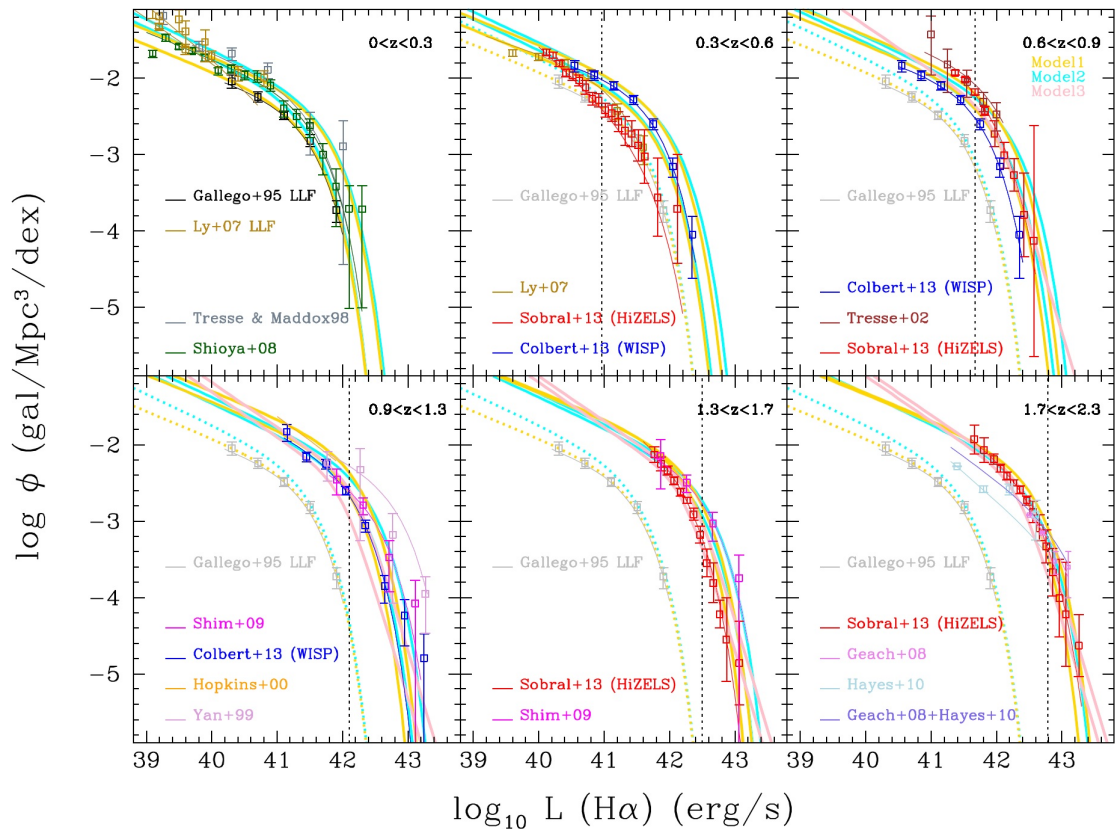
Figure 5.1: The Hα luminosity functions of model 1, 2, and 3, compared to observed LFs. The dotted lines mark the nominal flux limit of Euclid $(3 \times 10^{16} \mathrm{erg/cm^2/s})$ in the lower bound of each redshift range. Observed Schechter LFs are shown as thin lines and squares in the observed luminosity range and listed in the labels. For comparison, the LFs from empirical models 1, 2, and 3 are shown (in yellow, cyan, and pink, respectively) as thick lines in the same redshift range (shown in the two extremes of each redshift bin). Reproduced from Pozzetti et al. (2016).

## 5.5   Empirical models vs observed Hα luminosity functions

The three empirical models are plotted in Fig. 5.1 in different redshift bins, and compared to the observed HαLFs. Note that all the observed HαLFs used in the fitting and comparison are shown in terms of observed Hα flux, i.e. with no correction for extinction in the target galaxy. Generally, the measurements of extinction are unavailable. Usually, an average extinction of 1 magnitude is adopted by most the observers. In cases, where such corrections have been applied in the literature, we have undone the correction.

Overall, all of the empirical models from Pozzetti et al. (2016) can provide a good description of the observed HαLFs. However, this is due to the large scatter in the observed LFs covering similar redshift ranges. We note that at $z > 0.9$ the various empirical HαLFs start to disagree, as is clear from their Schechter parameters. Despite the empirical uncertainties, the strong luminosity evolution of the bright end of the HαLF with increasing redshift is clearly evident, as confirmed by the evolution of $L^\star$ by about an order of magnitude over the whole redshift range. On the other hand, the amount of density evolution is still not completely clear, as well as the exact value and evolution of the faint end slope.

## 5.6 Empirical models vs GALFORM

We use the semi-analytical galaxy formation model, GALFORM, to predict the HαLF for Euclid. Fig 5.2 shows the comparison between the GALFORM variants, Gonzalez13 (Gonzalez-Perez et al. 2013), Lacey14 (Lacey et al. 2015, in preparation), Lagos12 (Lagos, Lacey & Baugh 2012) and Bow06 (Bower et al. 2006), and the three empirical models. The Gonzalez13 and Lacey14 models use the cosmology and merger trees of the MillGas simulation ($H_0 = 70.4$ km/s/Mpc, $\Omega_m = 0.272$ and $\Omega_\Lambda = 0.728$). The Lagos12 and Bow06 models use the cosmology and merger trees of the Millennium simulation ($H_0 = 73$ km/s/Mpc, $\Omega_m = 0.25$ and $\Omega_\Lambda = 0.75$). We can see in Fig 5.2 that, at $z = 0.83$ and higher redshifts, the GALFORM predictions are generally below the empirical models, especially at the bright end. Here the GALFORM predictions include the effect of dust extinction, as calculated for the continuum at the wavelength of Hα.

Because there are large uncertainties in the empirical HαLF parameters, it is possible to make the empirical models agree with the GALFORM predictions by tuning these parameters. However, as our goal is to test and improve the GALFORM predictions, we use three empirical HαLFs with the best-fit values as the reference models. Since these have been tuned to match various data sets, the GALFORM predictions of HαLF are lower than the empirical models at the bright end, we apply two approaches to improve the GALFORM predictions: one is modifying the dust
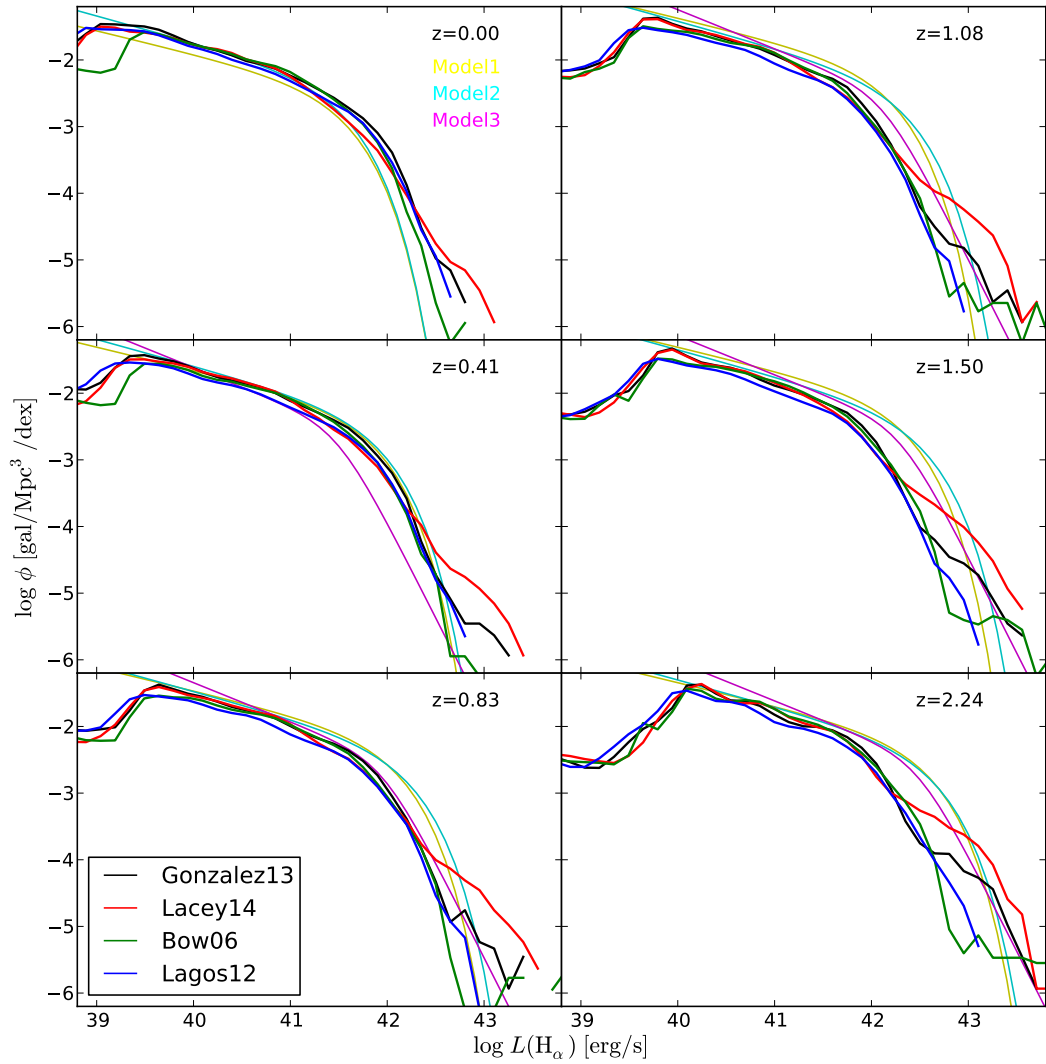
Figure 5.2: The Hα LFs of empirical model 1, 2, and 3 in thin lines labelled according to the legend in the top left panel, compared to LFs of GALFORM models, Gonzalez13, Lacey14, Lagos12 and Bow06 in thick lines as labelled in the bottom left panel.

extinction model, and the other is tuning GALFORM parameters. Hereafter in this section, we focus on the GALFORM Gonzalez13 model.

The effect of dust extinction can change the bright end of the H$\alpha$LF. As we know, there is no direct measurement of dust extinction in H$\alpha$ emitters. The dust extinction can be inferred if we have measurement of other H lines. Intrinsically these lines are expected to have a particular luminosity ratio without dust. The actual line ratio measured let us estimate the dust extinction. The uncertainty of GALFORM dust extinction model depends on the prediction for the galaxy shapes. There are incorrect for galaxies' luminosity, e.g. some galaxies have unreasonably small disks which can lead to very high extinctions. Hence, we decide to modify the dust model phenomenologically. In Fig. 5.3, we make a scatter plot of the extinct H$\alpha$ luminosity against H$\alpha$ luminosity without dust for all the galaxies at $z = 1.5$ as predicted by Gonzalez13 model. For galaxies which are brighter than $10^{41}$ erg/s, 13.3% of them (3385 out of 25315) shows more dust extinction than 1 magnitude (marked by the red dashed line). This is extremely different from the observers' assumed dust extinction.

Following the dust extinction correction used by observers, we set a upper limit, 1 magnitude, to the dust extinction, i.e. if a galaxy is presented to have more than 1 magnitude of dust extinction, we force it to be 1 magnitude. Fig. 5.4 shows the H$\alpha$LF of Gonzalez13, Gonzalez13 without dust and Gonzalez13 with maximum 1 magnitude dust extinction, which is labelled as "max 1 mag dust" in the plot. Comparing with the original Gonzalez13, this "max 1 mag dust" model changes a little at the bright end, but is still not consistent with the empirical models. However, it is clear that the predictions of the Gonzalez13 model without the effect of dust agree with the empirical models much better. Although there is a bump at brightest end of H$\alpha$LF. Considering the low number density, these bumps will not affect the number counts, which depends on the LF around $L^{\star}$, but could influence the tail of the redshift distribution of H$\alpha$ emitters.

By varying the galaxy formation parameters which relate to star-forming galaxies in GALFORM, we can try to bring the H$\alpha$LF prediction into closer agreement with to the empirical models. We build a new model, called "H$\alpha$ tuned" by varying the
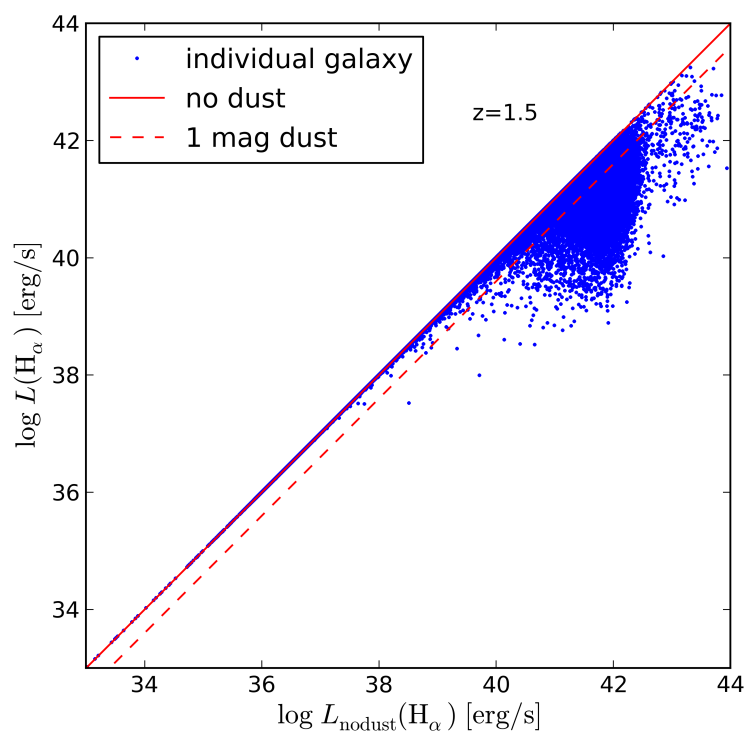
Figure 5.3: The extinct Hα luminosity (y-axis) plotted against the Hα luminosity without dust (x-axis) for all galaxies at $z = 1.5$ as predicted by Gonzalez13 model. The red solid line and dashed line indicate the galaxies without dust extinction and galaxies with 1 magnitude of dust extinction, respectively.
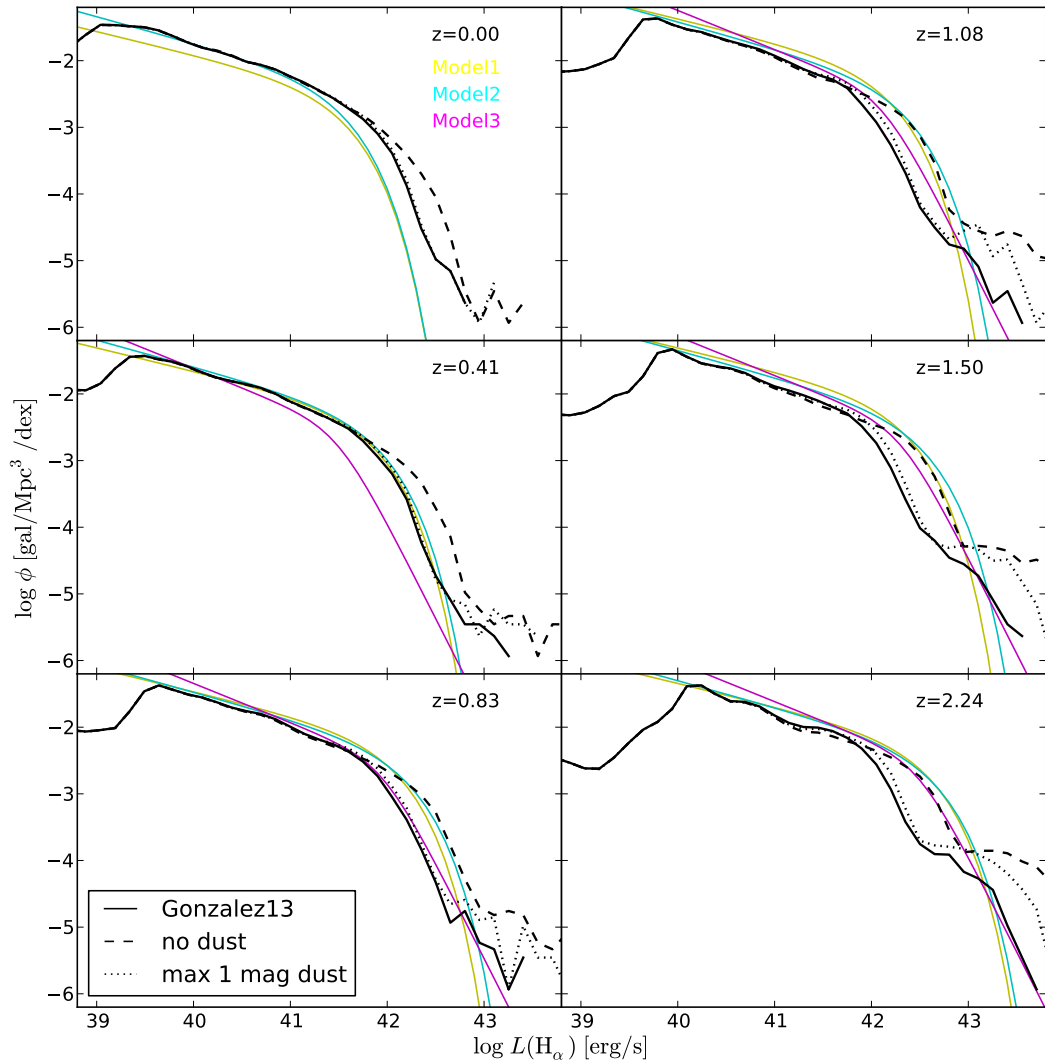
Figure 5.4: The Hα LFs of empirical model 1, 2, and 3 plotted in thin solid lines labelled according to the legend in the top left panel, compared to LFs of GALFORM Gonzalez13 model, the Gonzalez13 model without dust extinction (labelled as "no dust") and the Gonzalez13 model with the maximum applied extinction capped at 1 magnitude.

AGN feedback parameter and minimum star formation rate timescale for star burst in Gonzalez13. Fig 5.5 shows the comparison between Gonzalez13, Hα tuned and the three empirical models. The Hα tuned model fits with empirical models much better for $z \geq 0.83$ and does not have the bump at bright end. We have tested that the tuned version of Gonzalez13 does not change the clustering of Hα emitters, as quantified using the effective halo mass of the Hα emitters that will be seen by Euclid. Despite the great success in HαLF, this model is only a preliminary test of tuning GALFORM parameters. Modifying these parameters would potentially bring influences to many other galaxy properties, which we have not fully tested yet. For example, this model does not match the present-day LF. However, at least, the "Hα tuned" model gives us an positive example about the possibility to tune and constrains the GALFORM by emission line observed LFs.

## 5.7 The surface density of Hα emitters

Fig. 5.6 and Fig. 5.7 show the cumulative galaxy counts as a function of Hα flux limit predicted by the empirical models and GALFORM in the redshift range $0.7 < z < 1.5$ covered by the WISP slitless data, and $0.9 < z < 1.74$ which is defined by the Euclid red grism ($1.25 < \lambda < 1.8$m). The three original GALFORM models underestimate the number counts compared to the empirical models. The no dust model works much better. It agrees with empirical models quite well below a flux limit of $5 \times 10^{-16}$ erg/s/cm$^2$. But again, there is a bump at the bright end. Similar behaviour is seen in the no dust version of the Lagos12 model. The Hα tuned model nearly mimics model 3 and converge with WISP data. It meets our expectation because the LFs of Hα tuned model are pretty close to the LFs of empirical models in both redshift range (see Fig 5.5).

We use two flux limits: one is the depth of the Euclid Wide survey, $> 3 \times 10^{-16}$erg/s/cm$^2$; the other one is $> 2 \times 10^{-16}$erg/s/cm$^2$ corresponding to the 4 RED grism option, i.e. 4 position angles and therefore double the exposure time compared with the red book (Laureijs et al., 2011). Table 5.1 shows the number counts of Hα emitters at these two flux limits in the redshift range $0.9 < z < 1.74$. The no
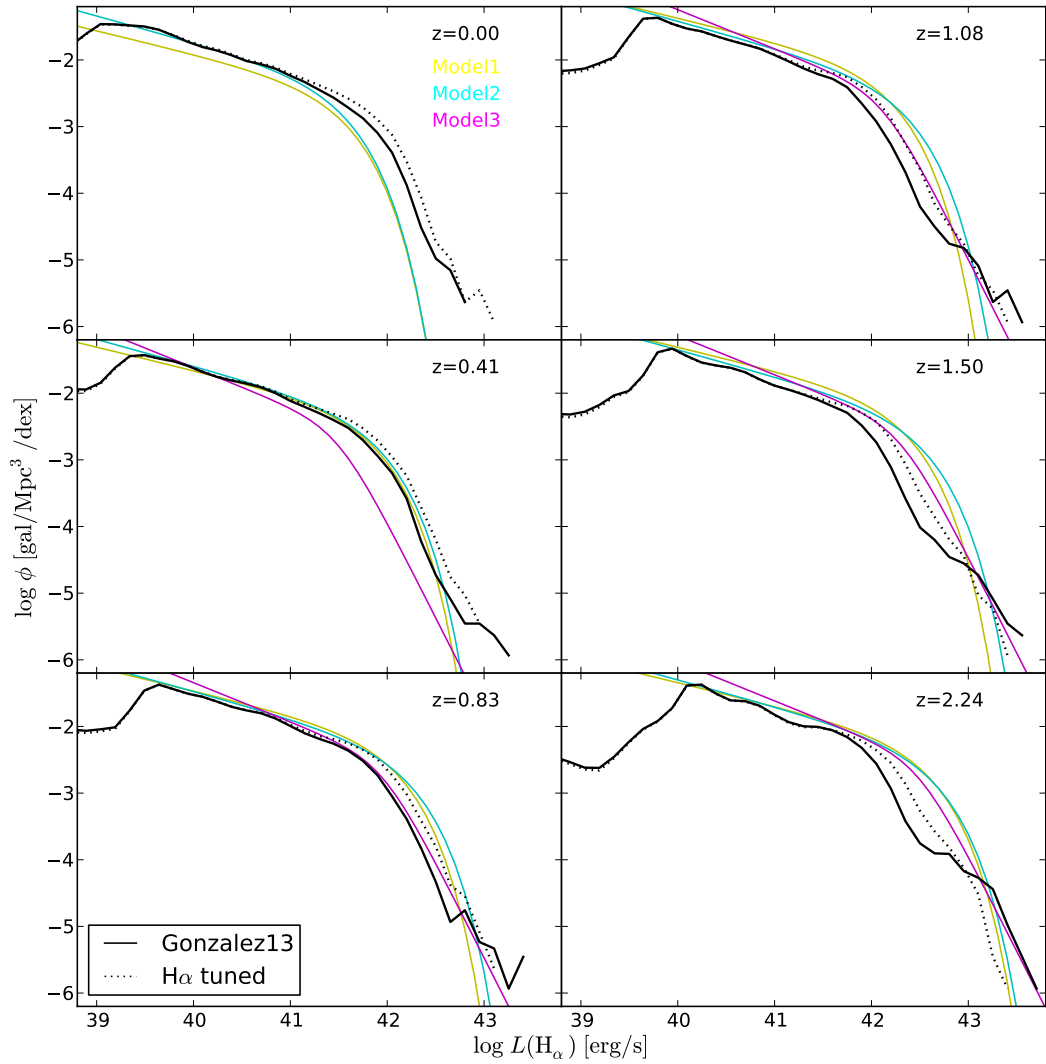
Figure 5.5: The Hα LFs of empirical model 1, 2, and 3 plotted in thin solid lines labelled according to the legend in the top left panel, compared to LFs of GAL-FORM Gonzalez13 model and the Hα tuned model developed from varying selected parameters from Gonzalez13, as labelled in the bottom left panel.

Table 5.1: The summary of the number counts of Hα emitters at redshift range $0.9 < z < 1.74$ for the models as labeled. The first line and second line are the number counts per square degree at flux limits of $3 \times 10^{-16}$ and $2 \times 10^{-16}$erg/s/cm$^2$

| Model1 | Model2 | Model3 | Gonalez13 | no dust | Hα tuned | Lacey14 | Lagos12 | Bow06 |
|--------|--------|--------|-----------|---------|----------|---------|---------|-------|
| 1500 | 2150 | 1000 | 300 | 2000 | 950 | 800 | 230 | 180 |
| 3800 | 4650 | 2450 | 800 | 4100 | 2450 | 1400 | 680 | 500 |

dust model predicts similar number counts to model 2 for the lower flux limit, but extremely over-estimates the counts under the higher flux limit. Meanwhile, the "Hα tuned" model has very similar prediction to Model 3 in both flux limits.

## 5.8 The redshift distribution of Hα emitters

The corresponding redshift distributions of Hα emitters at 2 flux limits ($3 \times 10^{-16}$ and $2 \times 10^{-16}$erg/s/cm$^2$) for the Euclid Wide surveys are shown in Fig 5.8 and Fig 5.9. It is clear that the original GALFORM models predicts much fewer Hα emitters than the empirical models at $z > 0.25$. Meanwhile, the "Hα tuned" model agrees slightly better with the empirical models, but still obviously underestimates number of Hα emitters when $z > 1$. The no dust model is similar to model 1 and model 2 at $z < 1.5$. But at higher redshifts, the redshift distribution remains constant which is not consistent with empirical models. This is because at higher redshifts, only the extremely bright galaxies can be observed. Hence, the bumps at bright end of the LFs in no dust models becomes the main source of these galaxies.

## 5.9 Conclusions $ discussions

In this chapter, we review the Hα emitter predictions made using a semi-analytical galaxy formation model, GALFORM, and investigate the possibilities to improve the model in order to make reliable forecasts for the Euclid survey. As GALFORM has not be calibrated using emission line data or high-redshift observations, the original GALFORM models generally underestimate the number of bright Hα emitters, comparing to the empirical LFs. We adopt two methods to improve the prediction of GALFORM model: one is to modify the dust extinction model in GALFORM and
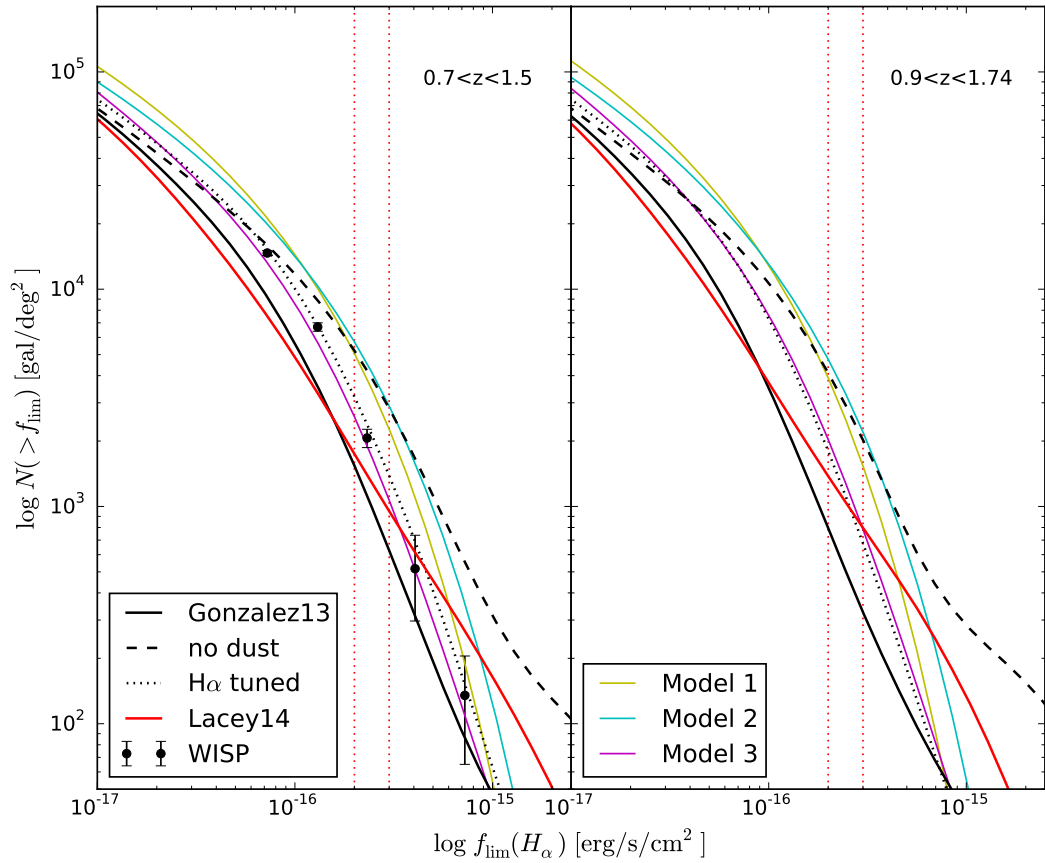
Figure 5.6: Cumulative H$\alpha$ flux number counts of the empirical models, GALFORM Gonzalez13 model, the Gonzalez13 model without dust extinction, H$\alpha$ tuned model and Lacey14 model. These models are integrated over two redshift ranges, $0.7 < z < 1.5$ (left panel) and $0.9 < z < 1.74$ (right panel). The red dotted lines indicate the two Euclid flux limits, $2 \times 10^{-16}$ and $3 \times 10^{-16}$ erg/s/cm$^2$. The observational data is obtained from WISP by Colbert et al. (2013).
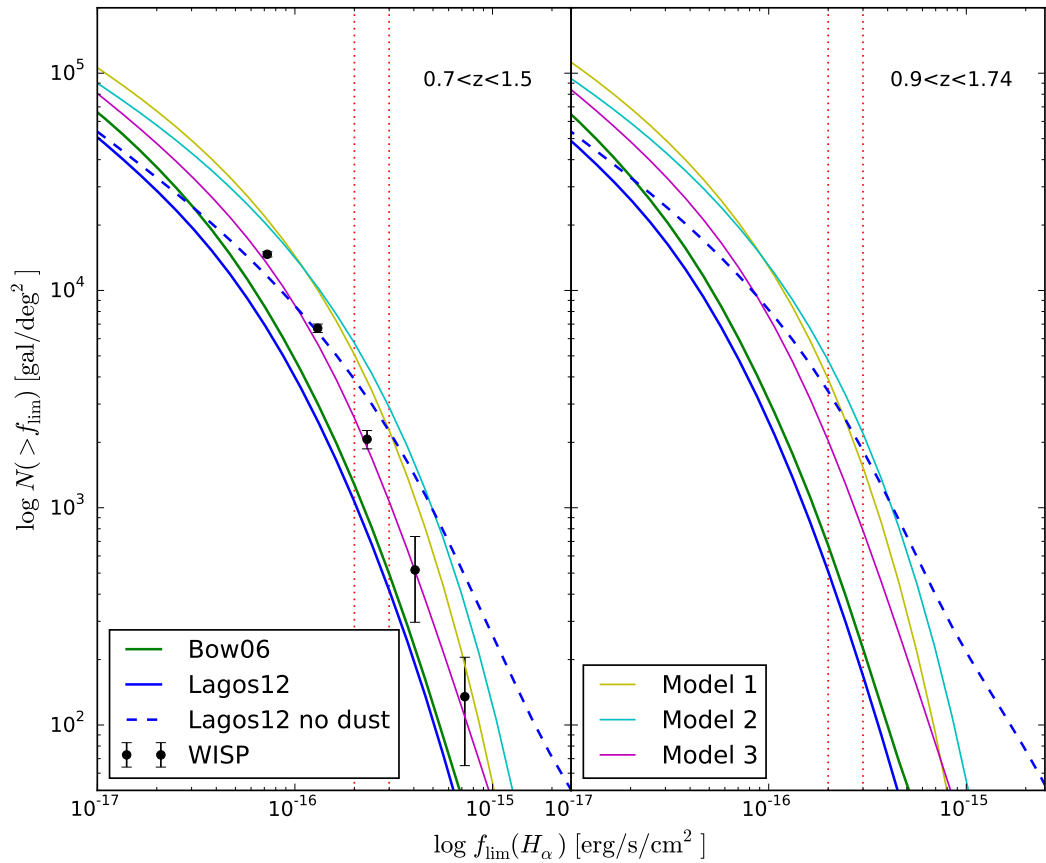
Figure 5.7: Cumulative H$\alpha$ flux number counts of the empirical models, GALFORM Bow06, Lagos12 and the Lagos12 models without dust extinction. These models are over two redshift ranges, $0.7 < z < 1.5$ (left panel) and $0.9 < z < 1.74$ (right panel). The red dotted lines indicate the two Euclid flux limits, $2 \times 10^{-16}$ and $3 \times 10^{-16}$ erg/s/cm$^2$.
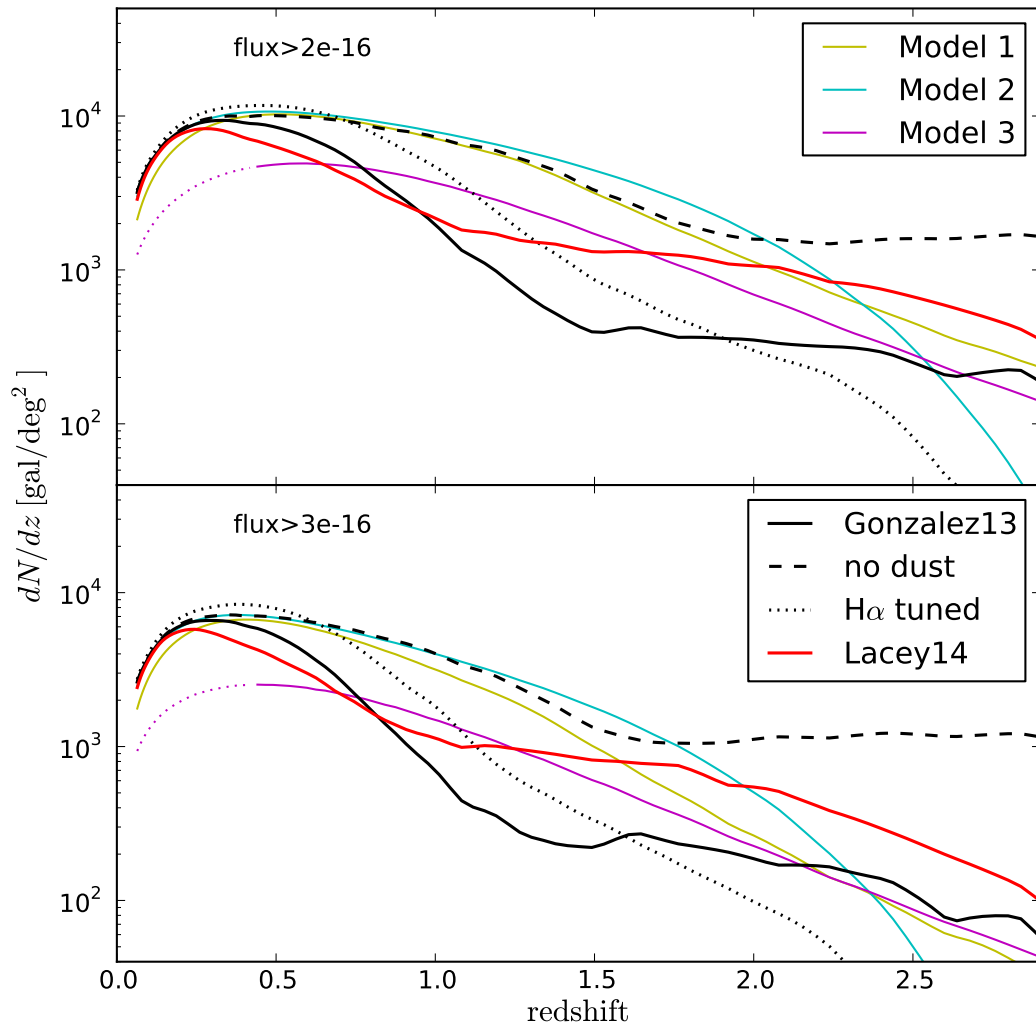
Figure 5.8: The Hα redshift distribution of the empirical models, the GALFORM Gonzalez13 model, the Gonzalez13 model without dust extinction, Hα tuned model and the Lacey14 model above the Euclid flux thresholds of $2 \times 10^{16}$ erg/s/cm$^2$ (top panel) and $3 \times 10^{16}$ erg/s/cm$^2$ (bottom panel).
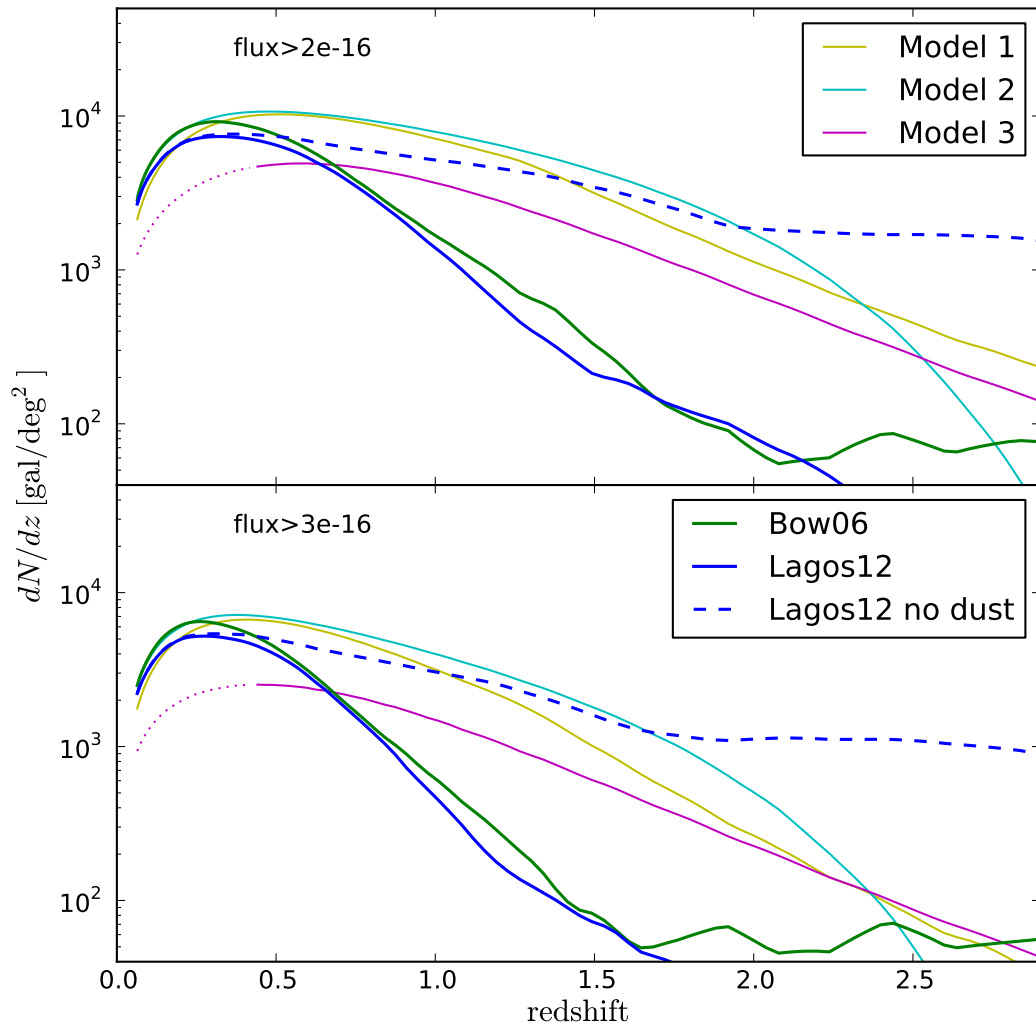
Figure 5.9: The Hα redshift distribution of the empirical models, GALFORM Bow06, Lagos12 and the Lagos12 models without dust extinction above the Euclid flux thresholds of $2 \times 10^{16}$ erg/s/cm$^2$ (top panel) and $3 \times 10^{16}$ erg/s/cm$^2$ (bottom panel).

the other one is to tune the GALFORM parameters which relates to star-forming galaxies. Here we conclude that the GALFORM predictions can match the number counts of Hα emitters with the empirical models either by removing dust extinction or re-calibrating the galaxy formation model. But the redshift distribution of Hα emitters is still a problem. Re-calibrating the galaxy formation model would potentially change other galaxy properties, which has not be studied. We recommend the GALFORM Hα emitters without dust extinction as a best-bet prediction for the Euclid survey. The mock catalog made by GALFORM can be used to forecast the number counts and redshift distribution of Hα emitters at $z < 2$, after removing the dust extinctions.

Only ΛCDM model is investigated in this chapter. We shall use GALFORM to build mock catalogues for non-standard cosmological models in the future. In the early dark energy cosmology (studied in Chapter 2), due to the non-negligible amount of dark energy at very high redshift, the fast expansion of the Universe suppress the growth of structure. The abundance of Hα emitters in EDE should be smaller than that in ΛCDM, especially at high redshifts. In the $f(R)$ cosmology (see Chapter 3), there are more Milky Way size haloes at low redshift than that in ΛCDM. We shall expect to observe more Hα emitters at the fainter side of luminosity function. However, not only the expansion history and halo abundance, but also the halo merger history, halo inner structure and enhanced gravity can affect galaxy formation. To accurate building the dark energy or modified gravity mock catalogues needs more detailed modelling of the galaxy formation.

# Chapter 6

# Overall Conclusions & Future Work

In this Chapter we summarise the main conclusions of this thesis and outline some future work.

The standard cosmological model, $\Lambda$CDM, has been remarkably successful at fitting many observational results. But the cosmological constant, $\Lambda$, which is thought to describe the dark energy, is afflicted by the "fine-tuning" problem and "coincidence" problem. This thesis is concerned with the study of alternative cosmological models which could explain the accelerating expansion of Universe. There are mainly two ways to revise the standard cosmological model: one is to replace the cosmological constant with other form of dark energy, like a dynamic scalar field. These fields are usually motivated theoretically and can avoid the fine-tuning and coincidence problems; the other is to modify the theory of gravity itself. In these modified gravity models, the accelerating expansion is cause by gravity theory at very large scales where it has not been test yet. In this thesis, we apply N-body simulations to explore these alternatives to $\Lambda$CDM.

In Chapter 2, we study a typical example of dynamical dark energy model. There is a non-negligible amount of dark energy at early times of cosmic expansion history, whilst the effect of dark energy can be ignored in $\Lambda$CDM when $z > 3$. Considering the function formats proposed for these early dark energy models can be quite different, it is impossible to do simulations for every single model. We

parametrize the behaviour of early dark energy models phenomenologically using the functions introduced by Doran & Robbers (2006) and Wetterich (2004). Firstly, we use CMB and BAO data to constrain the two parameterizations. The Wetterich model is ruled out as the fittings to current observations returns a existing of early dark energy that is $10^{-7}$ times the critical density. We then run N-body simulations to investigate the difference between $\Lambda$CDM and Doran & Robberts model with 1% and 2% early dark energy. We find that, the early dark energy cosmology has obviously fewer halos than $\Lambda$CDM at high redshifts due to the faster expansion and more than 15% difference in the large-scale power spectrum. Measuring the shape of large-scale power spectrum is a promising way to distinguish early dark energy from a cosmological constant in future galaxy surveys.

In Chapter 3, we concentrate on a modified gravity model, in which the Ricci tensor, $R$, in general relativity is replaced with a function of $R$. In particular, we study the $f(R)$ model, which was developed by Hu & Sawicki (2007), with parameter $n = 1, |f_{R0}| = 10^{-5}$ (F6 model). This results in 1/3 extra amount gravity force in low density region and uses the Chameleon screening mechanism to suppress the enhancement of gravity in high density regions. We run high-resolution N-body simulations (LIMINALITY) of F6 and GR. We find that, at low redshift, halos less massive than $10^{13} M_\odot/h$ in the F6 model have a much more condensed inner structure than in standard $\Lambda$CDM. The halo concentration is remarkably enhanced for low-mass haloes in this model due to a deepening of the total gravitational potential. Contrary to the naive expectation, the halo formation time is later for low-mass haloes in this model, a consequence of these haloes growing faster than their counterparts in $\Lambda$CDM at late times. Subhaloes, especially those less massive than $10^{11} M_\odot/h$, are substantially more abundant in the F6 model for host haloes less massive than $10^{13} M_\odot/h$. We discuss the implications of these results for the Milky Way satellite abundance problem. Although the overall halo and subhalo properties in this borderline f(R) model are close to the $\Lambda$CDM predictions, our results suggest that studies of the Local Group and astrophysical systems, aided by high-resolution simulations, can provide valuable for further tests of gravity.

We further study the halo environment in F6 gravity using the LIMINALITY

simulations in Chapter 4. We test the validity of different definitions of environment by measuring the correlation between one another and to the fifth-force potential which is calculated directly from the high-resolution N-body simulation. We find that, although the different ways to define environment in practice do not agree with one another perfectly, they can provide useful guidance, and cross checks about how well a dark matter halo is screened. In addition, the screening of subhaloes in dark matter haloes is primarily determined by the environment, with the subhalo mass playing a minor role, which means that lower-resolution simulations where subhaloes are not well resolved can still be useful for understanding the modification of gravity inside subhaloes. This result can be used in existing and future galaxy surveys to constrain $f(R)$ gravity and will also affect galaxy formation modelling in $f(R)$ cosmology. It also worth to extend this work to other gravity models.

Galaxy surveys are a powerful tool to investigate the nature of dark energy. However, only bright galaxies rather than dark matter can be directly observed. The modelling of galaxy formation is essential to connect the dark matter simulations to the observables. The Euclid survey will measure the redshifts of a large number of galaxies through the H$\alpha$ emission. In Chapter 5, we studied the H$\alpha$ luminosity function predicted by the semi-analytical galaxy formation model, GALFORM, which is used to build mock galaxy catalogs for the Euclid survey. Although GALFORM has not been calibrated using emission line data, the H$\alpha$LFs predicted by GALFORM roughly agree with the empirical models of observed luminosity functions in the redshift range Euclid survey will cover, except for an underestimate at the bright end. We apply two ways to improve GALFORM H$\alpha$LFs, one is modifying the dust extinction model and the other is tuning the galaxy formation parameters which affect the star-forming galaxies. We find that switching off the dust extinction in GALFORM can make the H$\alpha$LFs match the empirical models and predicts similar H$\alpha$ emitter number counts and redshift distribution up to $z = 2$. Refining the galaxy formation model is also a possible way to improve the GALFORM H$\alpha$LFs. But the potential side effects to other galaxy properties needs to be further investigated. For example, it remains to be seen if the refined model can reproduce the $z = 0$ observational luminosity function.

Overall, we study the typical alternative cosmological models in this thesis. The early dark energy model mainly affects the large-scale structure of the Universe, due to its distinct expansion history from $\Lambda$CDM. On the other hand, the major effects of $f(R)$ model is on small scales at late time of the Universe, because of the enhancement of gravity on low density region. Both the large-scale and small-scale effects would have imprints in the galaxy surveys. Although the galaxy formation modelling in dark energy or modified gravity model is complicated. The abundance of H$\alpha$ emitters would be different if we do not live in $\Lambda$CDM universe. In early dark energy cosmology, less H$\alpha$ emitters will be observed because of the smaller number of dark matter haloes. In the $f(R)$ model, more faint H$\alpha$ emitters are expected at low redshifts. Building mock catalogues for alternative cosmological models can give a light to distinguish them from $\Lambda$CDM.

The next generation of galaxy surveys, like DESI (Levi et al., 2013), Euclid and WFIRST (Spergel et al., 2013), aims to measure the linear perturbation theory relation between the density and velocity fields to roughly 1 per cent precision. The high-precision linear growth rate estimated from these surveys provides a direct constraint on the expansion history which is then used to test cosmological models. The detailed modelling of redshift space distortions caused by the peculiar velocity is required to achieve such high precision. In Chapter 2, we have measured the redshift-space power spectrum of early dark energy cosmology. There are obvious differences between early dark energy and $\Lambda$CDM at large scales in monopole and quadrupole moments. We are planning to apply the study to $f(R)$ and normal branch of DGP modified gravity models. Furthermore, we examine the full 2D power spectrum in order to in order to isolate the impact of non-linear growth and redshift space distortion effects. Some preliminary results are shown in Appendix B.

More interestingly, sterile neutrino, which is a candidate of warm dark matter, has some very similar cosmological effects as early dark energy. Sterile neutrino behaves like radiation at early universe and rapidly transit to zero pressure particles, like dark matter, at later time. A $\Lambda$CDM universe with sterile neutrino would have very similar background evolution history with early dark energy universe. We did

not consider the sterile neutrino effects in our N-body simulations in Chapter 2 and 3. Studying the degeneracies between sterile neutrino and early dark energy effects is a very promising project to reduce the complexity of numerous alternative cosmological models.

# Bibliography

Abbott B. P. et al., 2016a, Physical Review Letters, 116, 061102

Abbott T. et al., 2016b, Phys. Rev. D, 94, 022001

Allen S. W., Evrard A. E., Mantz A. B., 2011, ARA&A, 49, 409

Alonso D., 2012, (arXiv:1210.1833)

Amendola L., 2000, Phys. Rev. D, 62, 043511

Amendola L., Gannouji R., Polarski D., Tsujikawa S., 2007, Phys. Rev. D, 75, 083504

Anderson L. et al., 2014, MNRAS, 441, 24

Angulo R. E., Baugh C. M., Frenk C. S., Lacey C. G., 2008, MNRAS, 383, 755

Arnold C., Puchwein E., Springel V., 2014, MNRAS, 440, 833

Arnold C., Puchwein E., Springel V., 2015, MNRAS, 448, 2275

Ata M. et al., 2017, MNRAS, 467, 3993

Avila S. et al., 2014, Mon. Not. Roy. Astron. Soc., 441, 3488

Babichev E., Deffayet C., Ziour R., 2009, International Journal of Modern Physics D, 18, 2147

Barnes J., Hut P., 1986, Nature, 324, 446

Barreira A., Li B., Hellwing W. A., Baugh C. M., Pascoli S., 2014a, J. Cosmo. Astropart. Phys., 1409, 031

Barreira A., Li B., Hellwing W. A., Lombriser L., Baugh C. M., et al., 2014b, J. Cosmo. Astropart. Phys., 1404, 029

Bassett B. A., Corasaniti P. S., Kunz M., 2004, ApJ, 617, L1

Baugh C. M., 2006, Reports on Progress in Physics, 69, 3101

Behroozi P. S., Wechsler R. H., Wu H. Y., 2013, Astrophys. J., 762, 109

Bel J., Brax P., Marinoni C., Valageas P., 2015, Phys. Rev. D, 91, 103503

Benson A. J., 2010, Phys. Rep., 495, 33

Berlind A. A., Weinberg D. H., 2002, ApJ, 575, 587

Beutler F. et al., 2011, MNRAS, 416, 3017

Boisseau B., Esposito-Farèse G., Polarski D., Starobinsky A. A., 2000, Physical Review Letters, 85, 2236

Bose S., Hellwing W. A., Li B., 2015, J. Cosmology Astropart. Phys., 2, 034

Bower R. G., Benson A. J., Malbon R., Helly J. C., Frenk C. S., Baugh C. M., Cole S., Lacey C. G., 2006, MNRAS, 370, 645

Brans C., Dicke R. H., 1961, Phys. Rev., 124, 925

Brax P., Davis A.-C., Li B., Winther H. A., 2012a, Phys. Rev. D, 86, 044015

Brax P., Davis A.-C., Li B., Winther H. A., Zhao G.-B., 2012b, J. Cosmology Astropart. Phys., 10, 002

Brax P., Davis A.-C., Li B., Winther H. A., Zhao G.-B., 2013, J. Cosmology Astropart. Phys., 4, 029

Brax P., Valageas P., 2014a, Phys. Rev. D, 90, 023508

Brax P., Valageas P., 2014b, Phys. Rev. D, 90, 023507

Brax P., van de Bruck C., Davis A.-C., Mota D. F., Shaw D. J., 2007a, Phys. Rev., D76, 124034

Brax P., van de Bruck C., Davis A.-C., Mota D. F., Shaw D. J., 2007b, Phys. Rev., D76, 085010

Brax P., van de Bruck C., Davis A.-C., Shaw D., 2010, Phys. Rev. D, 82, 063519

Bullock J. S., Kolatt T. S., Sigad Y., Somerville R. S., Kravtsov A. V., et al., 2001, Mon. Not. Roy. Astron. Soc., 321, 559

Cai Y.-C., Li B., Cole S., Frenk C. S., Neyrinck M., 2014, Mon. Not. Roy. Astron. Soc., 439, 2978

Cai Y.-C., Padilla N., Li B., 2015, MNRAS, 451, 1036

Caldwell R. R., Dave R., Steinhardt P. J., 1998, Physical Review Letters, 80, 1582

Carroll S. M., 2001, Living Reviews in Relativity, 4, 1

Carroll S. M., de Felice A., Duvvuri V., Easson D. A., Trodden M., Turner M. S., 2005, Phys. Rev. D, 71, 063513

Carroll S. M., Duvvuri V., Trodden M., Turner M. S., 2004, Phys. Rev. D, 70, 043528

Cataneo M. et al., 2015, Phys. Rev. D, 92, 044009

Chevallier M., Polarski D., 2001, International Journal of Modern Physics D, 10, 213

Clifton T., Ferreira P. G., Padilla A., Skordis C., 2012, Phys. Rep., 513, 1

Colbert J. W. et al., 2013, ApJ, 779, 34

Cole S., 1991, ApJ, 367, 45

Cole S., Lacey C. G., Baugh C. M., Frenk C. S., 2000, MNRAS, 319, 168

Cole S. et al., 2005, MNRAS, 362, 505

Colombi S., Jaffe A., Novikov D., Pichon C., 2009, MNRAS, 393, 511

Cooley J. W., Tukey J. W., 1965, Mathematics of Computation, 19, 297

Copeland E. J., Sami M., Tsujikawa S., 2006, International Journal of Modern Physics D, 15, 1753

Corasaniti P. S., Copeland E. J., 2003, Phys. Rev. D, 67, 063521

Corbett Moran C., Teyssier R., Li B., 2015, Mon. Not. Roy. Astron. Soc., 448, 307

Croton D. J. et al., 2004, MNRAS, 352, 1232

Damour T., Polyakov A. M., 1994, Nuclear Physics B, 423, 532

Davis A.-C., Lim E. A., Sakstein J., Shaw D. J., 2012, Phys. Rev. D, 85, 123006

Davis M., Efstathiou G., Frenk C. S., White S. D. M., 1985, ApJ, 292, 371

De Felice A., Tsujikawa S., 2010, Living Reviews in Relativity, 13, 3

Deffayet C., Esposito-Farèse G., Vikman A., 2009, Phys. Rev. D, 79, 084003

Dicke R. H., 1962, Phys. Rev., 125, 2163

Dodelson S., Efstathiou G., 2004, Physics Today, 57, 60

Dooley G. A., Griffen B. F., Zukin P., Ji A. P., Vogelsberger M., et al., 2014, Astrophys. J., 786, 50

Doran M., Robbers G., 2006, J. Cosmology Astropart. Phys., 6, 26

Duffy A. R., Schaye J., Kay S. T., Dalla Vecchia C., 2008, Mon. Not. Roy. Astron. Soc., 390, L64

Dvali G., Gabadadze G., Porrati M., 2000, Physics Letters B, 485, 208

Efstathiou G. et al., 2002, MNRAS, 330, L29

Einasto J., 1965, Trudy Inst. Astrofiz. Alma-Ata, 51, 87

Eisenstein D. J. et al., 2005, ApJ, 633, 560

Eke V. R. et al., 2004, MNRAS, 348, 866

Ferreira P. G., Joyce M., 1998, Phys. Rev. D, 58, 023503

Fontanot F., Springel V., Angulo R. E., Henriques B., 2012, MNRAS, 426, 2335

Francis M. J., Lewis G. F., Linder E. V., 2009, MNRAS, 394, 605

Gallego J., Zamorano J., Aragon-Salamanca A., Rego M., 1995, ApJ, 455, L1

Gao L., Frenk C. S., Jenkins A., Springel V., White S. D. M., 2012, Mon. Not. Roy. Astron. Soc., 419, 1721

Gao L., Navarro J. F., Cole S., Frenk C., White S. D., et al., 2008, Mon. Not. Roy. Astron. Soc., 387, 536

Gao L., White S. D., Jenkins A., Stoehr F., Springel V., 2004, Mon. Not. Roy. Astron. Soc., 355, 819

Geach J. E. et al., 2010, MNRAS, 402, 1330

Giocoli C., Tormen G., Sheth R. K., van den Bosch F. C., 2010, Mon. Not. Roy. Astron. Soc., 404, 502

Gonzalez-Perez V., Lacey C. G., Baugh C. M., Frenk C. S., Wilkins S. M., 2013, MNRAS, 429, 1609

Gonzalez-Perez V., Lacey C. G., Baugh C. M., Lagos C. D. P., Helly J., Campbell D. J. R., Mitchell P. D., 2014, MNRAS, 439, 264

Gronke M., Llinares C., Mota D. F., Winther H. A., 2015, MNRAS, 449, 2837

Grossi M., Springel V., 2009, MNRAS, 394, 1559

Guo Q., White S., Angulo R. E., Henriques B., Lemson G., Boylan-Kolchin M., Thomas P., Short C., 2013, MNRAS, 428, 1351

Haas M. R., Schaye J., Jeeson-Daniel A., 2012, MNRAS, 419, 2133

Halliwell J. J., 1987, Physics Letters B, 185, 341

Han J., Frenk C. S., Eke V. R., Gao L., White S. D. M., Boyarsky A., Malyshev D., Ruchayskiy O., 2012a, Mon. Not. Roy. Astron. Soc., 427, 1651

Han J., Jing Y. P., Wang H., Wang W., 2012b, Mon. Not. Roy. Astron. Soc., 427, 2437

He J.-h., Hawken A. J., Li B., Guzzo L., 2015, Physical Review Letters, 115, 071306

He J.-h., Li B., Hawken A. J., Granett B. R., 2014, Phys. Rev., D90, 103505

He J.-h., Wang B., 2013, Phys. Rev., D87, 023508

Hellwing W. A., Cautun M., Knebe A., Juszkiewicz R., Knollmann S., 2013a, J. Cosmo. Astropart. Phys., 10, 012

Hellwing W. A., Knollmann S. R., Knebe A., 2010, Mon. Not. Roy. Astron. Soc., 408, 104

Hellwing W. A., Li B., Frenk C. S., Cole S., 2013b, Mon. Not. Roy. Astron. Soc., 435, 2806

Heymans C. et al., 2012, MNRAS, 427, 146

Hinshaw G. et al., 2013, Astrophys. J. Suppl., 208, 19

Hinterbichler K., Khoury J., 2010, Physical Review Letters, 104, 231301

Hockney R. W., Eastwood J. W., 1988, Computer simulation using particles

Hu W., Sawicki I., 2007, Phys. Rev. D, 76, 064004

Hubble E., 1929, Proceedings of the National Academy of Science, 15, 168

Jain B., Vikram V., Sakstein J., 2013, Phys. Rev., D79, 339

Jenkins A., Frenk C. S., White S. D. M., Colberg J. M., Cole S., Evrard A. E., Couchman H. M. P., Yoshida N., 2001, MNRAS, 321, 372

Jennings E., Baugh C. M., Angulo R. E., Pascoli S., 2010, MNRAS, 401, 2181

Jennings E., Baugh C. M., Li B., Zhao G. B., Koyama K., 2012, Monthly Notices of the Royal Astronomical Society, 425, 2128

Jennings E., Baugh C. M., Pascoli S., 2011, MNRAS, 410, 2081

Jing Y., Suto Y., 2002, Astrophys. J., 574, 538

Jose C., Samui S., Subramanian K., Srianand R., 2011, Phys. Rev. D, 83, 123518

Joyce A., Jain B., Khoury J., Trodden M., 2015, Phys. Rep., 568, 1

Joyce A., Lombriser L., Schmidt F., 2016, Annual Review of Nuclear and Particle Science, 66, 95

Khoury J., Weltman A., 2004, Phys. Rev. D, 69, 044026

Kitaura F.-S., Jasche J., Metcalf R. B., 2010, MNRAS, 403, 589

Knollmann S., Knebe A., 2009, Astrophys. J. Suppl., 182, 608

Komatsu E. et al., 2009, ApJS, 180, 330

Koyama K., 2016, Reports on Progress in Physics, 79, 046902

Lacey C., Cole S., 1993, Mon. Not. Roy. Astron. Soc., 262, 627

Lacey C. G. et al., 2016, MNRAS, 462, 3854

Lagos C. D. P., Lacey C. G., Baugh C. M., Bower R. G., Benson A. J., 2011, MNRAS, 416, 1566

Laureijs R. et al., 2011, (arXiv:1110.3193)

Lee J., Zhao G.-B., Li B., Koyama K., 2013, Astrophys. J., 763, 28

Levi M. et al., 2013, (arXiv:1308.0847)

Lewis A., Bridle S., 2002, Phys. Rev. D, 66, 103511

Li B., Efstathiou G., 2012, Mon. Not. Roy. Astron. Soc., 421, 1431

Li B., Hellwing W. A., Koyama K., Zhao G., Jennings E., Baugh C. M., 2013, Mon. Not. Roy. Astron. Soc., 428, 743

Li B., Lam T. Y., 2012, Mon. Not. Roy. Astron. Soc., 425, 730

Li B., Mota D. F., Barrow J. D., 2011, Astrophys. J., 728, 109

Li B., Zhao G., Teyssier R., Koyama K., 2012, J. Cosmo. Astropart. Phys., 01, 051

Li B., Zhao G.-B., Koyama K., 2012, MNRAS, 421, 3481

Li B., Zhao H., 2010, Phys. Rev., D81, 104047

Linder E. V., 1998, New Scientist, 2127, 45

Linder E. V., 2003, Physical Review Letters, 90, 091301

Linder E. V., 2005, Phys. Rev. D, 72, 043529

Liu X. et al., 2016, Physical Review Letters, 117, 051101

Lombriser L., 2014, Constraining chameleon models with cosmology

Lombriser L., Koyama K., Li B., 2014, J. Cosmo. Astropart. Phys., 1403, 021

Lombriser L., Koyama K., Zhao G.-B., Li B., 2012, Phys. Rev. D, 85, 124054

Lombriser L., Li B., Koyama K., Zhao G.-B., 2013, Phys. Rev., D87, 123511

Lombriser L., Simpson F., Mead A., 2015, Physical Review Letters, 114, 251101

LSST Dark Energy Science Collaboration, 2012, (arXiv:1211.0310)

Ludlow A. D., Navarro J. F., Angulo R. E., Boylan-Kolchin M., Springel V., et al., 2014, Mon. Not. Roy. Astron. Soc., 441, 378

Maccio' A. V., Dutton A. A., Bosch F. C. d., 2008, Mon. Not. Roy. Astron. Soc., 391, 1940

Merloni A. et al., 2012, (arXiv:1209.3114)

Mota D. F., Shaw D. J., 2007, Phys. Rev. D, 75, 063501

Muldrew S. I., Pearce F. R., Power C., 2011, Mon. Not. Roy. Astron. Soc., 410, 2617

Navarro J. F., Frenk C. S., White S. D. M., 1996, ApJ, 462, 563

Navarro J. F., Frenk C. S., White S. D. M., 1997, ApJ, 490, 493

Navarro J. F., Hayashi E., Power C., Jenkins A., Frenk C. S., et al., 2004, Mon. Not. Roy. Astron. Soc., 349, 1039

Neto A. F., Gao L., Bett P., Cole S., Navarro J. F., et al., 2007, Mon. Not. Roy. Astron. Soc., 381, 1450

Ng K. C. Y., Laha R., Campbell S., Horiuchi S., Dasgupta B., Murase K., Beacom J. F., 2014, Phys. Rev. D, 89, 083001

Nicolis A., Rattazzi R., Trincherini E., 2009, Phys. Rev. D, 79, 064036

Norberg P., Baugh C. M., Gaztañaga E., Croton D. J., 2009, MNRAS, 396, 19

Nusser A., Gubser S. S., Peebles P., 2005, Phys. Rev., D71, 083505

Olive K. A., Pospelov M., 2008, Phys. Rev. D, 77, 043524

Onions J. et al., 2012, Mon. Not. Roy. Astron. Soc., 423, 1200

Padilla N. D. et al., 2004, MNRAS, 352, 211

Peacock J. A., Heavens A. F., 1990, MNRAS, 243, 133

Peebles P. J. E., 1976, ApJ, 205, 318

Percival W. J. et al., 2010, MNRAS, 401, 2148

Perlmutter S. et al., 1999, ApJ, 517, 565

Pietroni M., 2005, Phys. Rev. D, 72, 043535

Planck Collaboration et al., 2014, A&A, 571, A16

Planck Collaboration et al., 2016a, A&A, 594, A13

Planck Collaboration et al., 2016b, A&A, 594, A24

Planck Collaboration et al., 2016c, A&A, 594, A14

Platen E., van de Weygaert R., Jones B. J. T., Vegter G., Calvo M. A. A., 2011, MNRAS, 416, 2494

Poole G. B. et al., 2013, MNRAS, 429, 1902

Power C., Navarro J., Jenkins A., Frenk C., White S. D., et al., 2003, Mon. Not. Roy. Astron. Soc., 338, 14

Pozzetti L. et al., 2016, A&A, 590, A3

Prada F., Klypin A. A., Cuesta A., Betancort-Rijo J. E., Primack J., 2012, Mon. Not. Roy. Astron. Soc., 423, 3018

Prunet S., Pichon C., Aubert D., Pogosyan D., Teyssier R., Gottloeber S., 2008, Astrophys. J. Suppl., 178, 179

Ratra B., Peebles P. J. E., 1988, Phys. Rev. D, 37, 3406

Reed D., Bower R., Frenk C., Jenkins A., Theuns T., 2007, Mon. Not. Roy. Astron. Soc., 374, 2

Riess A. G. et al., 1998, AJ, 116, 1009

Sánchez A. G., Baugh C. M., Angulo R. E., 2008, MNRAS, 390, 1470

Sánchez A. G., Crocce M., Cabré A., Baugh C. M., Gaztañaga E., 2009, MNRAS, 400, 1643

Sánchez A. G. et al., 2012, MNRAS, 425, 415

Sanchez-Conde M. A., Prada F., 2014, Mon.Not.Roy.Astron.Soc., 442, 2271

Sawala T., Frenk C. S., Crain R. A., Jenkins A., Schaye J., Theuns T., Zavala J., 2013, Mon. Not. Roy. Astron. Soc., 431, 1366

Schaller M. et al., 2015, MNRAS, 451, 1247

Schaye J. et al., 2015, MNRAS, 446, 521

Schechter P., 1976, ApJ, 203, 297

Schmidt F., 2010, Phys. Rev., D81, 103002

Shao J., 1986, The Annals of Statistics, 14, 1322

Sheth R. K., Tormen G., 1999, MNRAS, 308, 119

Shi D., Li B., Han J., Gao L., Hellwing W. A., 2015, MNRAS, 452, 3179

Shim H., Colbert J., Teplitz H., Henry A., Malkan M., McCarthy P., Yan L., 2009, ApJ, 696, 785

Sobral D., Smail I., Best P. N., Geach J. E., Matsuda Y., Stott J. P., Cirasuolo M., Kurk J., 2013, MNRAS, 428, 1128

Somerville R. S., Davé R., 2015, ARA&A, 53, 51

Sotiriou T. P., Faraoni V., 2010, Reviews of Modern Physics, 82, 451

Spergel D. et al., 2013, (arXiv:1305.5422)

Springel V., 2005, MNRAS, 364, 1105

Springel V. et al., 2005, Nature, 435, 629

Srisawat C. et al., 2013, Mon. Not. Roy. Astron. Soc., 436, 150

Stasińska G., 1990, A&AS, 83, 501

Steinhardt P. J., Wang L., Zlatev I., 1999, Phys. Rev. D, 59, 123504

Taruya A., Nishimichi T., Bernardeau F., Hiramatsu T., Koyama K., 2014, Phys. Rev., D90, 123515

Tasitsiomi A., Kravtsov A. V., Wechsler R. H., Primack J. R., 2004, ApJ, 614, 533

Taylor J. H., Weisberg J. M., 1982, ApJ, 253, 908

Teyssier R., 2002, Astron. Astrophys., 385, 337

Vainshtein A., 1972, Physics Letters B, 39, 393

van den Bosch F. C., Tormen G., Giocoli C., 2005, Mon. Not. Roy. Astron. Soc., 359, 1029

Vikram V., Sakstein J., Davis C., Neil A., 2014, (arXiv:1407.6044)

Vogelsberger M. et al., 2014, MNRAS, 444, 1518

Wang J., Frenk C. S., Navarro J. F., Gao L., Sawala T., 2012, Mon. Not. Roy. Astron. Soc., 424, 2715

Wang Y., Mukherjee P., 2006, ApJ, 650, 1

Wang Y., Wang S., 2013, Phys. Rev. D, 88, 043522

Wechsler R. H., Bullock J. S., Primack J. R., Kravtsov A. V., Dekel A., 2002, Astrophys. J., 568, 52

Weinberg D. H., Mortonson M. J., Eisenstein D. J., Hirata C., Riess A. G., Rozo E., 2013, Phys. Rep., 530, 87

Wetterich C., 1988, Nuclear Physics B, 302, 645

Wetterich C., 1995, A&A, 301, 321

Wetterich C., 2004, Physics Letters B, 594, 17

White M., 2001, Astron. Astrophys., 367, 27

White S. D. M., Frenk C. S., 1991, ApJ, 379, 52

Will C. M., 2014, Living Reviews in Relativity, 17, 4

Winther H. A., Mota D. F., Li B., 2012, ApJ, 756, 166

Yan L., McCarthy P. J., Freudling W., Teplitz H. I., Malumuth E. M., Weymann R. J., Malkan M. A., 1999, ApJ, 519, L47

Yaryura C. Y., Baugh C. M., Angulo R. E., 2011, MNRAS, 413, 1311

Zhao D. H., Jing Y. P., Mo H. J., Borner G., 2003, Astrophys. J., 597, L9

Zhao G., 2014, Astrophys. J. Suppl., 211, 23

Zhao G.-B., Li B., Koyama K., 2011a, Phys. Rev. D, 83, 044007

Zhao G.-B., Li B., Koyama K., 2011b, Physical Review Letters, 107, 071303

Zivick P., Sutter P. M., Wandelt B. D., Li B., Lam T. Y., 2015, MNRAS, 451, 4215

# Appendix A

# Consistency check of the $\Phi_\star$ environment measure

While defining the experienced gravity environment measure, $\Phi_\star$, we have subtracted the self Newtonian potential due to a halo itself from the total potential inside the halo, so that $\Phi_\star$ is created by all matter outside the halo, including the large-scale structure. Since the size of the halo is generally negligible compared with the effective size of surrounding environment, we would expect $\Phi_\star$ to vary little inside it. As a result, an important consistency check is to check that the $\Phi_\star$ numerically obtained from the simulation does indeed have very little fluctuation inside haloes, for example, across the different bins of radial distance.

For this check, we divide the halo radius, $r_{200}$, into 20 bins equally spaced in logarithmic scale and calculate the values of $\Phi_\star(r)$ in each spherical shell according to Eq. (4.3.8). The value of $\Phi_\star$ for a halo quoted in Chapter 4 is the average of these 20 values. The left panel of Fig. A.1 shows the distribution of this average value for all haloes in the lowest halo mass bin (just for example). We see that the environment potential of haloes $\Phi_\star$ peaks at around $|\Phi_\star| = 10^{-5.5}$, and is between $10^{-7} \sim 10^{-5}$ for most haloes. There is very little redshift evolution of this distribution.

We also calculate the standard deviation of the $\log |\Phi_\star|$ values in all bins for each halo. The right panel displays the distribution of standard deviation of $\log_{10} |\Phi_\star|$ for the same haloes as considered in the left panel. Although the values of $\log_{10} |\Phi_\star|$ mostly fall between $-7$ and $-5$, the variation in the different radius bins is fairly
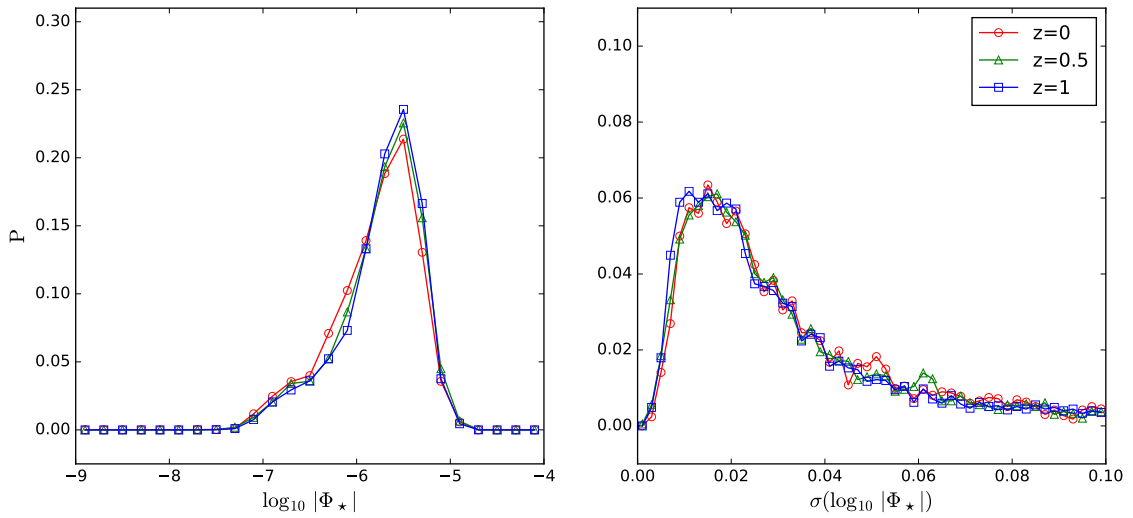
Figure A.1: The probability distribution of the average value of $\Phi_\star$ inside dark matter haloes (left panel) and the standard deviation of $\log_{10}|\Phi_\star|$ across 20 different radius bins (right panel). The mass range of the haloes is $1 \sim 3 \times 10^{11} \mathrm{M}_\odot/h$. The variation of $\Phi_\star$ is very small inside haloes, confirming that $\Phi_\star$ is mainly determined by the larger-scale structures, and therefore is a good environment measure.

small, peaking at $\sim 0.02$ and smaller than 0.1 for most haloes. This indeed confirms that $\Phi_\star$ is almost a constant within dark matter haloes, and not affected by the fairly strong dependence of the total gravitational potential $\Phi(r)$ on the radial distance $r$.

# Appendix B

# Redshift Distortion in Modified Gravity

Peculiar velocity distorts the measurement of the mass distribution on Mpc scales in galaxy surveys. The redshift-space distortion (RSD) is a fundamental cosmological observable to constrain the cosmological parameters and allow us to look for deviations from standard ΛCDM model. The halo bias is one of the key parameters in modeling RSD effects or interpreting observational results. We study the halo bias and redshift distortion effects in two modified gravity theories from N-body simulations. We measure the halo bias by matter power spectra and two-point correlation functions and examining the redshift distortion effects in 2D matter power spectra. This appendix shows some preliminary results of this work.

## B.1  Modified Gravity Models

We study two modified gravity in this work. One is the $f(R)$ gravity model proposed by Hu & Sawicki (2007), and focus on the "F5" model with parameter $n = 1, |f_{R0}| = 10^{-5}$ and "F6" model with $n = 1, |f_{R0}| = 10^{-6}$. The F6 models is the same model as LIMINALITY simulation in Chapter 3 and 4. The brief review of the general theory of $f(R)$ gravity and this $f(R)$ model we study can be seen in §3.2.1.

The other model we study is "nDGP" model, which refers to the normal branch solution of DGP gravity (Dvali et al., 2000). The DGP model is an example of a

braneworld model. Matter in DGP gravity is confined to live in a four-dimensional brane, embedded in a five-dimensional bulk spacetime. DGP model obeys In the simulations of this work, we consider two parameter values, $rcH_0 = 1$ and $rcH_0 = 5$ as "nDGP5" and "nDGP6" models. These were chosen to roughly match the F5 and F6 models, respectively, in terms of the values of $\sigma_8$ at $z = 0$.

## B.2  Simulations

We run a set of N-body simulations in GR, $f(R)$ and DGP cosmologies, using ECOS-MOG code with $1024^3$ particles in a comoving cubic box of side length 1024 $h^{-1}$Mpc (Li et al., 2012). The particle mass is $7.80 \times 10^{10}$ $h^{-1} M_\odot$. ROCKSTAR is used to identify the dark matter halos and measure their properties (Behroozi et al., 2013). We measure power spectra using the code POWMES (Colombi et al., 2009) and 2-point correlation function using the code CUTE (Alonso, 2012).

## B.3  Results

We bin the halo catalog into 6 mass ranges, $1 \sim 5 \times 10^{12}, 5 \times 10^{12} \sim 1 \times 10^{13}, 1 \sim 5 \times 10^{13}, 5 \times 10^{13} \sim 1 \times 10^{14}, 1 \sim 5 \times 10^{14} \mathrm{M_\odot}/h$ as bin0, bin1, bin2, bin3 and bin4 respectively.

### B.3.1  Matter power spectrum

In Fig. B.1, we plot the real space dark matter power spectra at $z = 0$ (upper panel) and their relative difference (lower panel) measured from GR and the modified gravity model simulations. Due to the enhanced gravity, $fR$ and DGP models have much higher $P(k)$ magnitude than GR at small scales ($k > 0.1$ $h$/Mpc). Although the simulations start from the same initial condition, the modified gravity models also have slightly higher $P(k)$ signal than GR at large scales. The difference between nDGP5 and GR is about 30% at $k < 0.1$ $h$/Mpc.
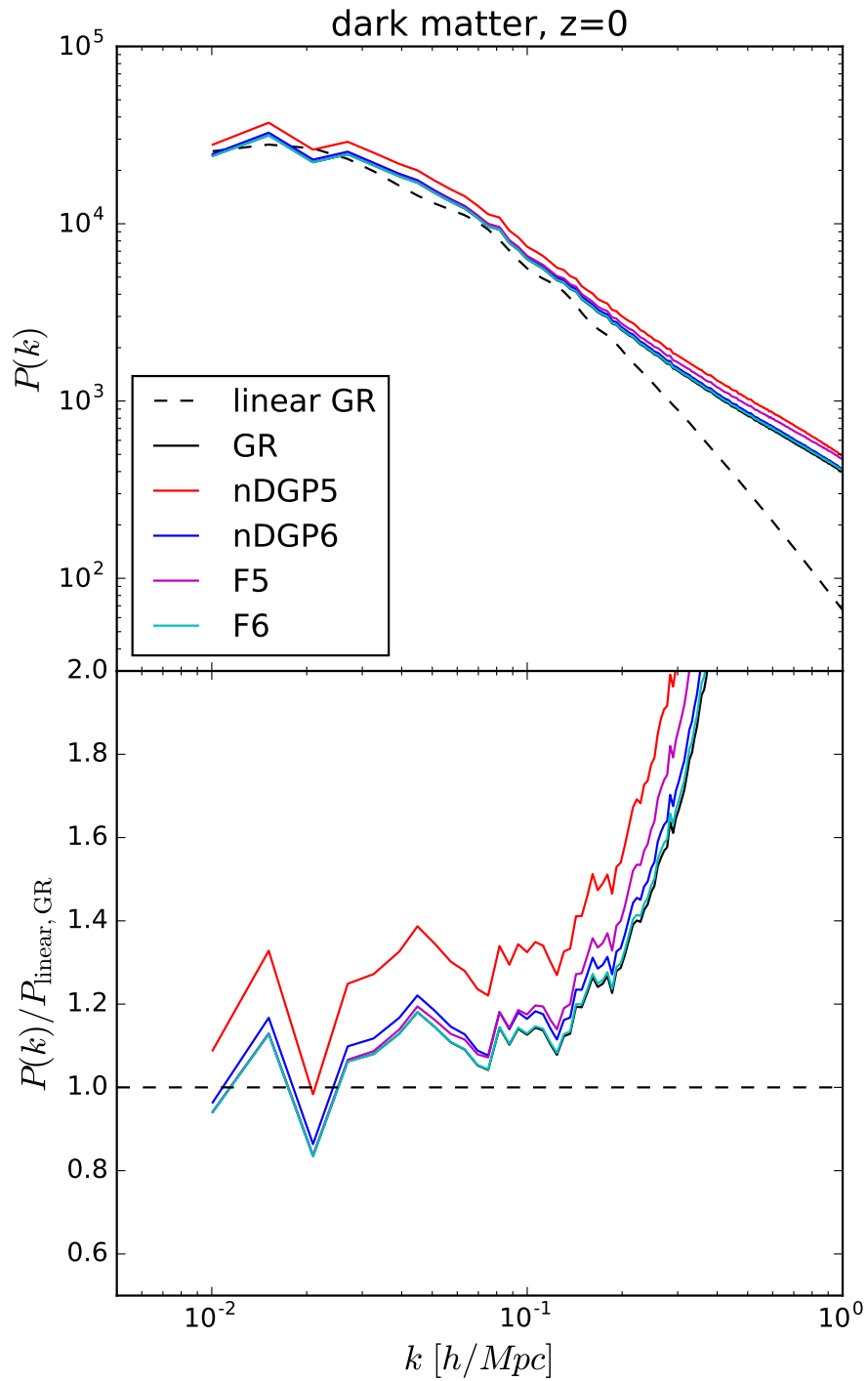
Figure B.1: Upper panel: the real space dark matter power spectrum in GR and 4 modified gravity models (solid lines), comparing to the GR linear theory (black dashed line). Lower panel: The ratio of the power spectrum measured from simulation to the GR linear theory.

## B.3.2 Halo mass function

Fig. B.2 shows the differential halo mass functions of GR and modified gravity models (upper panel) and their relative differences (lower panel) at $z = 0, 0.7$ and 1 from the simulations. Due to the mass resolution and the AMR N-body simulation, only halo massive than $10^{13} M_\odot/h$ can be trusted. F6 model has very similar halo mass function with GR because its very weak enhancement of gravity in low-density place at low redshift. Whilst F5, nDGP5 and nDGP6 models have rather more haloes than GR from $z = 1$ to 0. The difference is increasing with cosmic time. At $z = 0$, F5, nDGP5 and nDGP6 model has up to 20% more haloes within mass range $10^{13} - 10^{14} M_\odot/h$ than GR.

## B.3.3 Linear halo bias

The dark matter halo only lives in high-density region of the Universe. The statistics measured from this peak distribution is biased. In order to correctly estimate the true matter density, a halo bias arising from this incomplete selection has to be introduced. At large scales, the bias is nearly a constant. To measure the linear halo bias, we need to decided the "linear regime" first, which is depending on both redshift and sample incompleteness. Fig. B.3 shows how the range of $k$ ($k_{min} < k < k_{max}$) affects the linear halo bias measured by auto power spectrum in GR at $z = 0$. We fix the lower bound $k_{min} = 0.01 h/Mpc$. The upper bound $k_{max}$ is plotted as the x axis. It is clear that the shot noise affects linear bias measurement at all scales. But after subtracting the shot noise, the bias curve keeps almost flat up to $k_{max} = 0.1 h/Mpc$ for all the five halo bins. Here, we conclude that $k < 0.01 h/Mpc$ can be treated as linear scale in auto power spectrum measurements.

**Halo bias measurements comparison**

Beside the power spectrum, the two-point correlation function can be used to measure halo bias, as well. Fig. B.4 shows the comparison of linear halo bias measured from power spectrum and two-point correlation function. We use the linear range, $0.01 < k < 0.10 h/$Mpc for auto power spectrum, $0.01 < k < 0.04 h/$Mpc
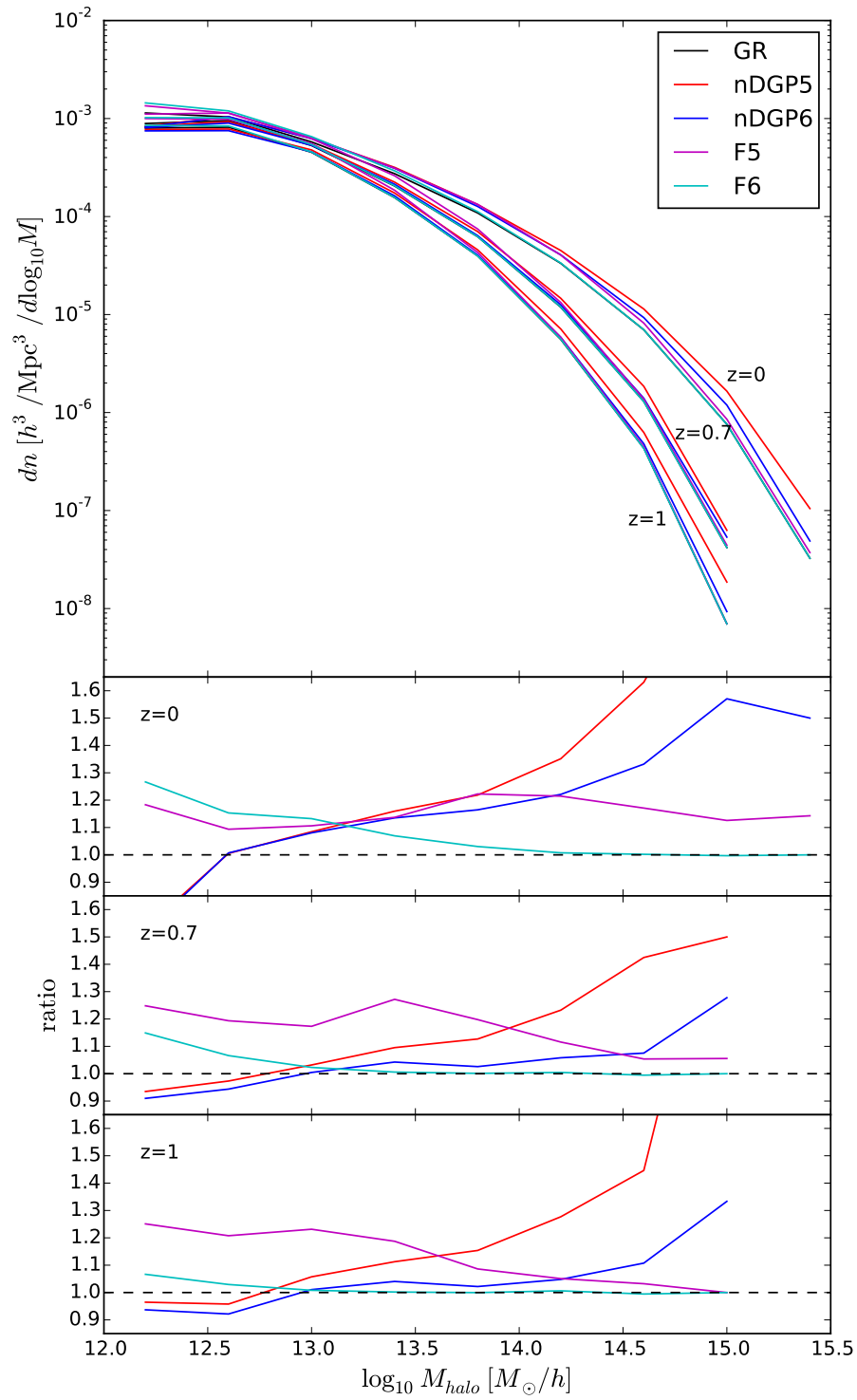
Figure B.2: Upper panel: the differential halo mass function in GR and 4 modified gravity models at $z = 0, 0.7$ and 1. Lower panels: The ratio of halo mass function between modified gravity models and GR.
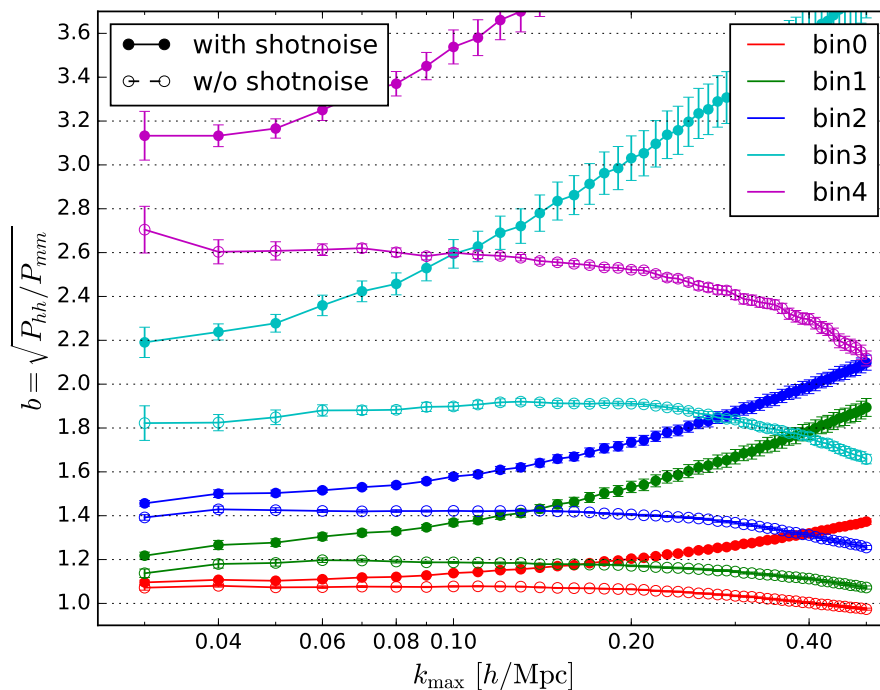
Figure B.3: The linear halo bias measured from auto power spectrum in GR against the upper bound of linear regime, $k_{max}$. The lower bound is fixed as $k_{min} = 0.01 h/Mpc$.

for cross power spectrum and $5 < r < 40\mathrm{Mpc}/h$ for correlation function. All the four measurements have very similar results at low mass halos. The auto power spectrum, auto and cross two-point correlation functions have extremely agreement up to $10^{14} M_\odot/h$ halo mass. All measurements in Fig. B.4 have subtracted the shot noise. Hereinafter, we will only use the halo bias measured from auto power spectra.

**Halo bias in different cosmologies**

Fig. B.5 shows the comparison of auto power spectrum bias among GR, nDGP and $f(R)$. F6 model has very similar halo bias as GR, while F5 model has a slightly smaller bias at $z = 0$. nDGP5 and nDGP5 have fairly smaller halo bias than GR for $10^{12} \sim 5 \times 10^{14} M_\odot/h$ halos at all three redshifts. This is mainly because the same halo bin in different model has different halo abundance (see halo mass function in Fig. B.2). Therefore, the linear halo bias in GR cannot be used in modified gravity cosmologies.
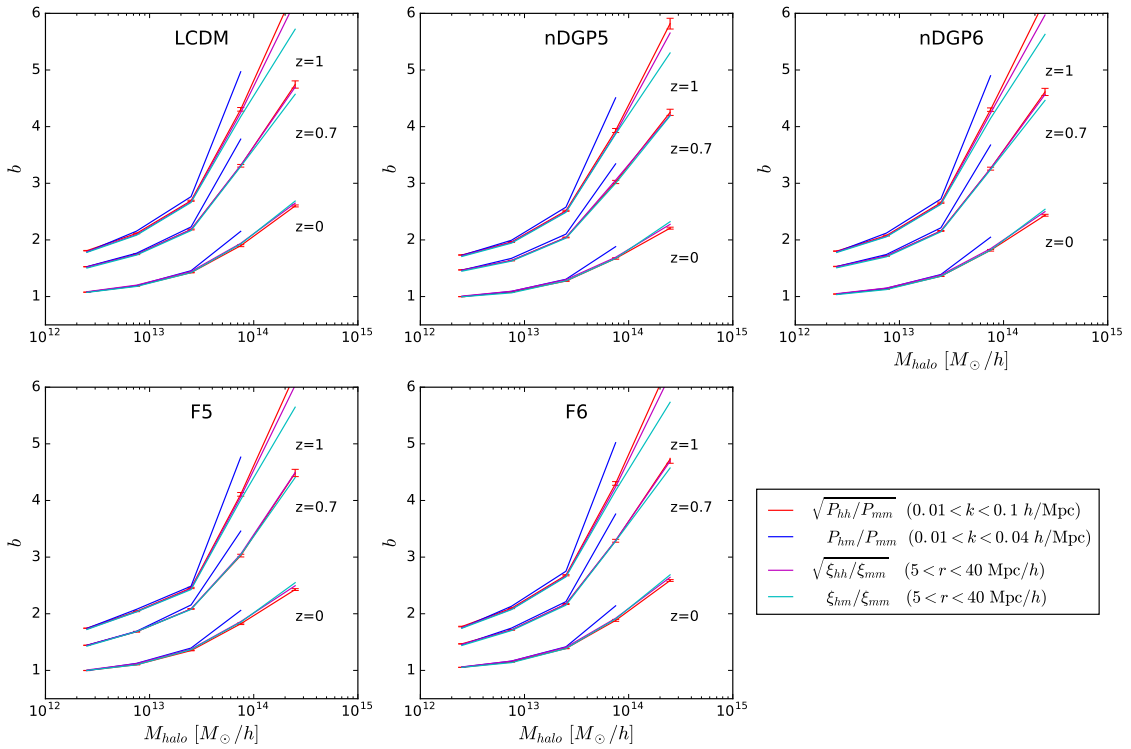
Figure B.4: The halo bias against halo mass at $z = 0, 0.7$ and 1. The halo bias is measured from simulations in different ways: auto power spectrum in range $0.01 < k < 0.10h/\mathrm{Mpc}$, cross power spectrum in range $0.01 < k < 0.04h/\mathrm{Mpc}$, auto and cross 2-point correlation function in range $5 < r < 40\mathrm{Mpc}/h$.
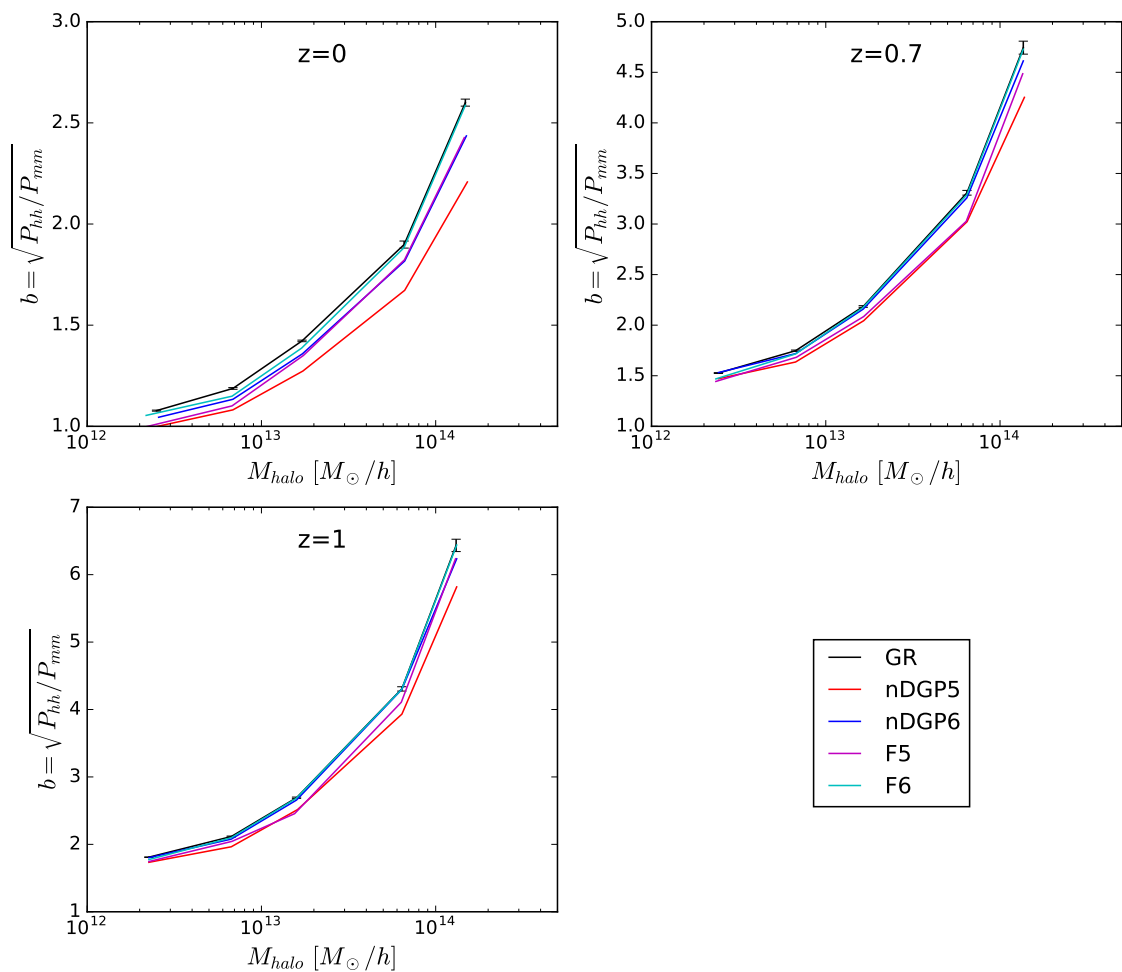
Figure B.5: The halo bias measured from auto power spectrum correlation in range of $0.01 < r < 0.1$ $h$/Mpc against halo mass at $z = 0, 0.7$ and $1$. The halo mass is plotted as median of the bin.

## B.3.4   Redshift-space distortion results

The redshift-space distortion at large scales only affects to the line-of-sight direction. Examining the 2D redshift-space galaxy power spectrum, $P(k, \mu)$, could isolate the impact of RSD effects. Here, $\mu$ is cosine of the angle to the line of sight. We have binned the measured power spectra into five $\mu$ bins that are centred at $\mu = 0.1, 0.3, 0.5, 0.7$ and $0.9$.

Fig. B.6 shows the ratio of the anisotropic 2D power spectra in redshift space, $P^s(k, \mu)$, to 3D power spectra real space, $P^r(k, \mu)$, in the five models. It is clear that the $\mu = 0.1$ bin is almost not affected by RSD, and $\mu = 0.9$ bin have more than $50\%$ enhancement compared to the real space power spectra. The dashed lines

correspond to the linear-theory prediction $(1 + f/b_L \mu^2)^2$ for each $\mu$ bin. On the left panel, each set of $P^s$ and $P^r$ is measured from the same cosmology. The departures at large scales between different models are tiny and negligible if considering the big statistic error at large scales. The linear-theory predictions roughly agree with the simulation results at large scales. The best-fit linear bias is measured as $b_L = \sqrt{P_{halo}/P_{DM}}|_{k<0.05}$ for each model. On the right panel, we compare $P^s$ in all five models to $P^r$ in GR. These departures between different model become fairly larger, especially for the F5 model. In this circumstance, linear-theory predictions for GR (black dashed line) cannot used in modified gravity cosmologies, even for $\mu = 0.1$ bin.

Fig. B.7 shows the ratio of the anisotropic 2D redshift-space power spectrum, $P^s(k, \mu)$, compared to the linear theory Kaiser prediction, $P^s(k, \mu) = (b_L + f\mu^2)^2 P_{\text{linearGR}}$, where $P_{\text{linearGR}}$ is the linear-theory power spectrum in GR at $z = 0$. In this circumstance, we assume the underlying gravity theory is GR. However, the linear theory prediction will not agreed with measured power spectrum measured from a modified gravity cosmology. The nDGP5 model has 30% departure from linear theory prediction. It is mainly because the power spectrum in modified gravity model is different from that in GR (see Fig. B.1).

We replace the halo bias with a 'fake' bias which is defined as $b_L = \sqrt{P_{halo}/P_{DM,GR}}|_{k<0.05}$ in order to compensate the different $P(k)$ in different cosmologies. In Fig. B.8, all the modified gravity model agree with linear theory Kaiser prediction quite well at large scales. It implies that if using a GR based model to intercept a modified gravity cosmology, we must to apply this 'fake' bias to compensate the model differences. In addition, the non-linear difference at $k < 0.2h/\text{Mpc}$ is significant between GR and modified gravity models, especially in high $\mu$ bins. This gives a light to distinguish cosmological models. Further study of RSD non-linear effects is our future work.
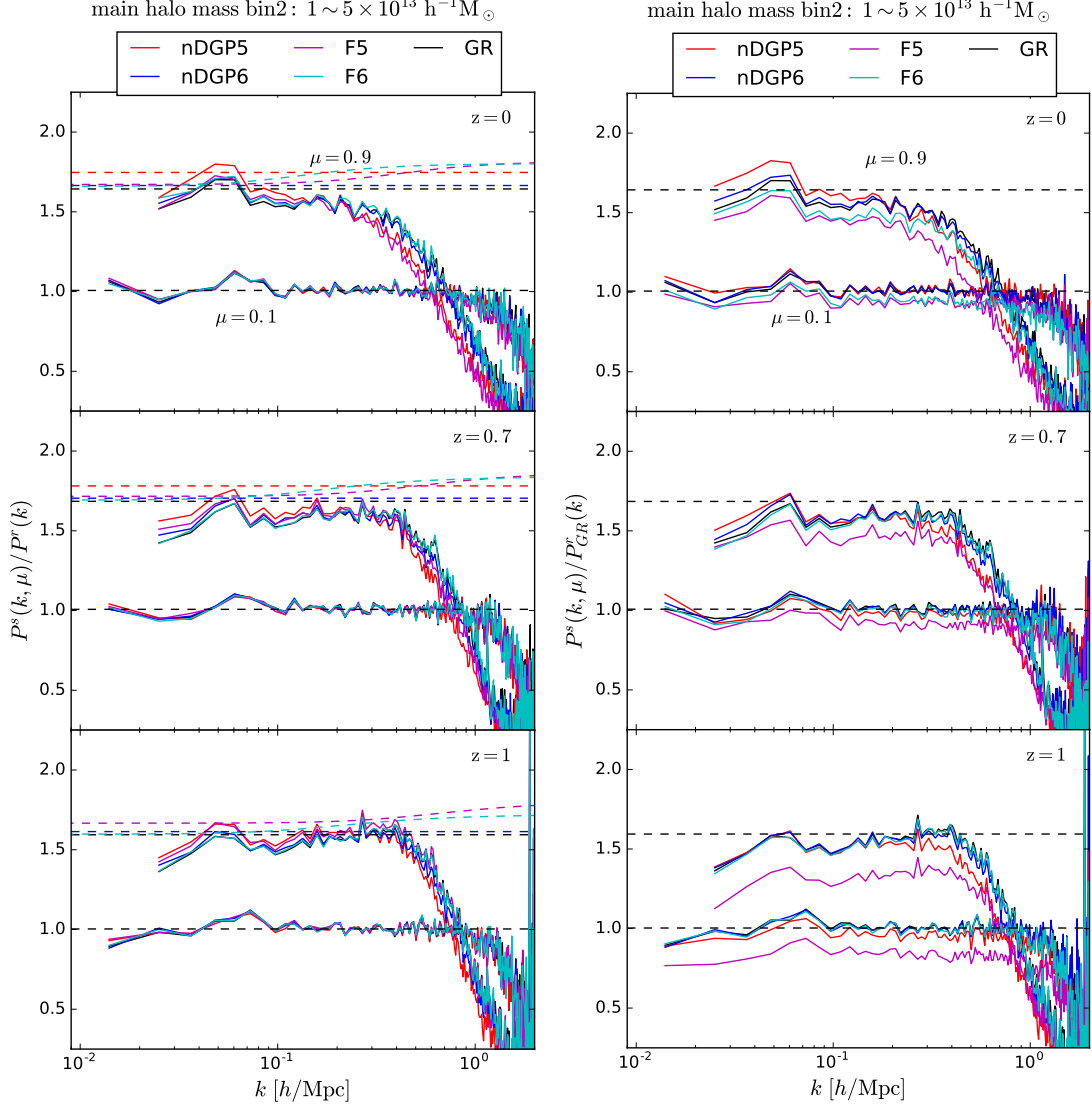
Figure B.6: The ratio of the anisotropic power spectra in redshift space to real space, $P^s(k, \mu)/P^r(k)$, for GR and 4 modified gravity models. The colors of each line represent the $\mu$ bin plotted as given in the legend. The dashed lines are the linear-theory prediction $(1 + f/b_L\mu^2)^2$. The best-fit linear bias is measured as $b_L = \sqrt{P_{halo}/P_{DM}}|_{k<0.05}$ for each model. In the left panel, for each model, both redshift power spectrum and real space power spectrum are measured from simulation. In the right panel, we use GR real space power spectrum as real space $P(k)$ in all models.

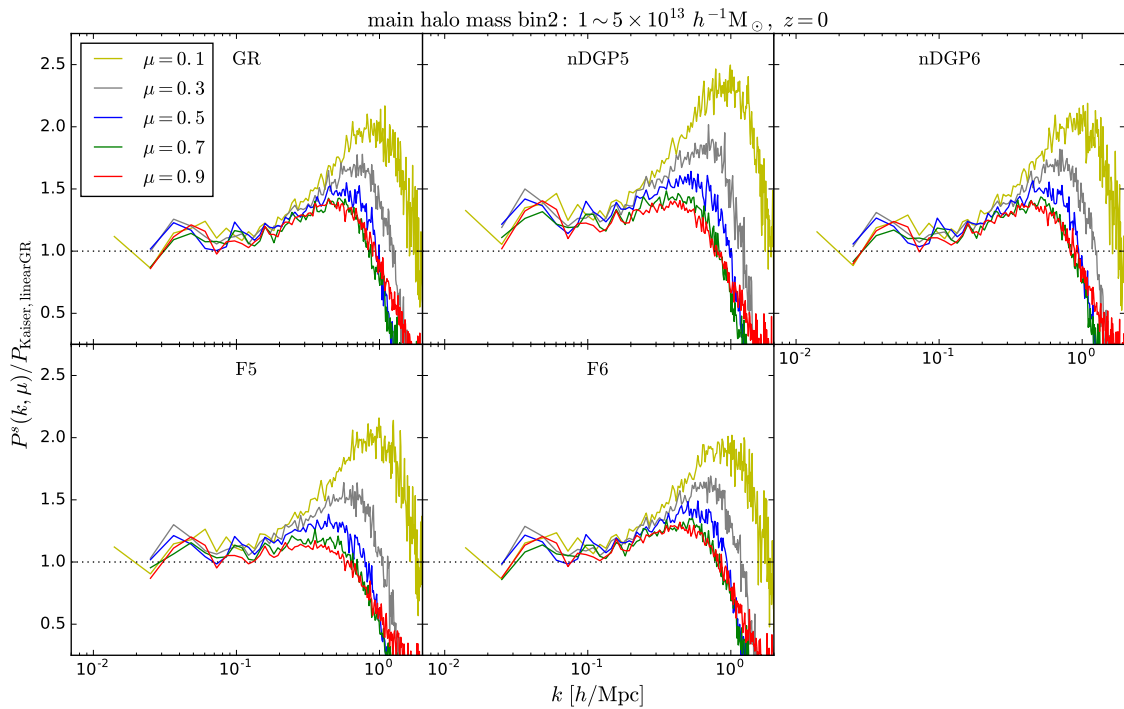main halo mass bin2 : $1 \sim 5 \times 10^{13} \ h^{-1} \mathrm{M}_\odot$ , $z = 0$



Figure B.7: The ratio of the anisotropic redshift space power spectrum $P^s(k, \mu)$, for GR and 4 modified gravity models, compared to the linear theory Kaiser prediction $P^s(k, \mu) = (b_L + f\mu^2)^2 P_{\mathrm{linearGR}}$. Here, $P_{\mathrm{linearGR}}$ is the linear-theory power spectrum in GR, and $b_L = \sqrt{P_{halo}/P_{DM}}|_{k<0.05}$ is the best-fit linear bias for each model. This plot shows the impact of nonlinear growth.

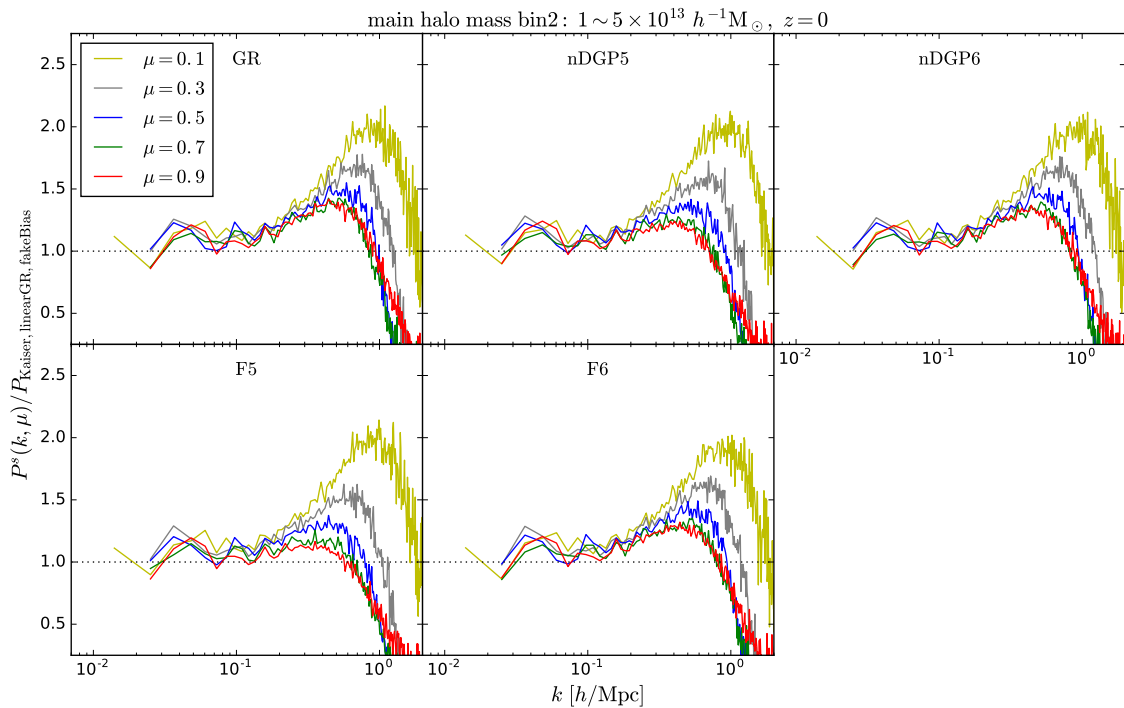main halo mass bin2 : $1 \sim 5 \times 10^{13} \ h^{-1} \mathrm{M}_\odot$ , $z = 0$



Figure B.8: The same ratio as Fig. B.7. But here uses the "fake" bias, $b_L = \sqrt{P_{halo}/P_{DM,GR}}|_{k<0.05}$.